



universität
wien

DIPLOMARBEIT

Titel der Diplomarbeit:

„Investigation of relevant phase diagrams for high
temperature solder materials:
The binary systems Cu-Sn and Cu-Sb“

Verfasser

Siegfried Fürtauer

angestrebter akademischer Grad:

Magister der Naturwissenschaften (Mag. rer. nat.)

Wien, 2010

Studienkennzahl lt. Studienblatt:

A 190 423 482

Studienrichtung lt. Studienblatt:

Lehramtsstudium: UF „Chemie“ und UF „Bewegung und Sport“

Betreuer:

Ao. Univ.-Prof. Mag. Dr. Hans Flandorfer

Acknowledgements

“Most problems arise by their answer.”

Leonardo da Vinci (1452-1519)

“Without speculation it is not possible to make new observations.”

Charles Darwin (1809-1882)

“If the facts don't fit the theory, change the facts.”

Albert Einstein (1897-1955)

I want to express my gratitude to my thesis supervisor Dr. Hans Flandorfer, who accompanied me during the last year in a very patient and supporting way and conveyed a lot of knowledge and the scientific way of thinking and working to me.

Furthermore I want to thank Dr. Christian Lengauer, who accomplished the high temperature X-ray diffraction measurements and spent a lot of effort to improve the quality of the data.

I thank all my colleagues in the department for helping me with the practical work, especially to Mag. Bea Huber, Mag. Norbert Ponweiser, Mag. Martin Marker and Dr. Clemens Schmetterer.

Special thanks go to my parents, who enabled me to finish my academic studies, as well as to my partner Lisa Haberl, who supported me the last years and had a lot of appreciation for my work.

Finally I want to thank the FWF (Fonds zur Förderung der wissenschaftlichen Forschung), who provided the funds for this work by the project P21507-N19.

Table of Content

1	Introduction	- 4 -
2	Soldering	- 5 -
2.1	Solder materials.....	- 6 -
2.1.1	Soft solders	- 6 -
2.1.2	Hard solders.....	- 8 -
2.1.3	Lead free high temperature soft solders.....	- 9 -
3	Literature review	- 11 -
3.1	The elements	- 11 -
3.1.1	Copper (Cu).....	- 11 -
3.1.2	Tin (Sn).....	- 13 -
3.1.3	Antimony (Sb).....	- 15 -
3.2	Cu-Sn	- 17 -
3.2.1	Introduction	- 17 -
3.2.2	High-temperature phases	- 18 -
3.2.3	Phases in Cu-Sn.....	- 29 -
3.3	Cu-Sb	- 30 -
4	Experimental section	- 34 -
4.1	Sample preparation of Cu-Sn	- 34 -
4.2	Sample preparation of Cu-Sb	- 39 -
4.3	Measurement systems	- 41 -
4.3.1	Differential Thermals Analysis Netzsch DTA 404S.....	- 41 -
4.3.2	Differential Thermals Analysis Setaram Setsys Evolution.....	- 42 -
4.3.3	Reflected light microscope Zeiss Axiotech 100	- 44 -
4.3.4	EPMA CAMECA SX 100 and ESEM Zeiss Supra 55 VP	- 45 -
4.3.5	Bruker D8 Powder-X-Ray-Diffractometer	- 47 -
4.3.6	The Rietveld-refinement.....	- 49 -
4.3.7	High temperature Bruker D8	- 50 -
5	Discussion	- 51 -
5.1	Results in the system Cu-Sn.....	- 51 -
5.1.1	Thermal analysis: DTA	- 51 -
5.1.2	PXRD at room temperature	- 55 -
5.1.3	HTPXRD	- 56 -
5.1.4	ESEM / EPMA	- 60 -
5.1.5	Phase diagram Cu-Sn.....	- 64 -
5.2	Results in the system Cu-Sb.....	- 67 -
5.2.1	Thermal analysis: DTA	- 67 -
5.2.2	PXRD at room temperature	- 71 -
5.2.3	ESEM / EPMA	- 78 -
5.2.4	Phase diagram Cu-Sb.....	- 84 -
5.3	Comparison of Cu-Sn and Cu-Sb.....	- 87 -
6	Summary	- 91 -
6.1	Summary (English)	- 91 -
6.2	Zusammenfassung (Deutsch)	- 92 -
7	References	- 93 -
8	Appendices	- 98 -
8.1	List of figures	- 98 -
8.2	List of tables.....	- 99 -
8.3	Curriculum Vitae et Studiorum	- 100 -

1 Introduction

Although solders in the electronic industry have only a relative small contribution to the worldwide consumption of lead, the recycling of the electronic waste is complicated and thus it pollutes the environment. Therefore the electronic industry has tried to substitute the poisonous lead in the solders for less harmful materials during the last decade. In the European Union the use of lead containing solders is prohibited since 2006, except for a few special applications (medical equipment, aerospace industry, monitoring and control systems, network infrastructure and servers in the telecommunication sector). While the development of lead free low temperature soft solders (melting point $\sim 180\text{-}230^\circ\text{C}$) is fairly advanced, the research of lead free high temperature soft solders (melting range $> 230\text{-}350^\circ\text{C}$) has just started. For a systematic search of useful alloy systems some fundamental data regarding the phase relations and thermochemical properties are essential. Within the budget of the COST-Action MP0602 an encyclopaedically data base with these and other continuative data will be created. Interested alloys are those ones which could include the components of the lead free solder and the substrate materials. This work concentrates on the experimental research of the binary systems Cu-Sn and Cu-Sb. Experimental techniques are the powder X-ray diffraction at normal and higher temperatures (PXRD / HTPXRD), thermal analysis (DTA) and metallographic methods (EPMA / ESEM). The available phase diagrams of the literature will be improved and completed. The Cu-Sn system is the key to understand the mechanisms of lead free solders, because tin is the main component of the solders and copper is the most common substrate, as well as a component of the solder itself. Despite the fact that there is already a considerable amount of data available for Cu-Sn, some ambiguities occurred during the research. This primarily affects the high temperature phases, which are known to be not stable at room temperature. Due to the relationship of the elements tin and antimony, also the system Cu-Sb would be worth to be investigated. These alloys are known less than the Cu-Sn bronzes. Because of the similar tendency to form metastable phases, parallels between these two systems could be drawn. There is also an interest in the Cu-Sb system, because antimony itself is a component of some solders, e.g. Ag-Sb-Sn or Cu-Sb-Sn. Aim of this work is to improve existing phase diagram versions and contribute valuable information for the lead free solder data base which would enable better thermodynamic calculations (CALPHAD).

2 Soldering

The solder process is a very important industrial method to join two working pieces, which are in most cases metals. In contrast to other processes of metal connection, in soldering an alloy with a low melting point is used to fill the gap between the metallic pieces, as well as two different kinds of metal can be joined by soldering. The interaction between solder and substrate is dominated by diffusion. In a very thin diffusion zone the solder migrates into the substrate. This zone is often very brittle, much more than the substrate, and its diameter is determined by the solder process parameters, e.g. the exposure time and temperature.

Another major process is adhesive bonding, where a glue material is coated that sticks the metals together. Both processes, adhesive bonding and soldering, form reversible joints which can be released by applying heat.

The third method to connect two metallic parts is welding. Here the metal is heated until it becomes ductile or liquid, and then the edges are pressed together with pressure. The welded joint can show the same mechanical properties as the untreated machine part.

Soldering has, due to a range benefits, a lot of applications, e.g. solder joints in the electronic industry, for the machine building industry, for the connection of installation pipes, for the construction of engine parts, heat exchangers and tools, and for several other devices.

The benefits, as well as the disadvantages of soldering are listed in Table 1 and 2.

Table 1: Benefits of soldering [1]

- | |
|---|
| <ul style="list-style-type: none">• Joining of two or more different metals• Low energy costs (low melting temperature)• Low oxidation of the surface due to low temperatures and exposition times• Also non-metallic components solderable (metal layer technique)• Gas-and vacuumproof connections• Good thermal and electric conductivity• Ductile joints possible• Flexible use• gentle material treatment• Low consumption of material: Small parts, lightweight parts• Safe connection of different shaped parts• Good mechanical stability (hard solder)• Automatable, Soldering of more than 2 parts at the same time |
|---|

Table 2: Disadvantages of soldering [1]

- Low mechanical stability of soft solders
- Corrosion due to different electrochemical potentials
- Surface pre-treatment necessary
- Limited gap width
- Decrease of strength at higher temperatures
- Pore formation due to flux melting agent inclusions

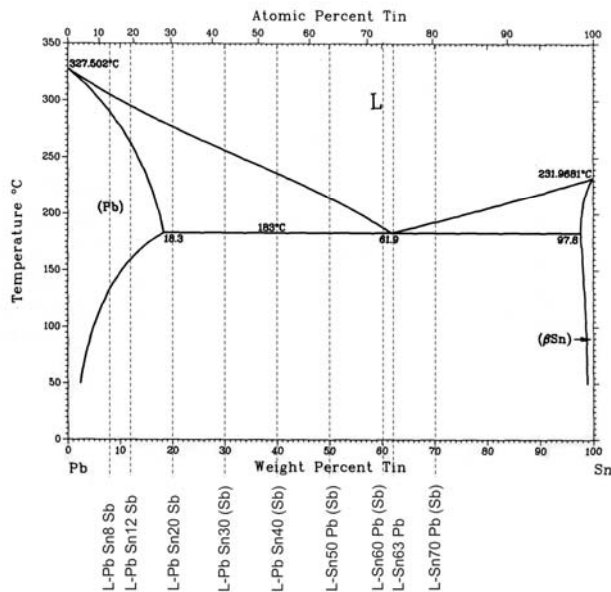
We can subdivide the solder process into the solder method (e.g. torch brazing, hand soldering, resistance brazing, induction brazing, dip brazing, ...), the shape of the soldered point (gap brazing, surfacing by brazing), feeding of the solder material (contact solder, inserted solder, dipped in liquid solder), the atmosphere (vacuum; gaseous: Inert gas; flux agent: Liquid, paste-like, powdered) and the working temperature [1]. There is a rough differentiation in the working temperature between soft soldering ($<450^{\circ}\text{C}$) and hard soldering ($>450^{\circ}\text{C}$), which makes a differentiation between soft and hard solder materials necessary.

2.1 Solder materials

2.1.1 Soft solders

Soft soldering is proceeded at temperatures below 450°C . The typical temperature range for low temperature soft soldering is $180\text{--}230^{\circ}\text{C}$, whereas high temperature soft soldering happens at temperatures between 230 and 450°C . A typical soft solder is an alloy of Pb-Sn, but also combinations based on Sn-Zn, Ag-Sn, Cu-Sn, Cd-Sn and Ag-Pb are used. Soft solders have the benefit of a low melting temperature, this assures a gentle treatment of the solder substrate. The easy handling makes an automating possible, soft solders are mainly used in the electronic industry for the production of electronic circuits. Further application areas are the soldering of copper pipes for water installations, and in the past it was the production of cans made of tin foil by solder automats. The main disadvantage of soft solders is the limited strength of the joints. This is determined by the used solder, in most cases it is in the range of 50 N/mm^2 [1]. Soft solders can be subdivided in light and heavy metal solders.

Fig. 1: Pb-Sn phase diagram for common soft solders [2]



The largest and most important family of soft solders are the Pb-Sn based solders. These solders can consist of different portions of Sn and Pb, whereas in most cases the hypoeutectic solders with a Sn-content lower than the eutectic composition (61.9 wt% = 73.9 at%) is preferred; see Fig. 1. Hypoeutectic Pb-Sn solders have the benefit of a higher corrosion resistance. Hypereutectic Pb-Sn solders (Sn > 61.9 wt%) could easily form

watersoluble Sn-compounds, which could be harmful to the environment and are therefore not widely used. In this context it would be interesting to know, that the recent research on lead free solders (see chapter “lead free high temperature soft solders” below) bases mainly on Sn-rich systems. The detrimental influence of tin-based solder materials on the environment is not well studied by now.

Sometimes also a portion up to 0.5 wt% Sb can occur in the Pb-Sn solders. Sb is an impurity which leads to unwanted mechanical properties, e.g. a decrease in the creep resistance of the soldered joints. A use of Sb-free solders is preferred. Possible additives are Cu (< 1.6 wt%) and Ag (< 4 wt%), which are used to tailor special properties.

Finally, there could be mentioned a wide range of non-standard solders, special solders and very low melting solders. The non-standard solders are derived from the systems Sn-Ag, Sn-Sb, Pb-Ag, Sn-Pb-Cd and Cd-Zn-Ag and are used mainly in the electronic industry. Examples for the special soft solders are the alloys of Pb, Sn, Pb-Au, Pb-In, Pb-Bi-Sn, Au-Sn-Pb, Sn-In, Au-Sn, Au-Ge and Pb-Sn-Ag, which are used for joining less common metals and other materials (Cu, Au, Ag, Sn, Ge, Si, Mo or glass), e.g. for the connection of Si- or Ge-crystals with the socket materials (Cu, Mo). Solders with very low melting points (> 58°C) are binary, ternary or quaternary Bi-based systems with different amounts of Pb, Sn, In, or Cd. These solders are used for special solder purposes at very low temperatures [1], e.g. for safety fuses, embedding metals for turning workpieces and for heat sensitive components.

2.1.2 Hard solders

Hard soldering is used at temperatures higher than 450°C. It can be applied to light metals (e.g. Al and Si), as well as heavy metals (steel, nickel, copper, brass and some other metals). The advantage of hard soldering is the high strength of the obtained joint, which is in the same range as the substrate material. Compared to welding it is easier to handle, has better wetting properties and doesn't enlarge the grain structure. The hard solder process is widely used to produce engine parts, mountings, heat exchangers, containers, bearings, gear wheels and a many other component parts, which can't be welded due to constructional limits, or which are produced on a large scale in automated production.

Hard solders for light metals are mainly based on Al-Si, whereas solders for heavy metals can have a great variety in the used materials. The most common solder alloys are based on Ag-Cd. Other alloys which are used as a hard solder are Cu-Sn, Cu-Zn, Cu-Ni-Zn and Cu-P based solders. Nameable are also the hard solders based on Ag (-Cd, -P-Cu, -Si, -Cu-Zn, Ni-Mn) and some special solders based on noble metals (Au, Pt, Pd). Because this work concerns with Cu-Sn bronzes, we paid attention on this system and the used solders in Table 3.

Table 3: Cu-Sn hard solders [1]

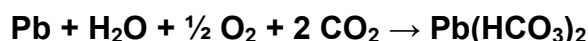
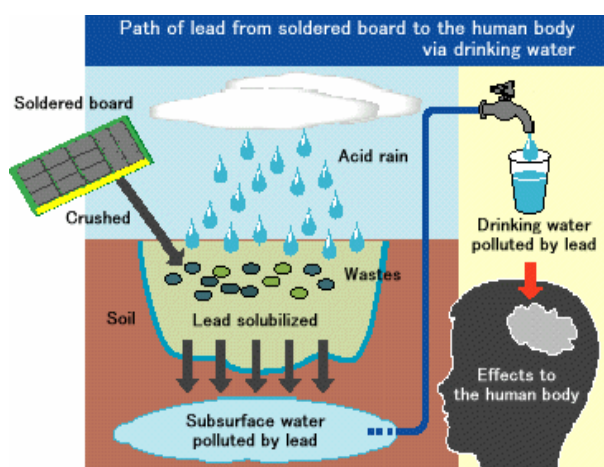
name	composition (wt%)	Melting range (°C)	working temperature (°C)	substrate	trademark
L-SnBz 6 (DIN 8513)	Cu 94 / Sn 6	910-1040	1040	steel, Ni	DE 840
L-SnBz 12 (DIN 8513)	Cu 88 / Sn 12	825-990	990	steel, Ni	DE 830
SL-CuSn12 (ÖNORM M 7825)	Cu 88 / Sn 12	820-990	-	steel, Ni	Metta BG

Alloys made of Cu and Sn are also called tin bronzes. Their melt is usually viscous and bronze-coloured, they are also useable for acid-proof solder joints. The obtained surfaces are resistant against friction and corrosion. In most cases gap soldering with inserted solder is applied [1].

2.1.3 Lead free high temperature soft solders

In the European Union by 2006 the RoHS regulation (Restriction of the use of certain hazardous substances in electric and electronic equipment) was updated in order to ban lead and lead containing substances in electronic devices. This means that formerly used lead containing soft solder materials have to be substituted by less harmful materials.

Fig. 2: Possible liberation of lead into the environment [3]



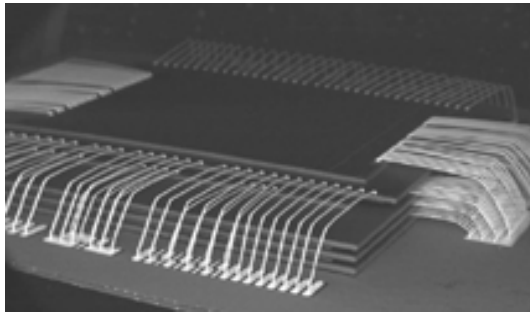
Lead is known as a heavy metal with a high affinity to the proteins of the human body and acts as a severe toxin (threshold value 100µg Pb/l blood, intoxication at 250µg/l [3]). It can be accumulated in the body and leads to disorders in the nervous and reproductive systems, the neurological and physiological development, cognitive and behavioural changes and the production of haemoglobin resulting in anaemia and hypertension [4]. It is estimated, but not really proved by independent studies yet,

that the lead in solder materials can be oxidized and dissolved by rainwater under oxidizing conditions (electronic waste in waste deposit sites; see Fig. 2).

This RoHS regulation affects the low temperature soft solders ($F_p = 180\text{-}230^\circ\text{C}$), which are commonly used for hand soldering and for the most electronic solder purposes in an industrial scale. For the low temperature soft solders alternative systems were already found, with more or less benefits compared to the lead containing ones (e.g. Ag-Cu-Sn, $F_p \sim 220^\circ\text{C}$). These alloys are already used in Japan, Europe and in the USA, but countries like China are currently not able to comply with the European lead free legislation.

High temperature soft solders ($F_p > 230^\circ\text{C}$) often possess a lead content of more than 85 wt%. Despite the fact that the high temperature soft solders are excluded from this regulation, the trend to substitute hazardous substances from solders will continue and the pressure to find new alloys which contain less harmful metals and offer similar properties at the same time will increase.

Fig. 3: Multi chip package (recorded with an electron microscope) [5]



High temperature soft solders, such as the Pb95-Sn5 solder ($F_p = 308-312^{\circ}\text{C}$ [4]), are mainly used for advanced packing technologies, e.g. the die-attach and BGA (Ball Grid Array) solder spheres, the chip-scale packaging (CSP) and the multi-chip modelling (MCM, see Fig. 3) [4]. The die-attach technique is used for heat resistant under-

bonnet-applications in engine. The BGA solder spheres, the CSP and the MCM technique contain a multi-step soldering, where various levels of solders with different melting temperatures are used. An exact knowledge of the melting points of the different solders is necessary.

In addition to the preconditioned properties of a new high temperature soft solder (mechanical and long-term thermal fatigue stress resistance, unsusceptible against pollutants and humidity, good wettability and processability), there is called for a variety of new requirements by the modern chip technology, due to the trend of miniaturization of electronic parts and attended new challenges in material science. In Sn-based materials, negative effects are exacerbated with ongoing miniaturization, e.g. embrittlement, corrosion effects with multilayered metallisations (Ag, Ti, W, Ni, Cu, V [4]), and the formation of tin whiskers which can lead to short circuits [3]. Moreover, the addition of other elements to Sn-based systems to decrease the melting temperature in this range did not provide satisfactory results up to now, therefore the investigations will focus on alloys with another base element in the future. Promising solders seem to be hypoeutectic Bi-Ag [4] and the systems of Zn-Al-X ($X = \text{Mg, Ge, Ga, Sn, Bi}$ [4]), because they are affordable and provide similar properties like the Pb-Sn-based solders, but a lot of research in the description of the properties has to be made for the lead free high temperature soft solders in the future.

3 Literature review

3.1 The elements

3.1.1 Copper (Cu)

Table 4: Element data of Cu [6]

Group	11
Atomic number	29
Molar mass (g mol⁻¹)	63.546
Electron configuration	[Ar] 3d ¹⁰ 4s ¹
Atomic radius (pm)	127.8
Electronegativity	1.90

Fig. 4: Copper wires [7]



Sources and extraction

The main natural mineral deposits of copper ores are in the USA, Peru, Chile and Papua New Guinea. Copper can occur as native copper, as well as the minerals chalcopyrite (CuFeS_2), covellite (CuS) and bornite (Cu_5FeS_4). The sulfidic ores already contain the reductive agent (sulphur). They are molten with chalk and quartz at 1300°C to the so-called copper matte. This is converted with air under the formation of clinker and 99% pure crude copper, which is cast in layers. These layers are refined electrolytically to 99.998% pure copper sheets [8].

History

4000 BC people in Mesopotamia and Europe used copper for producing tools and weapons (Copper Age). Some thousand years later (~ 2000 BC) it was alloyed with tin and other metals to bronzes, which were harder and easier to melt (Bronze Age). Initially the native copper was used, later also copper rich ores were gathered in copper mines and reduced with wood charcoal in copper mills. Nowadays copper has, due to its beneficial properties (corrosion resistance, strength, easy handling, high thermal and electric conductivity), still a very high importance. 10 million tons of copper per year are produced worldwide [8].

Physical properties

The reddish element (Fig. 4) is ductile, soft and forgeable. The melting point is at 1084°C, the boiling point at 2562°C. The density of pure copper is 8.92 g cm⁻³ [8]. Copper crystallizes in the fcc structure (cI4), the crystals have the space group Fm-3m [9]. It is an important metal for alloys (bronzes and brasses) and can be completely mixed with gold. Only pure silver has a higher thermal and electric conductivity [10].

Chemical properties

Copper can easily be oxidized in air at normal temperature, this leads to the reddish Cu-oxide coating. Red heated copper reacts with oxygen to CuO, at higher temperatures Cu₂O is formed. Copper panels, which are exposed in the environment, form with air, water, CO₂ or SO₂ a green patina, which is Cu(HCO₃)₂ or Cu(HSO₄)₂. The metal can be oxidized by halogens, but is not soluble in non-oxidizing acids in the absence of oxygen. With oxygen it is easily soluble in HNO₃ or H₂SO₄, but also in aqueous NH₃ or KCN [10]. Oxidation states of copper are possible between -1 and +4, but common oxidation states are Cu⁰, Cu^I and Cu^{II}. Copper is rather noble with a standard reduction potential of Cu/Cu^{II} of 0.340 V [6].

3.1.2 Tin (Sn)

Table 5: Element data of Sn [6]

Group	14
Atomic number	50
Molar mass (g mol⁻¹)	118.710
Electron configuration	[Kr] 4d ¹⁰ 5s ² 5p ²
Atomic radius (pm)	140.5
Electronegativity	1.96

Fig. 5: Tin ingots [11]



Sources and extraction

The main source for tin is tin stone or cassiterite (SnO_2), sometimes also accompanied by arsenic- or antimony sulfides. It can be found at the so-called “tinbelt”, which is a region at the pacific shores of Southeast Asia. There the tin ore was uncovered by the weathering of the associated minerals feldspath, quartz and mica. Main producers of tin ore are Brazil, Bolivia, China, Indonesia and Malaysia. Here the tin stone is mined in opencast pits.

The ore is reduced in radiation furnaces with coke and chalk, the liquid tin (99.9% pure) is cast in ingots (see Fig. 5). The obtained clinker is heated in the arc furnace again to extract the remaining tin (20% tin in clinker). This dark, glassy remaining clinker is a valuable raw material, it contains the rare metals tantalum, niobium and tungsten, which can be extracted. Finally, the only by-product of the metallurgical process is gaseous carbon dioxide from the reduction of the oxides with coke [8].

History

Tin is known since the antiquity, it was widely used in the ancient cultures in Egypt, Mesopotamia, Greece, China as well as Central- and South America to produce bronzes. The hard bronzes of copper and tin which were used for tools and weapons provided power and fortune to the peoples who knew this technology. In the middle ages people found out, that iron sheets coated with tin could be protected from corrosion. This technology is still important, but nowadays achieved in a large scale continuous production in an electrolytic tin-coating process [8].

Physical properties

The element occurs in two crystallographic modifications: The grey α -tin (stable below 13.25°C, cubic diamond structure, space group Fd3m) and the white β -tin (stable at temperatures higher than 13.25°C, tetragonal, space group I4₂/amd) [6]. The transformation from β - to α -tin occurs at fairly low temperatures, but can be accelerated by nuclei of the α -modification. This process increases the volume by 21% [8]. The density of the common β -tin is 7.31 g cm⁻³. It melts at 231.9°C and has a surprising high boiling point at 2602°C. At the Mohs scale of mineral hardness tin is at 1.8, therefore it is one of the softest metals [8].

Chemical properties

Tin is not reactive with oxygen at room temperature, because it is protected by an oxide film. It is also insoluble in water, but can easily be dissolved by acids and bases. Oxidation states of Tin are Sn⁰, Sn^{II} and Sn^{IV} and Sn^{-IV}. The standard reduction potential of Sn/Sn^{II} is -0.137 V [6]. The pure element is widely used for solders and alloys, especially bronzes. There are some organic tin compounds known, which are used as UV-stabilizers for PVC, as catalysts for polymerization reactions (silicone elastomers) or as antifouling paints for ships (not allowed any more [8]).

3.1.3 Antimony (Sb)

Table 6: Element data of Sb [6]

Group	15
Atomic number	51
Molar mass (g mol⁻¹)	121.75
Electron configuration	[Kr] 4d ¹⁰ 5s ² 5p ³
Atomic radius (pm)	141
Electronegativity	2.05

Fig. 6: Antimony crystals [12]



Sources and extraction

Chief ore is the mineral stibnite (Sb_2S_3), which is mined in Bolivia, South Africa, China and Russia. It is often found with gold, e.g. in the green stone belt in South Africa. Here the ore contains 1.8 wt% antimony and 2g gold per ton. Antimony is only the by-product of the much more valuable gold. In a leaching process with cyanides the gold is separated from the stibnite. The Sb_2S_3 is calcinated at controlled oxygen supply to the Sb_4O_6 , cleaned in another aqueous process and then reduced to the pure element.

History

Antimony was already known by the Sumerians and was alloyed with copper, tin and lead to form bronze. The Egyptians used stibnite for cosmetics and in the ophthalmology. In the middle ages the pure element was used to separate Silver from gold by precipitation of the compound Ag_3Sb . Antimony also played a role in the early pharmaceuticals, it was used as an antiseptic agent and an emetic. The potassium antimony tartrate was prescribed as a drug against bilharziosis, but with several serious side effects [8].

Physical properties

Pure antimony is very brittle and crystallizes in needle-shaped crystals (Fig. 6). The electric conductivity is low (4 % of Cu), therefore it can be considered as a semimetal [8]. Beside the metallic α -state (hexagonal close packed, $P6_3/mmc$) it also exists in two allotropic forms (cubic, $Pm3m$ and rhombohedral, $R-3m$). The melting point is at 630.74°C , the boiling point at 1635°C . The density of antimony is 6.69 g cm^{-3} [6].

Chemical properties

Antimony burns in air with an intense blue flame and reacts to a smoke of Sb_2O_3 . The oxide is soluble in acids as well as bases, and forms antimony salts or antimonates. The oxidation states are $\text{Sb}^{-\text{III}}$, Sb^0 , Sb^{III} and Sb^{V} , but the most common form is Sb^{III} . The element is used for several alloys in accumulators ($\text{Pb} + 8\text{-}12\text{ \% Sb}$, increases tensile strength), letterpress types (Pb-Sn-Sb), gun bullets (Pb-Sb), bearings (Cu-Sb-Sn), solders (1 \% Sb) and III-V-semiconductors ($\text{In / Ga / Al} + \text{Sb}$). The oxides are used for fire-resistant plastics, pigments in ceramics and glasses and as catalysts for polymerizations. Some salts are components of pesticides, etchants and pyrotechnics [8].

3.2 Cu-Sn

3.2.1 Introduction

The Cu-Sn-bronzes were investigated systematically since the end of the 19th century. First papers are dated back to 1894 [13] and 1897 [14], where primarily the liquidus curves were examined. These data from the early works are also used in modern phase diagram assessments[15]. Due to the liquidus lines and some invariant effects, measured with, compared to modern techniques, very archaic methods, the authors [16] made excellent conclusions for the construction of a first complete Cu-Sn phase diagram, which was very similar to current phase diagram versions. Thermal methods (pyrometry), gravimetric and microscopic methods lead to backdraws to the thermal effects, the composition and the phase interactions. Further authors found new invariant effects [17] or new phases [18, 19]. In 1944 the available data were assessed by Raynor [20] to the widely known Cu-Sn phase diagram. At the time of Raynor's publication there were only estimations about the crystal structures at the high temperature phases. The first one who also investigated the high temperature phases systematically was Knödler [21, 22]. He confirmed Raynor's phase diagram and added crystallographic data from the high temperature X-ray diffraction, which was a new and powerful analysis method established in the early 1950's. Until the early 1980's a wide range of X-ray studies were operated, investigating different sections and phases of the phase diagram [9, 23-27]. Two famous publications, which are benchmarks for contemporary scientists, tried to sum up the recent investigations and include the available X-ray data [28, 29]. Recent investigations generate thermodynamic data by the use of mathematical models and try to design a phase diagram by the utilization of experimental data, obtained by earlier studies [30-33].

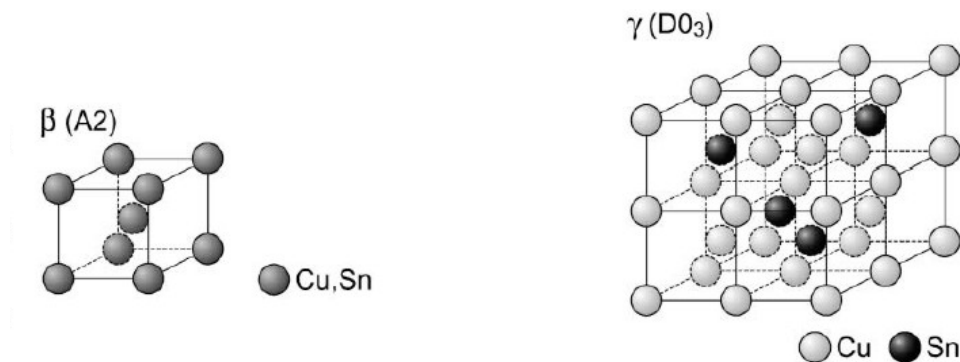
3.2.2 High-temperature phases

The assessment of Saunders and Miodownik [15] (see also Fig. 8) describes two high temperature phases: β and γ .

The β -phase is a W-type structure with the Pearson symbol cI2 and the space group Im-3m [34]. The Cu- and Sn-atoms are randomly arranged at the bcc positions, this means both occupy the same atom sites in an occupation ratio depending from the sample composition.

The γ -phase is a BiF₃-type structure with the Pearson symbol cF16 and the space group Fm-3m. It is similar to the β -phase, the difference can be found in the arrangement of the atoms. The unit cell of the γ -phase can be considered to have the double length of the unit cell of the β -phase, if we double the length in the x-, y- and z-direction, we obtain a unit cell with the volume of 8 β -unit cells. While the Cu-atoms are located at the corners of these β -subcells, the centre of every second subcell is either occupied by a Cu- or a Sn-atom. Fig. 7 should give a better imagination of these two related cell types [31]:

Fig. 7: Beta and gamma structure of Cu-Sn [31]



According to Saunders and Miodownik [15] beta and gamma are separated by a β - γ -two-phase-field. Beta is formed from (Cu), which is a solid solution of Sn in Cu (also called α), and the liquid melt L at 798°C in a peritectic reaction. It decomposes at 586°C in (Cu) and gamma in an eutectoid reaction. This is the reaction, which is very interesting for our own research, because it indicates the attendance of the controversial discussed beta-gamma-two-phase field.

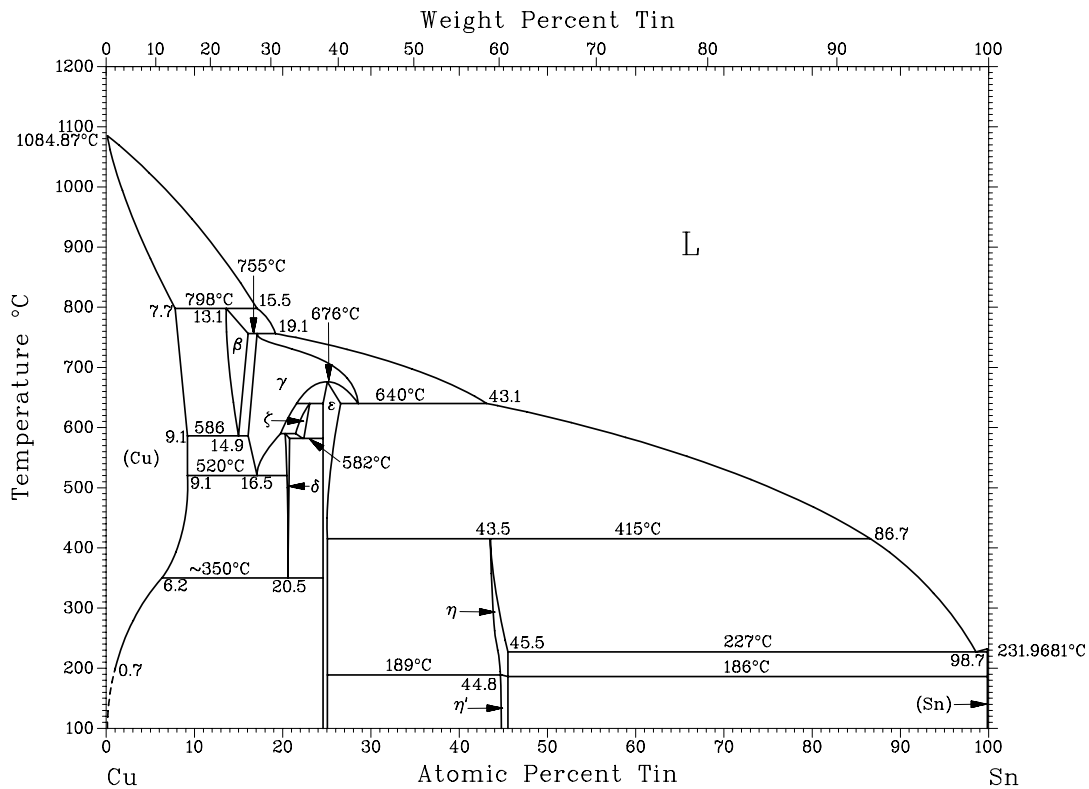
Gamma is much more difficult to describe, because it has a wide range of solubility and rather uncommon shape. It is formed at 755°C from beta and the liquid (peritectic) and decomposes at 520°C in delta and (Cu). At the Sn-rich side it forms congruently the phase epsilon at 676°C and 25 at% Sn. Furthermore, gamma forms with epsilon at 640°C the phase zeta. At the same temperature, but at Sn-contents of more than 25.9 at%, it decomposes into epsilon and the liquid. Gamma forms with zeta at 590°C the phase delta.

The invariant reactions with temperatures and compositions of the Cu-Sn-system are summarized in Table 7. Temperatures and reactions, which concern the β - and the γ -phase, are written in bold letters.

Table 7: Temperature-invariant reactions in the Cu-Sn-system [15]

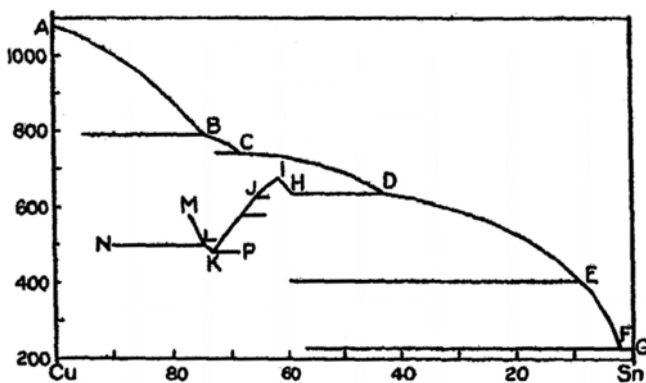
Reaction	Composition at% Sn			Temperature °C	Reaction type
(Cu) + L \rightarrow β	7.7	13.1	15.5	798	Peritectic
β + L \rightarrow γ	15.8	16.5	19.1	755	Peritectic
$\epsilon \rightarrow \gamma$		25.0		676	Congruent
$\gamma + \epsilon \rightarrow \zeta$	21.8	22.5	24.5	640	Peritectoid
$\gamma \rightarrow \epsilon + L$	25.9	27.9	43.1	640	Metatectic
$\gamma + \zeta \rightarrow \delta$	19.8	20.3	20.9	590	Peritectoid
$\beta \rightarrow (Cu) + \gamma$	9.1	14.9	15.4	586	Eutectoid
$\zeta \rightarrow \delta + \epsilon$	20.8	21.7	24.5	582	Eutectoid
$\gamma \rightarrow (Cu) + \delta$	9.1	16.5	20.4	520	Eutectoid
$\epsilon + L \rightarrow \eta$	24.9	43.5	86.7	415	Peritectic
$\delta \rightarrow (Cu) + \epsilon$	6.2	20.5	24.5	350	Eutectoid
$L \rightarrow \eta + (Sn)$	45.5	98.7	>99.9	227	Eutectic

Fig. 8: Current phase diagram version of the Cu-Sn-system [15]



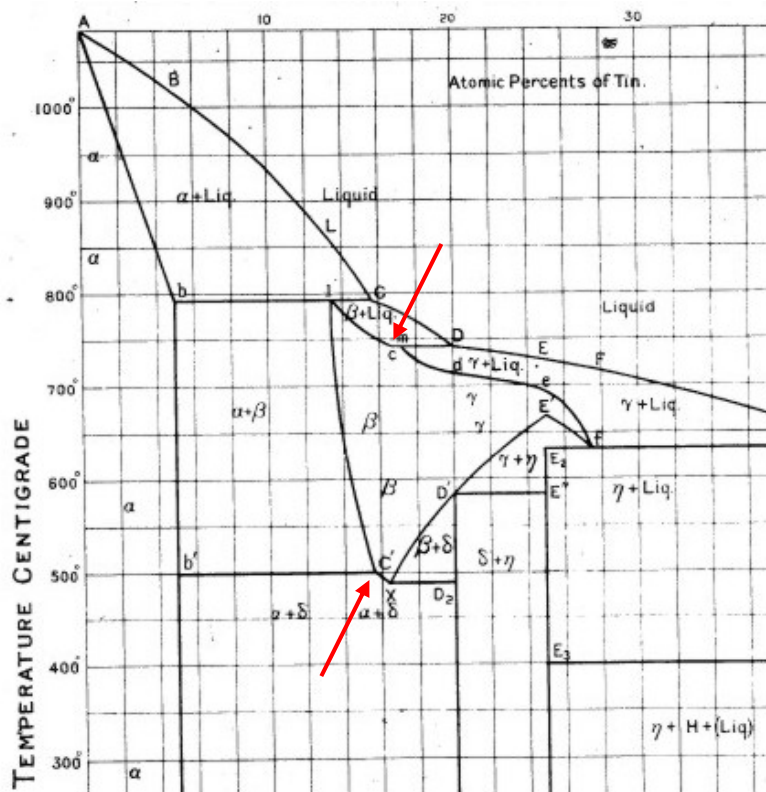
In the following section we want to discuss the development of the Cu-Sn phase diagram in the historic context.

Fig. 9: Stansfield's liquidus and invariant temperatures, cited in [17]



First attempts in finding the liquidus and the invariant reaction temperatures were done by Stansfield in 1897 [17]. He found out that there have to be at least 7 different phases, according to the number of the invariant reaction lines (Fig. 9).

Fig. 10: Section of Heycock and Neville's phase diagram [16]



Stansfield's work was a base for further investigations of Heycock and Neville [16]. They completed the diagram of Stansfield and named the phases (Fig. 10). Their methods were pyrometry (investigation of liquidus and phase transition temperatures), gravimetry (dissolution of Cu and Sn and precipitation of the Cu with electro-gravimetry) and microscopic methods (polishing and etching of the chilled samples, observation

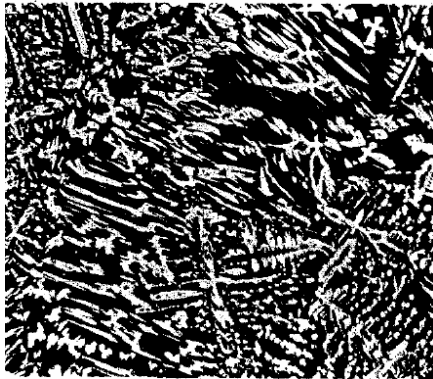
of the crystal orientation and shape). Important to know is that they found a thermal effect which couldn't be explained by a single phase field theory. The arrows in Fig. 10 show two small steps occurring at the invariant reactions at estimated 500 and 740°C. If the point c is equal to the point m at 740°C (respectively the point C' is equal to the point X at 500°C), the authors concluded that also the phase beta and gamma would be equal in their structure. But here in Heycock and Neville's phase diagram the point c is not at the same position as m, therefore the reaction " $\beta + L \rightarrow \gamma$ " would result from this indication.

In 1904 it was still unknown due to a lack of structure analysis methods, that the beta and gamma phase couldn't be quenched fast enough to be stabilized at room temperature. Heycock and Neville took a lot of effort on producing microscopic images from chilled samples, but the interpretation of these ones didn't always lead to the real dimension of the reality. They thought they would observe the high-temperature phases beta and gamma, but only could examine stable low temperature phases, e.g. (Cu) and delta. In Table 8 there are two misinterpretations listed exemplarily. We tried to compare Heycock and Neville's samples with similar compositions and thermal treatments of our own samples.

Table 8: Misinterpretations of high temperature phases

Heycock and Neville (1904)

13.5 at% Sn,
chilled from 558°C:
(Cu) (bright) + β (dark),
reflected-light microscope

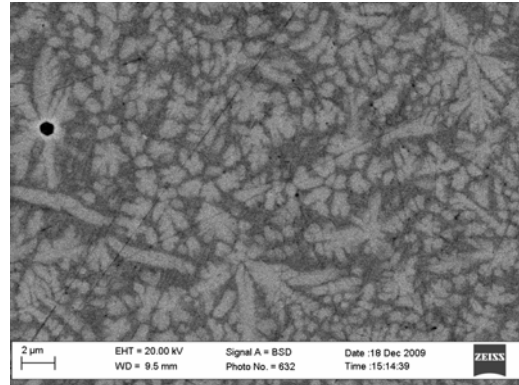


14.0 at% Sn,
very slow chilled from 800°C:
(Cu) (bright) + β (dark),
reflected-light microscope

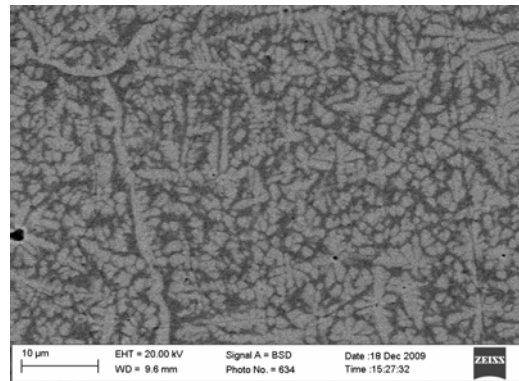


This work (2010)

11.0 at% Sn,
from 700°C quickly chilled:
(Cu) (dark) + δ (bright),
investigated with ESEM – BSE image



15.5 at% Sn,
from 700°C quickly chilled:
(Cu) (dark) + δ (bright),
investigated with ESEM – BSE image



Shepherd and Blough [17] were the first experimentators who mentioned, that the triangular shape of the β - γ -field has to be divided into a β -field, a γ -field and a β - γ -two-phase field (see Fig. 11). They produced a wide range of samples and annealed them at different temperatures. After quenching in water the obtained samples were polished and examined in a microscope. Although they examined their samples with the same methods as Heycock and Neville [16], and they did no X-ray-diffraction or high temperature X-ray-diffraction, they found the presence of the new β - γ -two-phase field in a rather wide composition range. Their argumentation for this β - γ -two-phase field was the fact, that the two invariant reaction lines b' -C' and x-D2 (see Fig. 10, [16]) were at different temperatures. The drawback of this work is the construction of the β - γ -two-phase field, which is based only on assumptions but was never detected by a reliable and independent method like the X-ray diffraction at high temperatures.

Fig. 11: Phase diagram of Shepherd and Blough [17]

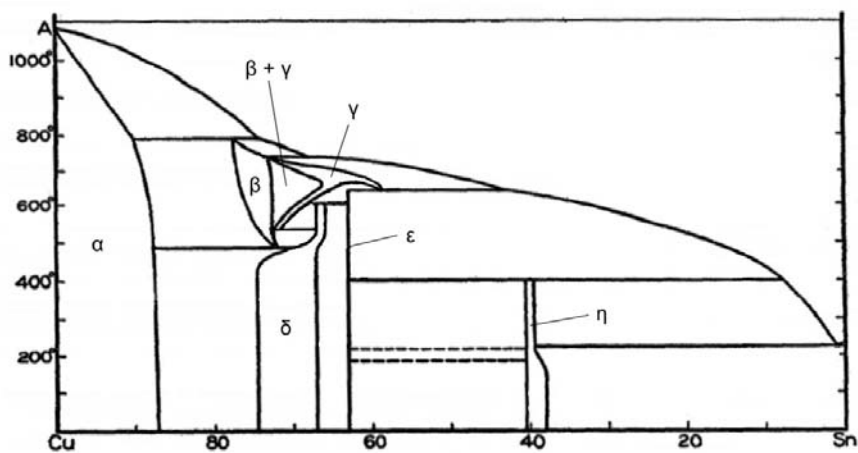


Fig. 12: Small temperature effect at 590°C in pure Cu-Sn-alloys [35]

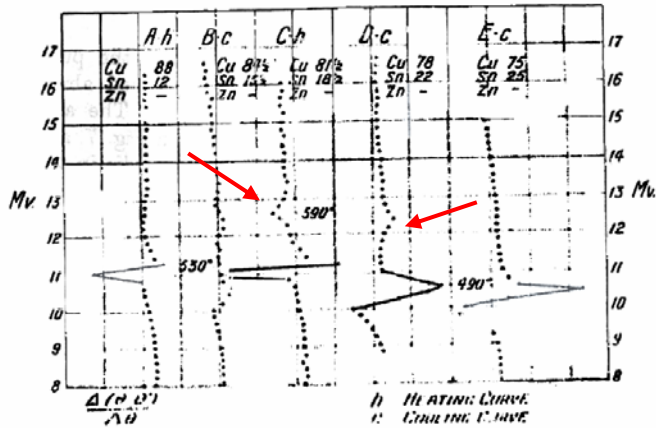
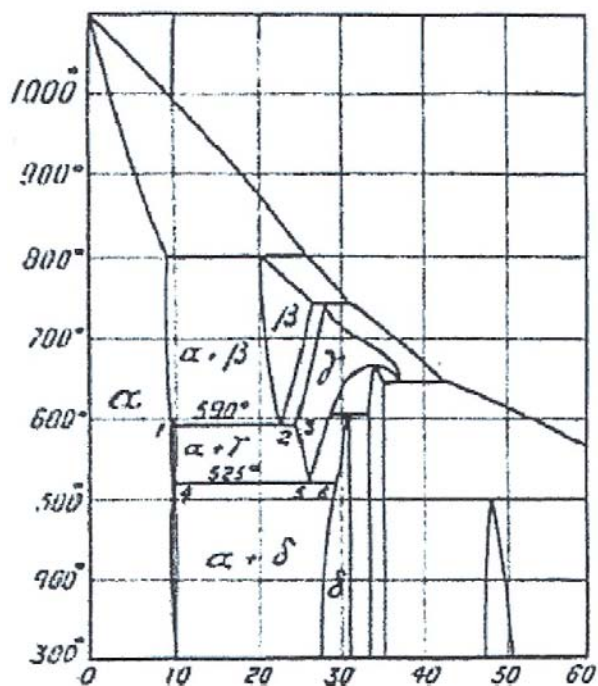
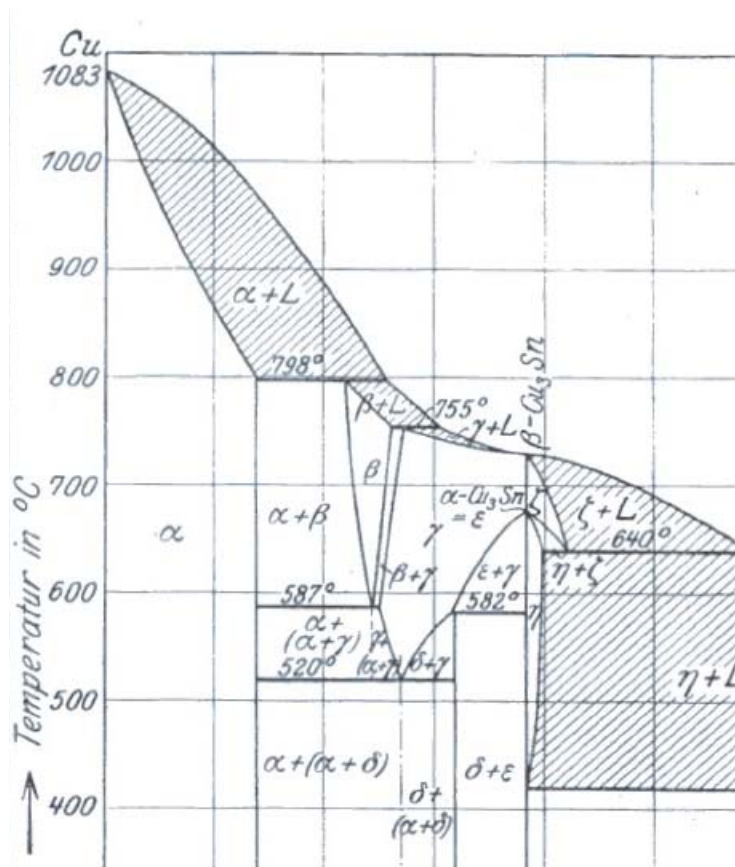


Fig. 13: Section of Hoyt's phase diagram [35]



The next investigator was Hoyt [35, 36]. He found a large temperature effect at 525°C, and also a smaller temperature effect at estimated 590°C in the samples of 10.8 and 13.1 at% Sn (see Fig. 12). In the binary Cu-Sn the smaller effect at 590°C was hardly to see, but by adding a few percent of Zn this effect enlarged. It seemed that the phase transition at 590°C is more stable in the ternary Cu-Sn-Zn-system. He also interpreted micrographs based on Cu-Sn and Cu-Sn-Zn, but his conclusions didn't support the theory of Shepherd and Blough [17], that beta decomposes at 590°C into alpha and delta. Based on the micrographs he interpreted that the two reactions " $\beta \rightarrow (\text{Cu}) + \gamma$ " at 590°C and " $\gamma \rightarrow (\text{Cu}) + \delta$ " at 525°C took place. So he created a phase diagram (Fig. 13), which is very similar to the modern phase diagram in the compilation of Saunders and Miodownik [15]. What Hoyt also didn't know was again the fact that beta and gamma were not quenchable, so he thought that he examined these high temperature phases in his micrographs.

Fig. 14: Section of Bauer and Vollenbruck's phase diagram [37]



According to Hoyt's work, Bauer and Vollenbruck [37] confirmed the presence of the small temperature effect and corrected the temperature to 587°C. The design of the beta and gamma phases was similar (Fig. 14). The gamma phase with more than 25 at% Sn was named as zeta (so-called β -Cu₃Sn) phase, which is formed congruently from the melt at 730°C. At 676°C it forms congruently the eta- or α -Cu₃Sn-phase (in later works: Epsilon phase). The small β - γ -two-phase field was estimated in a range of 0.7 at% Sn below the 755°C

peritectic temperature ($\beta + L \rightarrow \gamma$) and 0.4 at% Sn at 587°C (eutectoid reaction $\beta \rightarrow (\text{Cu}) + \gamma$). The reaction $\beta \rightarrow (\text{Cu}) + \gamma$ (587°C) was located at 14.7 at% Sn, the reaction $\beta + L \rightarrow \gamma$ (755°C) at 16.5 at% Sn.

In 1934 Verö [18] made a literature review of the available works in the early 20th century. There were a lot of different suggestions about the concentration limits, compositions and transition temperatures of the known Cu-Sn phases. Some of them could be considered as speculation, but one attempt of Hamasumi [19] could be an educated guess (Fig. 15). The 520°C line was without any doubts due to the decomposition of one phase into alpha and delta. For the 580°C horizontal line Verö considered two possibilities regarding the nature of this effect. On the one hand it could be a simple eutectoid transformation of beta into alpha and gamma. But on the other hand it could also be a polymorphous transformation (second order transformation) of the beta-phase. For the second and against the first theory three facts were listed in a summary of the previous works.

Fig. 15: Section of Hamasumi and Nishigori's phase diagram [18]

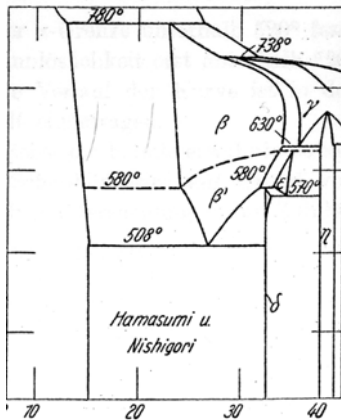


Fig. 16: Section of Verö's phase diagram [18]

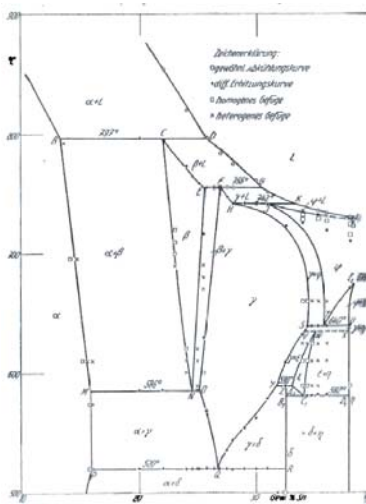
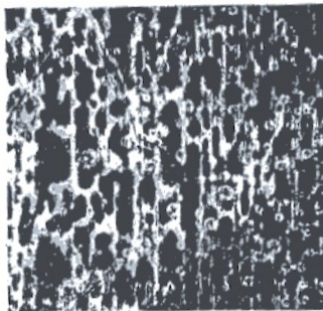


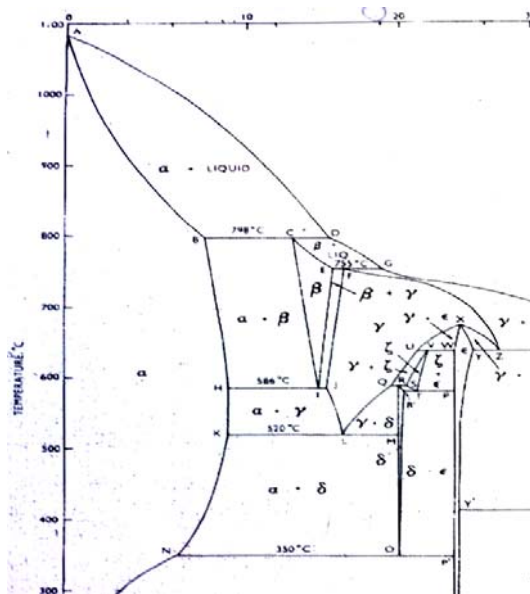
Fig. 17: 15.1 at% Sn, quenched from 595°C, etched with FeCl3. Beta (dark) and gamma (bright)



- No investigator found the β - γ -two-phase field on the estimated position of Bauer and Vollenbruck [37].
- The microscopic studies did not show an eutectoid structure according to the theoretical reaction $\beta \rightarrow (\text{Cu}) + \gamma$ in the (Cu) - γ -two-phase field.
- The $(\text{Cu}) / (\text{Cu})+\beta$ -curve didn't show a change in the slope at 580°C, which would be an evidence for an eutectoid reaction.

Although in the binary no β - γ -two-phase field could ever be detected, Verö mentioned that it existed in the ternary systems Cu-Ni-Sn and Cu-Mn-Sn. Here the 580°C horizontal line was the origin of a new phase field. The theoretical explanation for this phenomenon was that the Ni- or Mn-atoms decreased the transformation speed of the metastable beta-phase. The result was a kinetically stabilized beta phase after quenching in water. In Verö's own research [18] he found 3 peritectic horizontals at 797°C ($(\text{Cu}) + \text{L} \rightarrow \beta$), 756°C ($\beta + \text{L} \rightarrow \gamma$) and at 742°C ($\gamma + \text{L} \rightarrow \phi$), which was a new facet compared to older works (Fig. 16). He introduced the new phase phi, which should be formed at 742°C from gamma and the liquid. Also the presence of the epsilon phase, which was found by Hamasumi and Nishigori [19] (called zeta phase in later works), was confirmed. Although some evidences were against the thesis of an existing β - γ -two-phase field in the binary Cu-Sn, Verö decided to keep it in his phase diagram. As two evidences for the eutectoid reaction at 586°C he finally considered a change in the slope of the $(\text{Cu}) / (\text{Cu})+\beta$ -curve, as well as the micrograph of the supposed β - and γ -phase (Fig. 17).

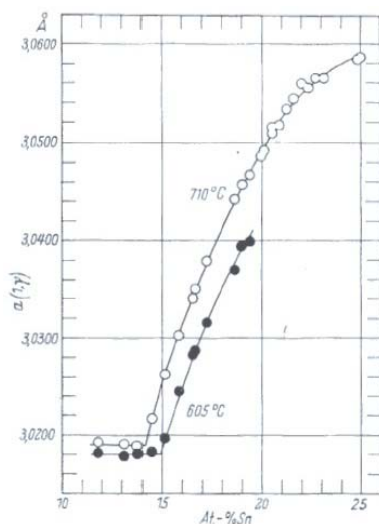
Fig. 18: Section of Raynor's phase diagram [20]



In 1944 Raynor made an assignment of the previous works [20].

His summary leads us to the modern Cu-Sn phase diagram (Fig. 18). Raynor decided for the assumption of the β - γ -two-phase field according to Bauer & Vollenbruck, Verö and Hoyt [18, 36, 37], but admitted that the β - γ -two-phase field borders were not exactly established experimentally. He also corrected Verö's suggestion for the shape of the gamma-phase-field, and referred to Hamasumi's work in 1937 [38], who disproved the presence of the peritectic transformation at 742°C ($\gamma + L \rightarrow \phi$) [18].

Fig. 19: Lattice parameter a vs. composition, 710°C and 605°C [22]



In 1956, Knödler was one of the first investigators who applied X-ray diffraction at high temperatures (700°C, 11.81 – 25 at% Sn). He wanted to show the exact concentration of the transformation from the β -phase to the ordered γ -phase-superstructure. Knödler reported some weak superstructure lines at 15 at% Sn, evidence for the beginning formation of the γ -phase. At 17 at% Sn these lines became rather clear. He also evaluated lattice parameters. Fig. 19, where the cubic lattice parameter “a” is plotted against the composition, shows for different temperatures (710 and 605°C) a continuous slope. This is very

interesting, because the lattice parameters in a two-phase-field is should be constant, whereas only in a single-phase field a continuous slope occurs. The estimated β - γ -two-phase field at 710°C [22] should be between 15.3 and 16.2 at% Sn, this would be evidenced by a step in the graph. But there is no step observable, and due to this indication we can conclude that in this section of the diagram definitely no β - γ -two-phase field can exist.

Fig. 20: Concentration profile of Sn in the Cu/Sn diffusion-couple at 700°C, 1h [31]

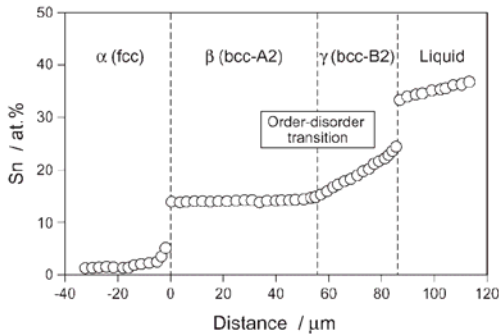
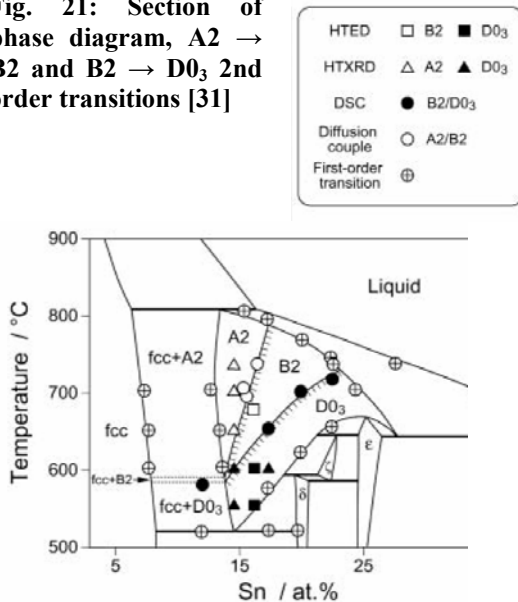


Fig. 21: Section of phase diagram, A2 → B2 and B2 → D0₃ 2nd order transitions [31]



The most recent work about the high temperature phases in Cu-Sn was done 2004 by Liu and coworkers [31]. He investigated the Cu-Sn-system by the use of diffusion-couple method, differential scanning calorimetry (DSC), high-temperature electron diffraction (HTED) and high temperature X-ray diffraction (HTXRD). Contrary to the former authors he decided to give up on the β - γ -two-phase field theory. He postulated a third intermediate structure of the B2(CsCl)-type, separating β (A2) and γ (D0₃). He found out in his diffusion-couple experiments at 700°C, that there is only a change in the slope at the Sn-content between the bcc-A2- and the γ -(bcc-B2)-phase, which indicates an order-disorder-transition (Fig. 20). If there was an abrupt discontinuity observable in the graph, as it was between (Cu)/ β and γ (bcc-B2)/liquid, this would indicate a two-phase field connecting the β and γ phase. He suggests that this shape of the graph is due to the difference of the

interdiffusivity of atoms in the A2 and B2 structures. This is a further evidence disproving the theory of an existing β - γ -two-phase field. By using DSC he found out another second-order transition of γ (bcc-B2) to γ (bcc-D0₃) at 649°C for the composition 16.9 at% Sn. At the composition 12 at% Sn he found the existence of the reaction γ (D0₃) → (Cu) (fcc) + δ at 515°C and suggested for the signal at 574°C a reaction that corresponds to the second-order transition in the β -phase. His results of the HTED and HTPXRD proved this theory, so he was able to construct a new phase diagram with the second-order transitions β (A2) → γ (B2) → γ (D0₃). The first order reactions at estimated 580°C (β → (Cu) + γ) and at 755°C (liq + β → γ) were disproved in his research (see Fig. 21).

3.2.3 Phases in Cu-Sn

Table 9: Crystallographic data of Cu-Sn phases

phase	Stoichiometry	type	Pearson symbol	Space group	No.	a (Å)	b (Å)	c (Å)	β (°)	Ref.
α	(Cu)	Cu	cF4	Fm-3m	225	3.61443	-	-	90	[9]
β	Cu ₁₇ Sn ₃	W	cI2	Im-3m	229	3.0261	-	-	90	[34]
γ	Cu ₃ Sn	BiF ₃	cF16	Fm-3m	225	6.1176	-	-	90	[34]
B2-bcc	No data av.	CsCl	cP2	Pm-3m	221	No data available			90	[31]
δ	Cu ₄₁ Sn ₁₁	Cu ₄₁ Sn ₁₁	cF416	F-43m	216	17.98	-	-	90	[26]
ϵ	Cu ₃ Sn	Cu ₃ Ti	oC80	Cmcm	63	5.529	47.75	4.323	90	[39]
ζ	Cu ₁₀ Sn ₃	ζ AgZn	hP26	P6 ₃	173	7.330	-	7.864	90	[40]
η	Cu ₆ Sn ₅	AsNi	hP4	P6 ₃ /mmc	194	4.192	-	5.037	90	[24]
η'	Cu ₆ Sn ₅	η' -Cu ₆ Sn ₅	mC44	C2/c	15	11.022	7.282	9.827	98.84	[41]
(Sn)	Sn	Sn	tI4	I41/amd	141	0.5832	-	0.3181	90	[42]

All crystallographic data of the Cu-Sn phases are listed in Table 9. The α phase is fcc copper with a maximum solubility of Sn reported 9.1 at% at 520°C [29]. The cubic δ phase consists of 413 atoms per unit cell and can be considered as a γ -brass type superstructure, where ordering prevents any close contact between the Sn-atoms [26]. It is formed at 590°C ($\gamma + \zeta \rightarrow \delta$) and decomposes at estimated 350°C ($\delta \rightarrow (\text{Cu}) + \epsilon$). The concentration range reaches from 20 to 21 at% Sn [29]. The orthorhombic ϵ phase has a Cu₃Ti-type based structure. It crystallizes in a long-period superstructure with an antiphase shift at every five unit cells along the b-axis. The Cu₃Ti-structure itself is based on the cph A3 lattice, thus ϵ belongs to the family of the cph-based antiphase structures [27]. The stoichiometry is Cu₃Sn, therefore it exists at 25 at% Sn with a composition range of 24.5-25.9 at% Sn. It is formed congruently at 25 at% Sn and 676°C from the γ -phase [29]. The ζ phase is a hexagonal superstructure isotypic to ζ AgZn [25]. It is formed at 640°C ($\gamma + \epsilon \rightarrow \zeta$) and decomposes at 582°C ($\zeta \rightarrow \delta + \epsilon$). The concentration range is between 20.3 and 22.5 at% Sn [29]. The monoclinic η' structure [41], based on the NiAs-type structure, transforms at 186-189°C to the conventional NiAs-type structure η , which is hexagonal hP4 [29]. η is formed at 43.5 at% Sn and 415°C ($\epsilon + \text{L} \rightarrow \eta$) and has a concentration range between 43.5 and 45.5 at% Sn. The (Sn)-phase, finally, exists at temperatures higher than 13°C and at 1 bar in the bct (tI4) structure and has a reported solubility of copper lower than 0.01 at% Cu [29].

3.3 Cu-Sb

The Cu-Sb phase diagram, as drawn in Massalski [43], is presented in Fig. 22. The invariant reactions are listed in Table 10, as well as the crystallographic data in Table 11.

The α -phase is Cu with a certain solubility of Sb. The maximum solubility of Sb in Cu is about 5.8 at% Sb at 645°C [43]. In contrast to this, there is nearly no solubility of Cu in Sb, which is sometimes labelled as the θ -phase [43]. The β -phase, which is a high temperature phase (not stable at room temperature, not quenchable), melts congruently at 683°C. It crystallizes in a cubic BiF₃-type structure (D0₃) with the space group Fm-3m, and is isotypic to the γ -phase in the Cu-Sn system. Sb-rich β forms with the liquid melt the η -phase in a peritectic reaction (586°C). At the Cu-rich side β and (Cu) are formed in an eutectic reaction from the liquid at 645°C. The β -phase decomposes in an eutectoid reaction at 440°C into ε and η . Schubert and Illschner [44] supported this reaction, whereas Heumann and Heinemann [45] found the eutectoid reaction $\beta \rightarrow \delta + \varepsilon$ at 436°C and 22.3 at% Sb from micrographic data. Hansen [46] and later Massalski [43] did not pay attention to the version of Heumann and Heinemann in their assessments, but established the eutectoid decomposition of $\varepsilon \rightarrow \delta + \eta$ at 375°C, also determined by micrographic data from Heumann and Heinemann's work [45]. Later, Günzel and Schubert [47] described a new phase ζ occurring at the Sb-rich side of δ . Therefore the last-mentioned reaction had to be corrected to $\varepsilon \rightarrow \zeta + \eta$ (adjusted from 375 °C to 360°C). β also forms the γ phase with (Cu) in the peritectoid reaction $(\text{Cu}) + \beta \rightarrow \gamma$ (488°C). This one and the peritectoid reaction $\gamma + \beta \rightarrow \delta$ (462°C) were found by Japanese scientists [48] and confirmed by Schubert [44] with dilatometric methods. The ε -phase was first mentioned by Schubert and Illschner [44]. They tentatively fixed the belonging reaction temperatures and the concentration limits according to their high-temperature X-ray diffraction results. The invariant peritectoid temperatures of the reactions $\beta + \delta \rightarrow \varepsilon$ (445°C), $\delta + \varepsilon \rightarrow \zeta$ (390°C) as well as the eutectoid decomposition of ζ ($\zeta \rightarrow \delta + \eta$; 280°C) were estimated by Günzel and Schubert [47] from X-ray diffraction experiments. They estimated the peritectoid temperature ($\delta + \varepsilon \rightarrow \zeta$) at 390°C, but there is the uncertainty that this reaction could occur at temperatures of 375-400°C. The temperature of decomposition ($\zeta \rightarrow \delta + \eta$) is suggested to be 260°C, but this temperature can be located between 250 and 300°C.

We could not find out which author described the eutectoid reaction $\gamma \rightarrow (\text{Cu}) + \delta$ at 400°C at first. We suppose that this temperature is also an assumption of former microscopic analysis and high-temperature X-ray diffractions.

It can be summarized that some reaction temperatures are not really exactly determined, which is shown by dashed lines in the assessment of the Cu-Sb-system by Massalski [43].

Fig. 22: Current phase diagram version of the Cu-Sb system [43]

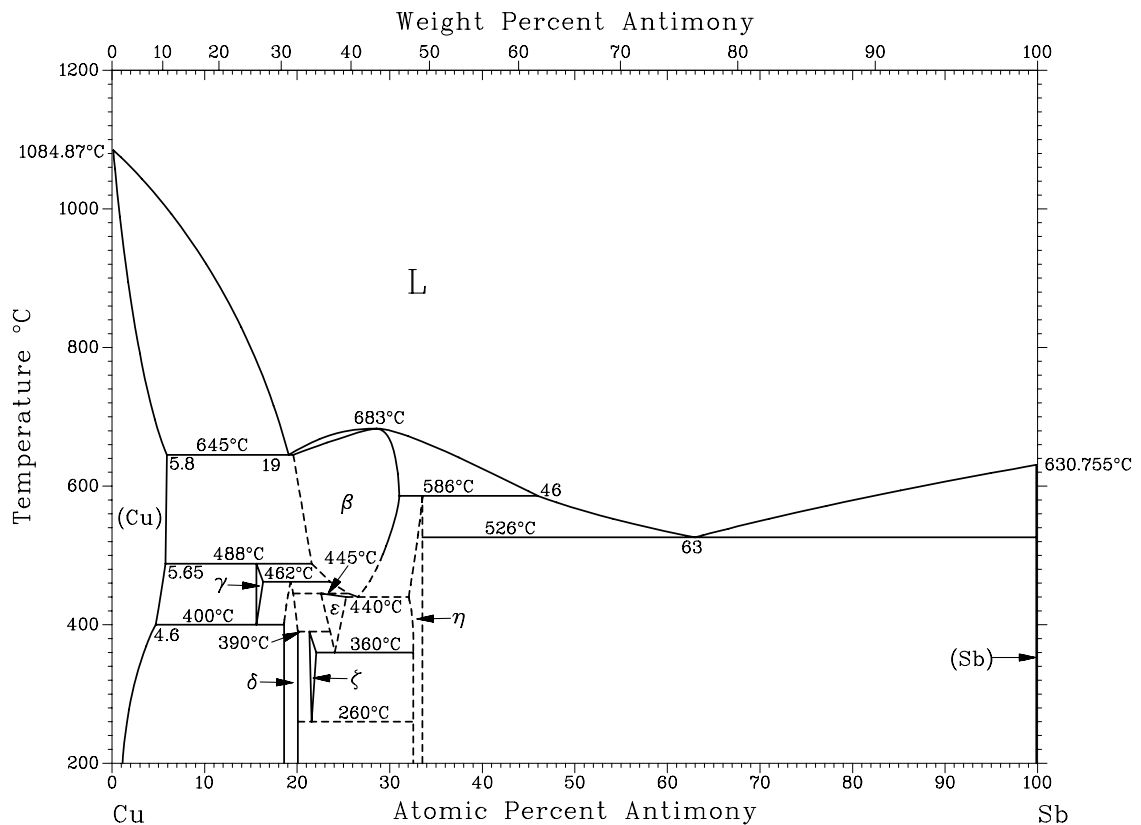


Table 10: Temperature-invariant reactions in the Cu-Sb-system [43]

Reaction	Composition at% Sb			Temperature °C	Reaction type
$L \rightarrow \beta$		29		683	Congruent melting
$L \rightarrow (Cu) + \beta$	5.8	19	19.5	645	Eutectic
$L + \beta \rightarrow \eta$	31	33.5	46	586	Peritectic
$L \rightarrow \eta + (Sb)$	33.5	63	99.9	526	Eutectic
$(Cu) + \beta \rightarrow \gamma$	5.65	15.5	21.5	488	Peritectoid
$\beta + \gamma \rightarrow \delta$	16.5	19	24	462	Peritectoid
$\beta + \delta \rightarrow \varepsilon$	19.5	23	25.5	445*	Peritectoid
$\beta \rightarrow \varepsilon + \eta$	25.5	26.5	32	440*	Eutectoid
$\gamma \rightarrow (Cu) + \delta$	4.6	15.5	18.5	400	Eutectoid
$\delta + \varepsilon \rightarrow \zeta$	20	21.5	23.5	390*	Peritectoid
$\varepsilon \rightarrow \zeta + \eta$	22.5	24	32.5	360	Eutectoid
$\zeta \rightarrow \delta + \eta$	20	21.5	32.5	260*	Eutectoid

* uncertain temperatures

Table 11: Crystallographic data of Cu-Sb phases

phase	Stochio- metry	type	Pearson symbol	Space group	No	a (Å)	b (Å)	c (Å)	Ref.
α	(Cu)	Cu	cF4	Fm-3m	225	3.6130	-	-	[49]
β	Cu ₃ Sb	BiF ₃	cF16	Fm-3m	225	6.0000	-	-	[50]
γ	Cu ₄ Sb	Mg	hP2	P63/mmc	194	2.7520	-	4.3200	[51]
δ	Cu ₇₈ Sb ₂₀	Cu ₇₈ Sb ₂₁	hP98	P63/mmc	194	19.124	-	4.324756	[52]
ε	Cu ₃ Sb	Cu ₃ Ti	oP8	PmmnZ	59	5.5040	4.3530	4.7680	[53]
ζ	Cu ₁₀ Sb ₃	Cu ₁₀ Sb ₃	hP26	P-3	147	9.9200	-	4.3200	[54]
η	Cu ₂ Sb	Cu ₂ Sb	tP6	P4/nmm	129	4.0014	-	6.1044	[55]
θ	(Sb)	As	hR2	R-3m	166	4.3084	-	11.2740	[56]

Fig. 24: Transformation $\text{DO}_{19} \rightarrow \text{BiF}_3$ [47]

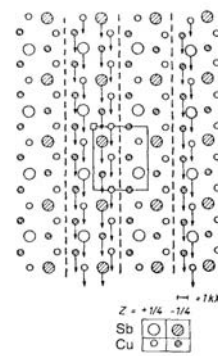
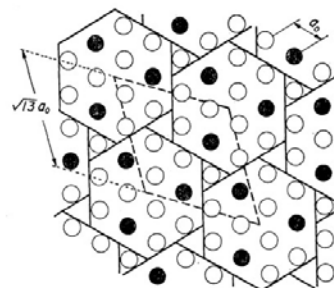


Fig. 26: ζ -phase [52]



4 Experimental section

4.1 Sample preparation of Cu-Sn

As discussed in the literature review, the current phase diagram of Raynor [20], found in the compilation of Saunders and Miodownik [15], was used as a base for our investigations. The idea was to produce samples which represented two-phase-fields at 400°C. Table 12 specifies the main compositions which were chosen. Some other samples were produced later at the compositions listed in Table 13.

Table 12: Cu-Sn: Main sample compositions

sample	atomic percentage (at%)		weight percentage (wt%)	
	Cu	Sn	Cu	Sn
CS_F_01	89.00	11.00	81.24	18.76
CS_F_02	84.50	15.50	74.48	25.52
CS_F_03	81.50	18.50	70.22	29.78
CS_F_04	79.00	21.00	66.82	33.18
CS_F_05	76.00	24.00	62.90	37.10
CS_F_06	72.50	27.50	58.53	41.47

Table 13: Cu-Sn: HTPXRD sample compositions

sample	atomic percentage (at%)	
	Cu	Sn
CS_F_12.5	87.5	12.5
CS_F_13	87.0	13.0
CS_F_13.5	86.5	13.5
CS_F_14	86.0	14.0
CS_F_14.5	85.5	14.5
CS_F_15	85.0	15.0
CS_F_15.5	84.5	15.5
CS_F_16	84.0	16.0
CS_F_16.5	83.5	16.5
CS_F_17	83.0	17.0
CS_F_17.5	82.5	17.5

sample	atomic percentage (at%)	
	Cu	Sn
CS_F_18	82.0	18.0
CS_F_19	81.0	19.0
CS_F_20	80.0	20.0
CS_F_21	79.0	21.0
CS_F_22	78.0	22.0
CS_F_23	77.0	23.0
CS_F_24	76.0	24.0
CS_F_25	75.0	25.0
CS_F_26	74.0	26.0
CS_F_27	73.0	27.0
CS_F_28	72.0	28.0

With the simple formulas

$$\text{at}\%_x = (n_x / (n_x + n_y)) * 100\% = ((\text{wt}\%_x / M_x) / ((\text{wt}\%_x / M_x) + (\text{wt}\%_y / M_y))) * 100\%$$

$$\text{wt}\%_x = m_x / (m_x + m_y) * 100\% = ((\text{at}\%_x * M_x) / ((\text{at}\%_x * M_x) + (\text{at}\%_y * M_y))) * 100\%$$

$\text{at}\%_x$ atomic percent of component X in (%)

$\text{wt}\%_x$ weight percent of component X in (%)

n_x molar amount of component X in (mol)

m_x mass of component X in (g)

M_x molecular weight of component X in (g mol^{-1})

the atomic percentage was converted into weight percentage and related to 2g total mass of the sample.

Used materials for the samples were copper-wire (99.999% pure, surface-coating oxides were initially reduced with hydrogen at 200°C and stored in a protective atmosphere of Argon) and tin-ingot (99.999% pure). At first the tin was roughly weighed, the amount of equivalent copper calculated and finally the exact amount of copper added. The metals were cut with conventional nippers, the final weight adjustment of copper was done with a piece of grinding paper (type 600). In the end the relative error in weighing was about 0.001% and therefore negligible.

Fig. 27: Chill-moulds of the arc furnace



Fig. 28: CS_F_01, after arc furnace, diameter ~7mm

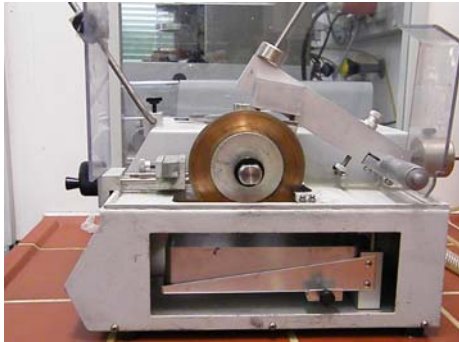


The mixtures of pure copper- and tin- pieces were molten in an arc furnace. This device consists of a water-cooled copper plate with six chill-moulds to contain the samples (Fig. 27). The plate was installed at the bottom of a cylindrical-shaped chamber with a protective atmosphere of argon inside. In the central mould there was inserted a zirconium pill, which should gather remaining oxygen. At the copper plate a tungsten-bolt, which was used for the ignition of the electric arc, was mounted. By touching this positive electrode with the negative, but movable electrode (also made of tungsten), an electric arc was initiated. This arc could be first moved to the zirconium pill and then to

one chill-mould with the pure metals inside. There it caused an immediately melting of the

copper and tin pieces. After a few seconds a nearly homogenous alloy of copper and tin was produced (Fig. 28). To get fully homogenous samples, this procedure was repeated three times with turning the samples upside down before starting the new melting process.

Fig. 29: Diamond saw



To prepare the samples for further analysis, the obtained cooled beads were cut into pieces. If the samples were ductile and not too brittle (< 24 at% Sn), a diamond saw was used (Fig. 29). The samples were fixed in a specimen holder and a small piece (approximately one third of the initial sample size) was separated. The sawing blade was cooled in a bath of special saw lubricant, the contact pressure could be adjusted with different kinds of balance weights. At the end the pieces were cleaned in a bath of acetone in the ultrasonic cleaner. If brittle samples (> 24 at% Sn) were fixed in the specimen holder, a breaking off of the sample could occur. To prevent this problem, a mortar and a chisel were used, the considered samples were broken with a careful hit.

Fig. 30: Quartz glass tubes CS_F_01-06



Fig. 31: Samples in Mo-foil



The larger pieces of the samples were sealed in quartz glass tubes under vacuum (Fig. 30). Before the tubes were finally sealed, the inside was purged 2-3 times with argon gas. For convenient reasons, samples which should be annealed at the same temperature were sometimes wrapped in molybdenum foil and stacked in a longer quartz glass tube with a larger diameter (Fig. 31). The quality of the vacuum was tested by applying an induction current with a tesla coil. If the pressure inside the quartz glass tube was in the dimension of $10^{-3} - 10^{-4}$ mbar, which would have been sufficient to prevent oxidation in the furnace, the

remaining Ar-atoms were excited and emitted a bluish light. Each sample (except the arc-samples) was first annealed at 400°C for at least one week. Finally the samples were annealed at the annealing temperature (400 or 700°C) for two weeks (see Table 14).

Table 14: Cu-Sn: Annealing temperatures and applied methods

sample	atomic percentage (at%)		Annealing temperature (°C)			Analyzing methods				
	Cu	Sn				DTA	Micro-graphs	PXRD	HTPXRD	EPMA/ESEM
CS_F_01	89.0	11.0	arc	400	700	X	X	X	X	X
CS_F_12.5	87.5	12.5	arc	400						
CS_F_13	87.0	13.0	arc	400		X				
CS_F_13.5	86.5	13.5	arc	400						
CS_F_14	86.0	14.0	arc	400		X				
CS_F_14.5	85.5	14.5	arc	400						
CS_F_15	85.0	15.0	arc	400		X			X	
CS_F_15.5	84.5	15.5	arc	400		X				
CS_F_02	84.5	15.5	arc	400	700	X	X	X	X	X
CS_F_16	84.0	16.0	arc	400		X			X	
CS_F_16.5	83.5	16.5	arc	400						
CS_F_17	83.0	17.0	arc	400		X			X	
CS_F_17.5	82.5	17.5	arc	400						
CS_F_18	82.0	18.0	arc	400		X			X	
CS_F_03	81.5	18.5	arc	400	700	X	X	X	X	X
CS_F_19	81.0	19.0	arc	400		X				
CS_F_20	80.0	20.0	arc	400		X				
CS_F_21	79.0	21.0	arc	400						
CS_F_04	79.0	21.0	arc	400	700	X	X	X	X	X
CS_F_22	78.0	22.0	arc	400						
CS_F_23	77.0	23.0	arc	400						
CS_F_24	76.0	24.0	arc	400					X	
CS_F_05	76.0	24.0	arc	400	700	X	X	X	X	X
CS_F_25	75.0	25.0	arc	400						
CS_F_26	74.0	26.0	arc	400						
CS_F_27	73.0	27.0	arc	400						
CS_F_06	72.5	27.5	arc	400	700	X	X	X	X	X
CS_F_28	72.0	28.0	arc	400						

It was assumed that during the heat treatment in the furnace the phases will reach an equilibrium state. This means that the composition and the temperature of the sample will describe well defined points in our phase diagram.

After keeping the samples in the furnace for two weeks they were immediately thrown into a water bath (cold water from the tap), to “freeze” the phase equilibrium state of the annealing temperature (the cooling procedure is called “quenching”). A piece of the obtained samples (400°C) was cut, cleaned and weighed. If its mass was between 100 and 150mg and it still was a single piece, it was sealed in a quartz glass tube with a connected tube of a smaller diameter at its bottom. This special tube was used for differential thermal analysis in closed crucibles (Netzsch DTA 404S). Another piece was cut like a cube and straightened at one side. The mass of this cube was between 150 and 200 mg and it was used for the more sensitive DTA measurement in open crucibles with the Setaram Setsys Evolution.

Fig. 32: Embedded and polished samples



Fig. 33: Automatic grinder and polisher



One larger piece was embedded in a conductible plastic matrix, grinded planar and polished (Fig. 32). An automatic grinder with adjustable contact pressure and rotational speed was used (Fig. 33). The grinding was done with commercially available grinding papers with a roughness between 400-1200 (400 was the roughest, 1200 the finest grinding paper), starting with the roughest and finishing with the finest one. The lubricant and cooling agent was water. The polishing was similar to the grinding, instead of the grinding paper a soft fabric plate with applied abrasive corundum powder (1 μ m and 0.3 μ m) was used. Between the grinding and polishing steps

the grinder, the plate and the samples were carefully cleaned (specimen holding rings and samples in water in ultrasonic cleaner). After the last step the samples were finally cleaned in ethanol and dried with a soft tissue. The surface of the sample was checked for scratches in the dark-field-mode of the reflected-light microscope.

The other part of the samples was crushed again in the mortar. The remaining debris was milled in another molybdenum mortar until the grain size was smaller than 0.18 mm. The more ductile samples (< 15 % Sn) were milled in a ball mill, screened with a sieve (wire distance 0.18 mm) and stress annealed for 15 min at the considered annealing temperature.

The powder was used for measurements in the room temperature powder-X-ray-diffractometer (PXRD) and in the high-temperature-powder-X-ray-diffractometer (HTPXRD).

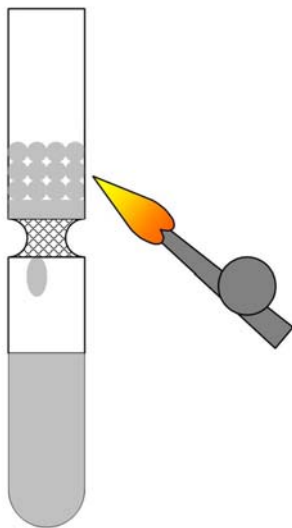
4.2 Sample preparation of Cu-Sb

The origin of our investigations was the Cu-Sb phase diagram described by Massalski [43]. To check temperature and concentration ranges of the phases, samples with a composition between two estimated single phases, as given in the phase diagram, have been produced (see Table 15).

Table 15: Cu-Sb sample compositions

sample	atomic percentage (at%)		weight percentage (wt%)	
	Cu	Sb	Cu	Sb
CA_F_01	90.00	10.00	82.45	17.55
CA_F_02	82.50	17.50	71.10	28.90
CA_F_03	79.00	21.00	66.26	33.74
CA_F_04	77.50	22.50	64.26	35.74
CA_F_05	72.00	28.00	57.30	42.70
CA_F_06	60.00	40.00	43.91	56.09
CA_F_07	70.00	30.00	54.91	45.09

Fig. 34: Sb purifying



The samples were produced from Cu-wire (99.999% clean, surface oxides reduced with H_2) and Sb (99.999%). Antimony was cleaned from oxides by melting and filtering the melt through glass wool (Fig. 34). The weighed Cu and Sb portions were sealed in a quartz glass tube in vacuum and molten for a few hours at $1000^\circ C$ in the furnace. To assure a homogeneous mixture, the liquid samples were swung from time to time. After cooling in water, the pieces were carefully split in a mortar. The fragments were sealed again in quartz glass tubes and annealed for 4 weeks at certain temperatures (see Table 16) in the furnace. After this time they were quenched in

water. A part of each sample was powdered with the mortar for the PXRD analysis. A larger, single piece of each sample was embedded in a plastic matrix, grinded and polished. The last polishing step was done with $1\mu m$ corundum in an organic solvent (Metadi®) to prevent oxidation of the surface in air. Cleaning of the embedded samples was done in ethanol with

the supersonic cleaner. These polished samples were used for the EPMA/ESEM-analysis, as well as for the microscopic analysis.

Another piece of each sample which was annealed at 340°C was sealed in a DTA-quartz glass tube, and used for the DTA analysis with closed crucibles (Netzsch DTA 404S). Additionally, after this DTA measurement these samples were again annealed at 340°C for four weeks, afterwards unsealed and measured for a second time, but this time in open crucibles (Setaram Setsys Evolution).

Table 16: Cu-Sb: Annealing temperatures and applied methods

sample	atomic percentage (at%)		Annealing temperature (°C)						Analyzing methods			
	Cu	Sb							DTA	Micro-graphs	PXRD	EPMA ESEM
CA_F_01	90.0	10.0	arc	340			470	600	X	X	X	X
CA_F_02	82.5	17.5	arc	340	430		470	600	X	X	X	X
CA_F_03	79.0	21.0	arc	340	430		470		X	X	X	X
CA_F_04	77.5	22.5	arc	340	430	450	470	600	X	X	X	X
CA_F_05	72.0	28.0	arc	340	430			600	X	X	X	X
CA_F_06	60.0	40.0	arc	340			470	600	X	X	X	X
CA_F_07	70.0	30.0			430		470	600	X	X	X	X

4.3 Measurement systems

4.3.1 Differential Thermal Analysis Netzsch DTA 404S

The DTA allows the examination of phase transitions at higher temperatures. Due to the fact that a phase transition is always connected to a heat effect, this effect can be measured by a temperature sensor and indicates invariant or non-invariant reactions, which configure our phase diagram. The device is quite simple, although the achieved sensitivity makes it susceptible to rather fast variations in temperature. The main part is a tubular furnace and a ceramic, T-shaped specimen holder with a thermocouple on each of its ends (see Fig. 35). At one thermocouple the reference substance (Ni) and at the other one the sample is mounted. Both, reference substance and sample are located in a closed and evacuated quartz glass crucible with a short quartz glass tube on the bottom to be attached at the specimen holder (Fig. 36). In case that the reference substance shows no phase transitions in the temperature interval, the heat difference between the sample and the reference count for thermal effects in the sample.

Fig. 35: Open DTA furnace with crucibles

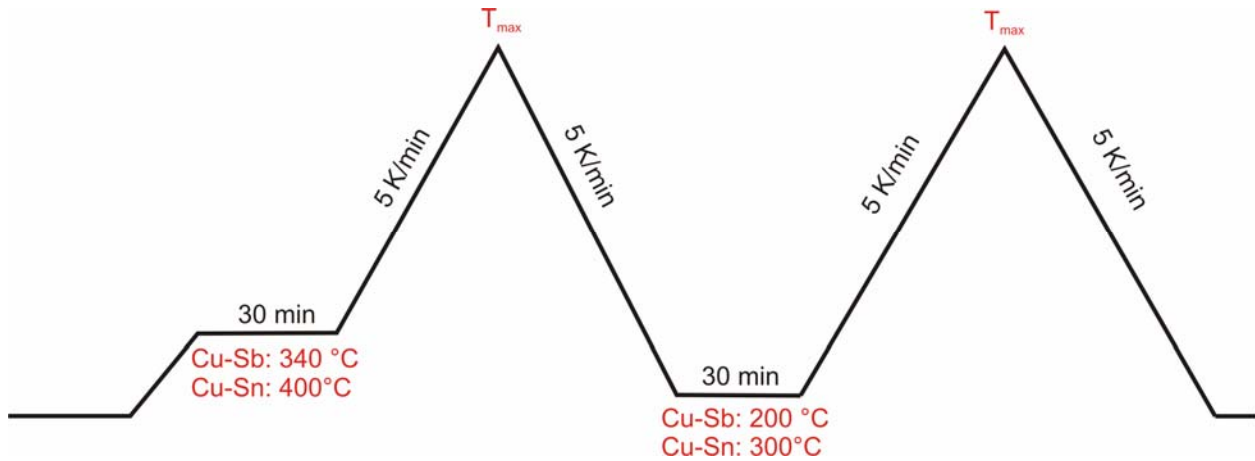


Fig. 36: DTA quartz glass crucible



The heating program (see also Fig. 37) started at room temperature, it was heated as fast as possible until the annealing temperature (Cu-Sn: 400°C; Cu-Sb: 340°C) was reached. There the temperature was kept constant for 30 min. Then the temperature was increased with a slope of 5 K/min, until it reached approximately 50-100°C more than the expected melting temperature (liquidus line). The cooling line was similar (5 K/min). The lowest temperature after cooling was 300°C at Cu-Sn and 200°C at Cu-Sb. Then it was heated and cooled again in the same way.

Fig. 37: Temperature program Netzsch DTA 404S



The diagrams were analysed with the Netzsch-Proteus[®] software. The graphs were transformed into a Signal/°C-diagram and thermal effects treated with the evaluation software Proteus[®] (Onset, Endset, Peak-Maximum, extrapolated Signals).

4.3.2 Differential Thermals Analysis Setaram Setsys Evolution

The TG-DTA Setaram Setsys Evolution is a device for the investigation of thermal effects in open crucibles (Fig. 38). The arrangement also would allow thermogravimetry methods, because the ceramic specimen holder is mounted onto a microbalance (range: 200mg). Crucible material is alumina, tantalum or carbon, for our measurements alumina was used. The sample was a piece of an annealed and quenched alloy (Cu-Sn: 400°C, Cu-Sb: 340°C) and had to be one piece with a flat bottom (~200mg). It was fixed in an alumina crucible at the side of the thermocouple where the temperature was measured, reference material were several small slices of titanium sheet in a second crucible (see Fig. 39).

To prevent oxidation from the air, the analysis chamber had to be evacuated and purged with argon several times. The measurement was done with a constant Ar-gas-flow of 20 ml/min. For our measurements the temperature program was the same as given in Fig. 37, but with a second run with 10 K/min. The maximum temperature of the Cu-Sn-samples was 1000°C, whereas the Cu-Sb samples were tried to be heated only 50-100°C above the estimated liquidus temperature, hence the volatility of antimony at higher temperatures is much higher than that one of tin. The evaluation of the data was done with the Calisto[®] software. The benefit of this software, compared to the Netzsch Proteus[®] software, is the ability of the exact separation of interfering signals with the peak deconvolution tool. Because of the higher sensitivity of the Setaram Setsys Evolution (3-point DTA), compared to the Netzsch DTA 404S, also very small temperature effects could be explored, which couldn't be distinguished from the background noise before.

Fig. 38: DTA Setaram Setsys Evolution [57]

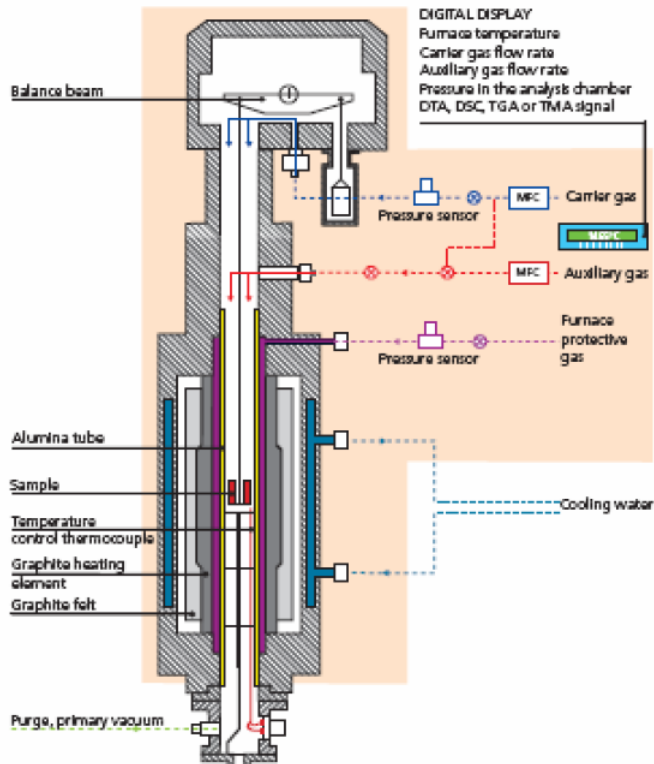


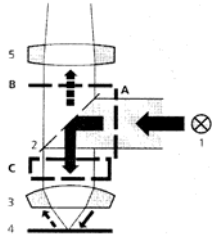
Fig. 39: open DTA furnace with open alumina crucibles (left side: sample; right side: reference Ti)



4.3.3 Reflected light microscope Zeiss Axiotech 100

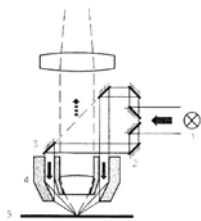
The microscope was used to obtain a rough overview of the phase ratio of the samples and to check the quality of polishing. It has the possibility of 4 different modes of representation:

Fig. 40: Bright field [57] Bright field (Fig. 40):



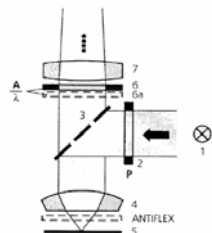
The beam enters the beam separator (2), passes the objective lens (3), is reflected by the sample surface (4) and collected back to the tube lens (5). This is the most common technique, a direct image is obtained. The contrast is due to the surface properties, like roughness, reflectivity and colour. It is sometimes useful for getting a rough idea of the sample.

Fig. 41: Dark field [57] Dark field (Fig. 41):



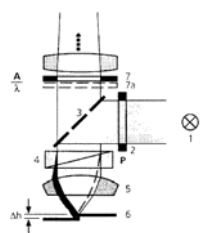
The beam enters a mirror system (2) with a ring mirror (3) and a dark field channel (4). The light is irradiating at low angles. This technique is useful for structured surfaces, cracks, scratches and holes seem bright, while the well-polished surface seems to be dark.

Fig. 42: Polarization [57] Polarization (Fig. 42):



The beam is polarized by a polarizer (2). At the surface of the sample the contrast is modified due to the optical properties of the material. Cubic and high-symmetric phases keep unicolour while rotating the specimen holder, anisotropic lattices (with lower symmetry) change their colour and contrast.

Fig. 43: DIC [57]



Differential interference contrast (Fig. 43):

A birefringent prism splits the beam into two parts. After being reflected by the sample, the beams interfere again and give a view of the heights of different parts of the surface ("altitude map").

4.3.4 EPMA CAMECA SX 100 and ESEM Zeiss Supra 55 VP

The EPMA (electron probe micro analysis) and the ESEM (environmental scanning electron microscope) technologies are non-destructive analysis methods and allow the depiction of the sample surface and the identification of the elementary composition of grains in the polished samples.

The techniques work with an electron beam which can be focused on a certain position at the surface of the sample. The excitation energy of the electron beam is about 5-30 kV depending on the kind of atoms and excited spectral lines (for our measurements there was a current of 15-20kV used). The beam hits the sample surface and produces a range of scattering effects (secondary electrons, backscattered electrons, Auger-electrons, continuous X-rays which are called “Bremsstrahlung”, characteristic X-rays, fluorescent X-rays).

The two species for the visualisation of our samples were the backscattered electrons and the secondary electrons, which can be detected by the BSE (backscattered electrons detector) and the SE (secondary electrons detector). The secondary electrons have lower energy than the backscattered electrons and are scattered in a lower angle from the surface. They provide a good image of the surface, the view is similar to visible light microscopes.

The backscattered electrons have a higher energy level and leave the surface in a steeper angle. According to the averaged atomic number of the observed crystals the obtained image seems to be brighter or darker (it is brighter if Z is high, because the electron density in the atoms is high). Therefore the BSE is very useful to picture a difference of the electron density, which means usually a difference of the composition.

There are two main spectroscopy techniques used for the composition analysis, namely the EDX (energy dispersive spectroscopy) and the WDX (wavelength dispersive spectroscopy).

In the EDX the produced X-rays are counted in energy dependent channels and result in an intensity- vs. energy-spectrum. By calibration with standard substances (e.g. pure metals) and comparison with the measured spectra the atomic composition can be calculated. The advantage is that this works quite fast. Due to the dependency of the measurement to the obtained spectral lines (e.g. Cu: K; Sn, Sb: L) sometimes interference of these lines can occur. This can lead to a systematic error, especially when similar elements should be distinguished.

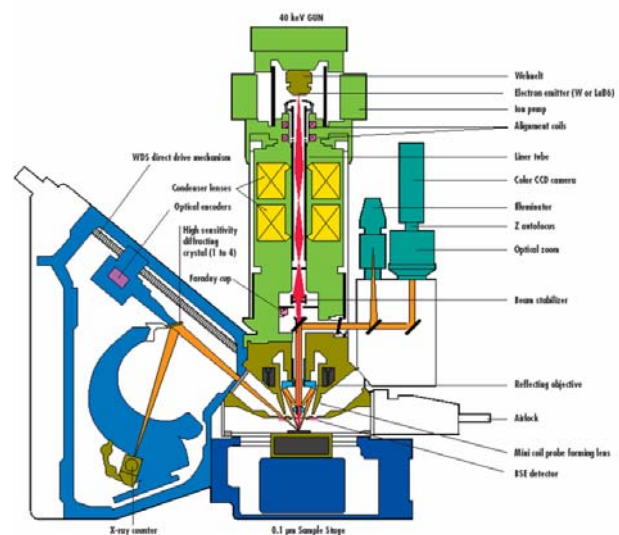
The WDX prevents this problem. Here the X-rays are monochromated by an arrangement of artificial crystals. There are different crystals used for different wavelength ranges. The detection of different wavelengths requires a movement of the crystal and the detector along the focusing circle. This is the only disadvantage, because the wavelength scan requires more time.

The Zeiss Supra 55 VP ESEM (Fig. 44) is only equipped with one crystal, therefore the spectroscopy method was in most cases the EDX. At the EPMA CAMECA SX 100 (Fig. 45) there were 4 crystals available, this allowed to measure 4 elements simultaneously in the WDX mode.

Fig. 44: Zeiss Supra 55 VP ESEM [58]



Fig. 45: CAMECA SX 100 [57]



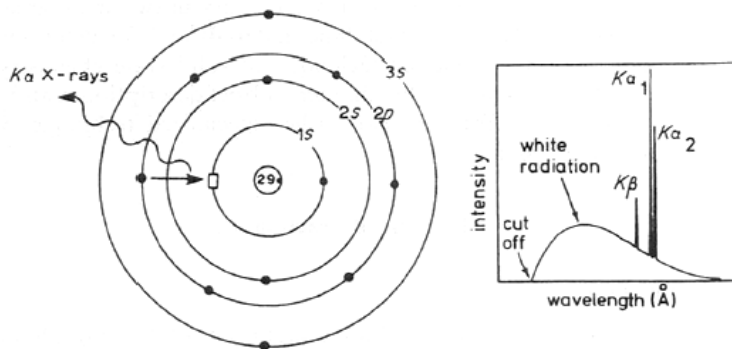
4.3.5 Bruker D8 Powder-X-Ray-Diffractometer

Fig. 46: Bruker D8 diffractometer [57]



The specimen holder with the sample is located exactly in the centre of this circle. When the specimen holder covers an angle of Θ , the detector moves 2Θ (see Fig. 46). This arrangement is contrary to a Θ/Θ -geometry where only the radiation source and the detector move along the goniometer circle, the specimen holder is in the centre of the circle and fixed.

Fig. 47: Origin of Cu-X-ray-radiation [59]

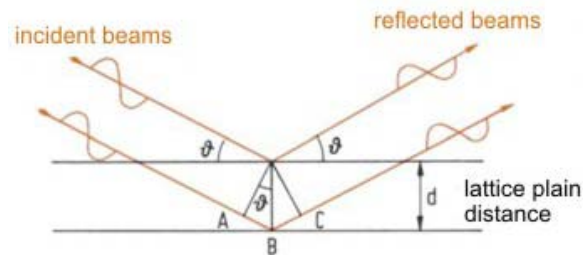


X-ray-radiation was produced by a copper-radiation source at an accelerating voltage of 40 kV and an electron current of 40 mA. The X-ray spectrum consists of white radiation (“Bremsstrahlung”) and the characteristic $K\alpha_1$, $K\alpha_2$ and $K\beta$ radiation peaks, whereas the both $K\alpha$ peaks are the important ones for our investigations (see Fig. 47).

After passing the automatic slit system the X-rays are reflected at the powdered sample, which is fixed with a small amount of vaseline on a rotary silicon monocrystal specimen holder. Rotating the specimen holder is necessary for averaging the grain distribution and providing a steady exposure of the sample from all sides. The device is also equipped with an autosampler, therefore it is also possible to measure up to nine samples sequential.

The “reflection” of the X-rays at the crystal planes accords to the Bragg’s law: $n\lambda = 2d \sin\theta$ (see Fig. 48).

Fig. 48: Scattering of X-rays on crystal plains [60]



$$n\lambda = 2d \sin\theta$$

The diffracted X-ray-radiation is then focused by a slit system. Afterwards it is filtered with a Ni-filter, which only allows the passing of the $K\alpha_1$ and $K\alpha_2$ lines. This beam is finally detected dependent on the reflection angle with a strip detector (Lynxeye), which consists of many parallel arranged silicon strips. The advantage of this detector compared to others is the possibility of a simultaneously counting rate at different diffraction angles and a resulting short measurement time (1h per sample) with a comparably good resolution.

4.3.6 The Rietveld-refinement

The Rietveld-refinement is a mathematical method to describe a measured powder pattern by a theoretical pattern, which is calculated from a variety of parameters (see Fig. 49). The calculated pattern is approached to the measured pattern with the least-square-fit. Important information of the calculated powder pattern is the position of the diffraction lines (dependent on lattice parameters and symmetry) and their intensity (multiplicity, site occupations). A powerful instrument for refining structure data is the Topas3[®] software, provided by Bruker AXS. The refining process was in most cases in that order:

- Main information: Instrumental data, parameters of the measurement
- Generating structure files from expected structure data, obtained from databases, e.g. from Pearson's Handbook of Crystallographic Data for Intermetallic Phases [61]
- Calculating of a theoretical pattern from this structure data and refinement of
 1. scale factor
 2. lattice parameters
 3. crystal size
- sometimes atom positions
- If necessary, changing of the Lorentz-polarisation factor
- Checking for the R_w -value of the refinement (\sim values below 10 are acceptable)
- Checking for the significance of the refined lattice parameters

Fig. 49: Important equations to describe a X-ray-scatter-signal [57]

The diagram illustrates the equations for X-ray scattering signal, with labels for various factors:

- Structure factor:**
$$F_{hkl} = \sum_i f_i \cdot e^{2\pi i(hx_i + ky_i + lz_i)}$$
- Temperature factor:**
$$I_{hkl} = |F_{hkl}|^2 \cdot p \cdot \left(\frac{1 + \cos^2 2\Theta}{\sin^2 \Theta \cos \Theta} \right) \cdot e^{-\frac{2B \sin^2 \Theta}{\lambda^2}}$$
- multiplicity factor of hkl plane set:**
$$\chi^2 = \frac{\sum_i w_i (y_{oi} - y_{ci})^2}{\sum_i w_i y_{oi}}$$
- Lorentz polarization factor:**
$$y_{ci} = y_{bi} + S \cdot \sum_{hkl} |F_{hkl}|^2 \cdot p \cdot \left(\frac{1 + \cos^2 2\Theta_i}{\sin^2 \Theta_i \cos \Theta_i} \right) \cdot e^{-\frac{2B \sin^2 \Theta}{\lambda^2}} \cdot \Phi(2\Theta_i - 2\Theta_{hkl}) \cdot P_{hkl} \cdot A \cdot S_r \cdot E$$

Legend:

- S: Scaling factor (for each phase)
- y_{bi}: Background at i
- P_{hkl}: Factor for preferred orientation
- S_r: Function for surface roughness
- Φ: Profile Function
- A: Absorption function
- E: Extinction factor

Additional labels in the diagram:

- y_{oi}: observed intensity at point i
- y_{ci}: calculated intensity at point
- w_i: weight factor 1/σ(y_{oi})²

4.3.7 High temperature Bruker D8

The arrangement for measuring powder samples at temperatures higher than room temperature consists of a powder diffractometer (Bruker D8, $\theta/2\theta$ -geometry, Cu-radiation, Ni-filter, strip detector) and a heatable specimen holder in an evacuable chamber (see Fig. 50 and Fig. 51). The specimen holder is made of ceramic and can contain an estimated 1mm thick layer of the powdered sample. It can be heated to a certain temperature up to 800°C. Due to the fact that the temperature is measured at the edge of the ceramic crucible and not in the centre of the sample, the temperature in the sample can differ by a few degrees centigrade from the measured temperature.

Another important fact to know about is the gas proofness of the vacuum chamber. The arrangement was originally constructed for investigating minerals, which are nearly inert against oxidation. For this purpose only a veritable vacuum was needed. Because of the too little diameter of the connection to the vacuum pump as well as the geometry of the vacuum chamber, it was difficult to achieve oxygen free conditions. There were several attempts to run the measurement in vacuum or inert gas (He or N₂), but in most case the result was an partial oxidation of the sample. Finally, the use of N₂-gas, an upstream gas purifying cartridge and a piece of Ti-foil in the measuring chamber to gather traces of remaining oxygen, lead to the breakthrough.

Fig. 50: High-temperature vacuum chamber

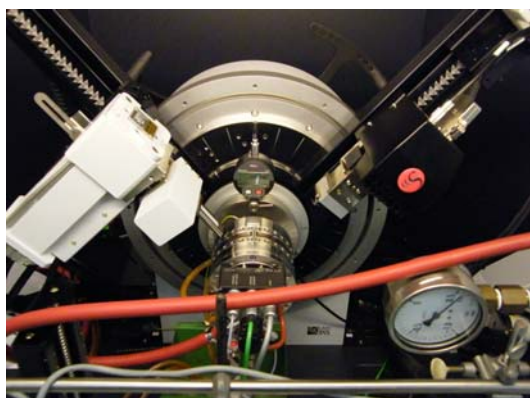


Fig. 51: High-temperature specimen holder



5 Discussion

5.1 Results in the system Cu-Sn

5.1.1 Thermal analysis: DTA

The DTA analysis of the samples at 11, 14, 15, 15.5, 16, 17, 18.5, 21, 24 and 27.5 at% Sn was done with the Netsch DTA 404S, furthermore there were data available at 13, 14, 15, 16, 17, 18, 19 and 20 at% Sn, recorded with the Setaram Setsys Evolution. The measurements with the Setaram DTA had shown a lower background noise and a better resolution of neighbouring peaks. The following results are also listed in Table 17.

The found liquidus temperatures match very well to the data from the literature, although some values (14-17 at% Sn) indicated a liquidus of 20-50°C lower temperature than reported by former authors [29]. Here we found broadened melting peaks which were interpreted as two peaks and took into account in the constructed phase diagram. The peritectic reactions reported at 798°C ((Cu) + L → β) and at 755°C (β + L → γ) were found at 798°C and 758°C. The signal of the latter one interfered with the melting peak, it could only be identified by peak deconvolution (Calisto[®] software).

The eutectoid reaction $\delta \rightarrow (\text{Cu}) + \varepsilon$ was estimated at 350°C by the literature [29]. This effect was also found in the second heating loop of the samples with 11, 15.5, 18.5, 21 and 24 with the Netzsch DTA 404S, assigned to the fact that the reference material nickel has a Curie temperature in this region we only can estimate the real value from the literature. The measurements with the Setaram Setsys Evolution (reference: Ti) showed some signals in this region which could origin from the reaction at 350°C. There also were serial signals which arose from the stabilisation of the baseline after the start of the next heating loop at 300°C, but it was not possible to distinguish the expected peak at 350°C from these ones, thus we couldn't identify the reaction temperature significantly.

The described eutectoid reaction at 520°C ($\gamma \rightarrow (\text{Cu}) + \delta$) [29] was also found in this research very clearly, a temperature correction of 2°C to the lower temperature at 518°C would be advisable, referring on the data recorded by the Setaram Setsys Evolution.

Further invariant reactions were verified at 649°C (640°C: $\gamma \rightarrow \varepsilon + \text{L}$ [29]), 641°C (640°C: $\gamma + \varepsilon \rightarrow \zeta$ [29]), 603°C (590°C: $\gamma + \zeta \rightarrow \delta$ [29]), 589°C (582°C: $\zeta \rightarrow \delta + \varepsilon$ [29]) and 408°C (415°C: $\varepsilon + \text{L} \rightarrow \eta$ [29]).

In the (Cu)- β , γ -two-phase field some signals occurred, which would lead us to the eutectoid reaction which is described by the literature (586°C : $\beta \rightarrow (\text{Cu}) + \gamma$ [29]). The cited temperature differs a bit from our results. We also assume that there is no “real” invariant reaction at this temperature, because the obtained temperature signal is very low, compared to other invariant reactions (e.g. the eutectoid reaction at $\sim 518^{\circ}\text{C}$). We think that these signals origin from a degenerated invariant reaction and indicate the presence of a second-order-transition between β and γ . Another evidence for this theory is the circumstance that the thermal effect becomes smaller towards samples of lower Sn concentrations (see Fig. 52). We estimate this degenerated invariant reaction at 566°C .

At the Sn-rich side of the γ -field it seems that there is a higher solubility of Sn in γ than described by Saunders & Miodownik [29], this would lead to a convexity of the γ / γ - ζ - and the γ / γ - δ -phase lines and a shift about 2-3 at% Sn to the Sn-rich side.

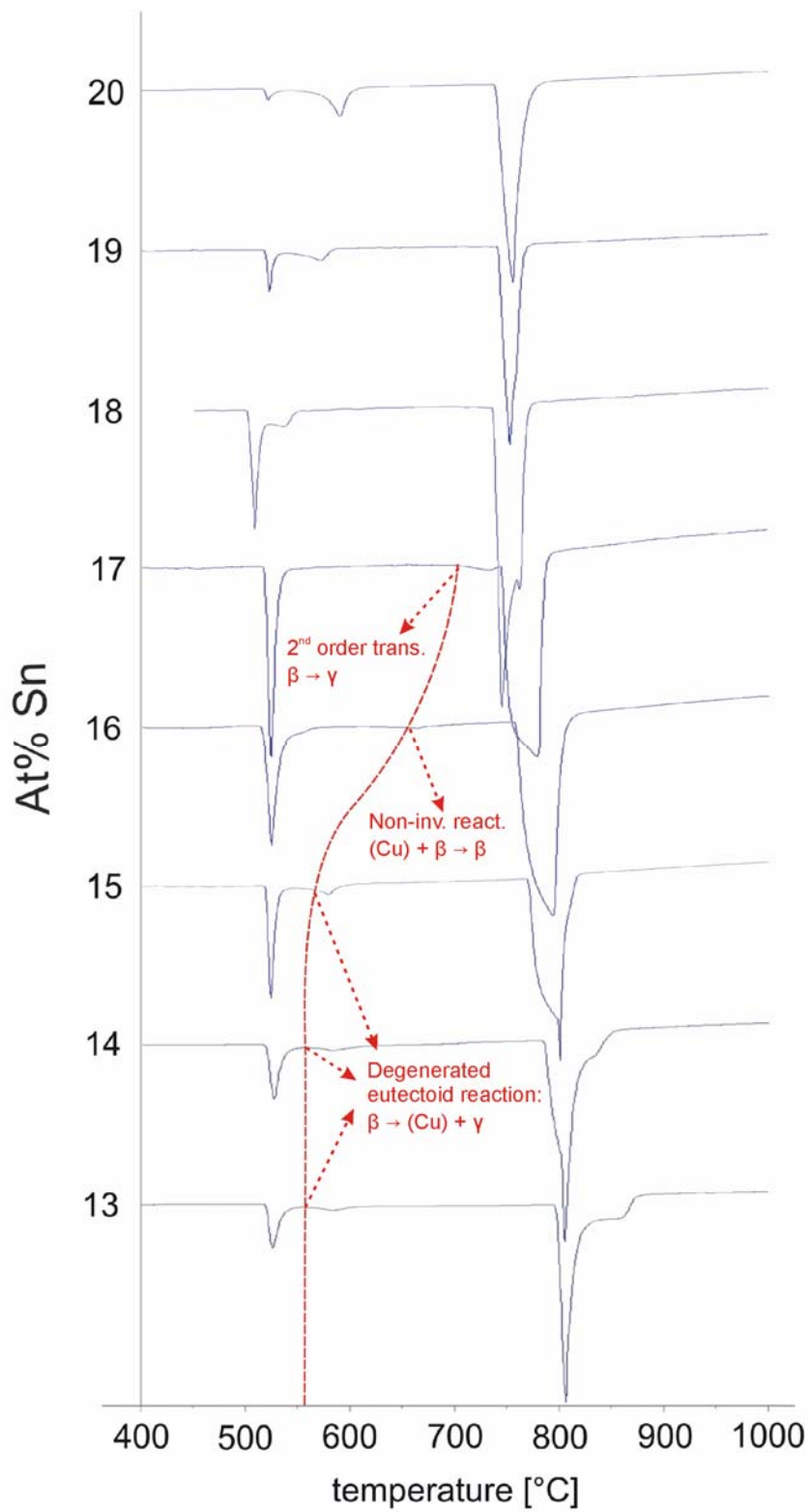
At the Cu-rich side of the estimated γ -field there could be found two small signals at 641°C (16 at% Sn) and at 685°C (17 at% Sn). This could be the borders of the β - γ -two-phase field. Our interpretation of these signals is the presence of a $\beta \rightarrow \gamma$ –second-order transition, which would be more evident because there was only one well-defined signal found per sample. If there would be a first order transition and therefore an existing β - γ -two-phase field, we would expect two independent signals which would be formed if a sample was scanned from low temperature to the melting point. According to the HTPXRD results, we assign the effect at $641^{\circ}\text{C} / 16 \text{ at\% Sn}$ to the $(\text{Cu}) + \beta / \beta$ –line, whereas the other effect at $685^{\circ}\text{C} / 17 \text{ at\% Sn}$ could belong to the $\beta \rightarrow \gamma$ –second-order transition boundary (see Fig. 52). To summarize the reactions belonging to the $\beta \rightarrow \gamma$ –second-order transition, we can assume that the degenerated invariant reaction at 566°C (13-15 at% Sn) disappears at higher Sn contents. Samples at 16 and 17 at% Sn showed effects at higher temperatures, which can be interpreted as the non-invariant reaction between the (Cu)- β -two-phase-field and the β -phase (16 at% Sn / 641°C) as well as the second-order-transition ($\beta \rightarrow \gamma$) (17 at% Sn / 684°C); see also Fig. 52.

In the β -liquidus field there were several signals occurring. We could examine the reaction at 758°C, but between 14 and 18 at% Sn a broadening of the peaks due to interferences with the liquidus line was observable. We assume that the first broadening (13-14 at% Sn) arises from the interference of the β / β -liquidus (= solidus) line with the liquidus line. The second and most interesting interference is between 15 and 18 at% Sn, we suggest that here also the liquidus-line interferes with the γ -solidus line, and if existing, also with the peritectic reaction at 758°C ($\beta + L \rightarrow \gamma$). If this reaction would exist, then this proves the presence of the often mentioned β - γ -two-phase field [29]. According to our HTPXRD results, we can estimate that this temperature doesn't show the peritectic reaction, because we didn't find beta and gamma in any sample in equilibrium. Furthermore we can consider that this temperature is the analogue to the reaction at 566°C, and is a degenerated invariant reaction, starting at the $\beta \rightarrow \gamma$ –second-order transition boundary.

Table 17: Comparison of reactions and temperatures between literature and this work (Cu-Sn)

Invariant reactions	Temperature °C [29]	Temperature °C, this work	Comments
$(\text{Cu}) + L \rightarrow \beta$	798	798	
$\beta + L \rightarrow \gamma$	755	758	Interference with melting peak, Second order transition
$\varepsilon \rightarrow \gamma$	676	-	Not investigated
$\gamma + \varepsilon \rightarrow \zeta$	640	641	
$\gamma \rightarrow \varepsilon + L$	640	649	
$\gamma + \zeta \rightarrow \delta$	590	603	
$\beta \rightarrow (\text{Cu}) + \gamma$	586	566	Second order transition
$\zeta \rightarrow \delta + \varepsilon$	582	589	
$\gamma \rightarrow (\text{Cu}) + \delta$	520	518	
$\varepsilon + L \rightarrow \eta$	415	408	
$\delta \rightarrow (\text{Cu}) + \varepsilon$	350	350	
$L \rightarrow \eta + (\text{Sn})$	227	-	Not investigated

Fig. 52: DTA curves 13-20 at % Sn



5.1.2 PXRD at room temperature

Six samples with the compositions 11, 15.5, 18.5, 21, 24 and 27.5 at% Sn were annealed at 400°C and at 700°C, quenched in water, powdered and analyzed with the powder X-ray diffraction method. A summary of found phases and lattice parameters is given in Table 18.

Table 18: Crystal structures and lattice parameters of quenched Cu-Sn-samples

No.	Nominal Composition (at%)	Heat Treatment (°C)	Phase Analysis		
			Phase	Structure Type	Lattice Param. (Å)
CS_F_01	Cu ₈₉ Sn ₁₁	400°C, 14d	α = (Cu) δ = Cu ₄₁ Sn ₁₁ ζ = Cu ₁₀ Sn ₃	Fm-3m F-43m P6 ₃	a = 3.68902(1) a = 17.9516(3) a = 7.3304(2) c = 7.8539(3)
CS_F_02	Cu _{84.5} Sn _{15.5}	400°C, 14d	α = (Cu) δ = Cu ₄₁ Sn ₁₁ ζ = Cu ₁₀ Sn ₃	Fm-3m F-43m P6 ₃	a = 3.68981(2) a = 17.9580(2) a = 7.3307(1) c = 7.8632(1)
CS_F_03	Cu _{81.5} Sn _{18.5}	400°C, 14d	α = (Cu) δ = Cu ₄₁ Sn ₁₁	Fm-3m F-43m	a = 3.6847(2) a = 17.9577(2)
CS_F_04	Cu ₇₉ Sn ₂₁	400°C, 14d	δ = Cu ₄₁ Sn ₁₁ ϵ = Cu ₃ Sn	F-43m Cmcm	a = 17.9579(1) a = 5.497(1) b = 47.82(1) c = 4.3288(5)
CS_F_05	Cu ₇₆ Sn ₂₄	400°C, 14d	δ = Cu ₄₁ Sn ₁₁ ϵ = Cu ₃ Sn	F-43m Cmcm	a = 17.9569(8) a = 5.5192(2) b = 47.573(2) c = 4.3294(1)
CS_F_06	Cu _{72.5} Sn _{27.5}	400°C, 14d	ϵ = Cu ₃ Sn η = Cu ₆ Sn ₅	Cmcm P6 ₃ /mmc	a = 5.5277(7) b = 47.681(2) c = 4.3291(1) a = 4.2199(3) c = 5.1009(7)
CS_F_01	Cu ₈₉ Sn ₁₁	700°C, 14d	α = (Cu) δ = Cu ₄₁ Sn ₁₁	Fm-3m F-43m	a = 3.7179(9) a = 17.9526(6)
CS_F_02	Cu _{84.5} Sn _{15.5}	700°C, 14d	α = (Cu) δ = Cu ₄₁ Sn ₁₁	Fm-3m F-43m	a = 3.7020(9) a = 17.9447(6)
CS_F_03	Cu _{81.5} Sn _{18.5}	700°C, 14d	δ = Cu ₄₁ Sn ₁₁	F-43m	a = 17.9469(2)
CS_F_04	Cu ₇₉ Sn ₂₁	700°C, 14d	δ = Cu ₄₁ Sn ₁₁	F-43m	a = 17.97531(9)
CS_F_05	Cu ₇₆ Sn ₂₄	700°C, 14d	ζ = Cu ₁₀ Sn ₃	P6 ₃	a = 7.3306(1) c = 7.8650(2)
CS_F_06	Cu _{72.5} Sn _{27.5}	700°C, 14d	ϵ = Cu ₃ Sn ζ = Cu ₁₀ Sn ₃	Cmcm P6 ₃	a = 5.5124(4) b = 47.453(4) c = 4.3384(2) a = 7.3258(1) c = 7.8662(2)

All phases, except the β - and the γ -phase, were found in the quenched samples. These two phases are high temperature phases, which can not be quenched, but undergo bulk transformation to the respective low temperature phases or transform to metastable phases [21, 22]. This is the reason why in some samples we could find more than two phases, contrary to the Gibbs' phase rule in binary systems. As a conclusion of this fact we decided to perform high temperature powder X-ray diffraction measurements.

5.1.3 HTPXRD

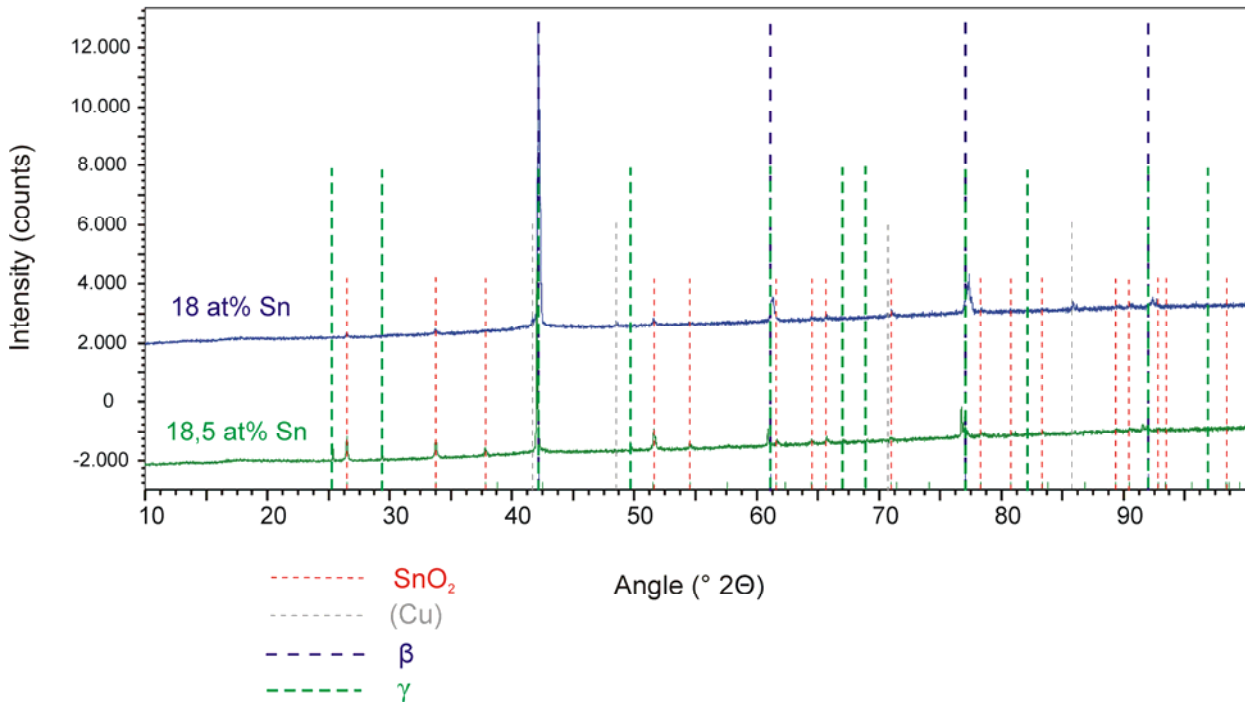
To investigate the phase relations of the high-temperature phases β and γ , the HTPXRD method was employed. The arrangement was similar to the room temperature PXRD, the difference to the former method was in the increased temperature, the inert gas and the special specimen holder. There were several runs started to find the best method in applying the inert gas atmosphere to the Cu-Sn samples. The goal was to prevent the oxidation of the alloys to SnO_2 (tP6) and CuO , the former was already formed at very low O_2 concentrations. Several assessments with dynamic vacuum, dynamic He-flow (He-gas 99.99999 % pure) and steady He-atmosphere, combined with Ti-foil as an oxygen getter at high temperatures and finally, the use of an upstream gas purifying cartridge for the Helium failed, there was still some SnO_2 detectable in the diffractograms. It was not really clear until the end of the measurements, why we had these problems with the oxidation of our powders. We assume that the geometry of the vacuum chamber and the arrangement of gas inlet and outlet were not adequate for the use of helium as an inert gas. The low density of helium would possibly lead to a low inert gas concentration at the bottom of the chamber where the sample was placed. Another reason could be a leak somewhere at an intersection of two pipes, this theory was disproved because a vacuum applied once was stable over hours. The most plausible explanation for the oxidation problem would be a high impurity of oxygen in the used helium. Nevertheless, the breakthrough came by using N_2 -gas (99.99999 % pure), a staged purging and an upstream gas purifying cartridge. At first the chamber was evacuated twice for 1 hour each and then flooded with N_2 -gas until 0.5 bar. After increasing the temperature to 100°C , once evacuating and flooding to 1.2-1.6 bar, the measurement could be started. Additionally, a piece of Ti-foil was kept in the vacuum chamber for capturing the remaining traces of oxygen.

Two different temperature programs were used for the measurements. The first program was a screening of samples CS_F_01-06 (11-27.5 at% Sn, previously annealed at 400°C); see also Table 14 and Fig. 55. The temperature was increased in intervals of 25°C and kept steady for one hour to ensure thermodynamic equilibrium. Afterwards the diffractogram was recorded. Such a program was typically started at 400°C and stopped at a temperature below the melting temperature. This should provide an overview of sample relations depending on temperature. In the second step an isothermal measurement was employed. The sample was heated up to a certain temperature (e.g. 700°C) and then kept steady for 2.5 h. In this time interval the measurement took place. Usually the measurement was repeated 5 more times to check if any further reactions would occur and again to assure the thermodynamic equilibrium. The screening method provided data which were mainly consistent with the literature [29], apart from differences in the formation temperatures of some phases, which could arise from the incomplete adjustment of the thermodynamic equilibrium and the error of the measurement due to the temperature gradient in the ceramic specimen holder.

With isothermal measurements at 700°C it was tried to prove the existence of the pure β , pure γ and the pretended connecting β - γ -two-phase field. Although there were traces of SnO₂ occurring after some time and we theoretically had a ternary system Cu-Sn-O, the obtained results can be considered as valid. In the range of 15-18.0 at% Sn the pure β -phase was found, with accompanying traces of SnO₂ and (Cu)-phase, which were formed during the decrease of tin that formed the oxide. At 18.5 at% a few more peaks occurred, complying with the former peaks of the β -phase. The refinement with Topas3[®] had shown clearly that these additional peaks originated from the γ -phase, which is an ordered superstructure of the beta-phase with the doubled lattice parameter in each axis (see Fig. 53).

We also tried to fit the diffractograms with the bcc-B2-structure (CsCl-type), reported by Liu in 2004 [31] to be located between the bcc-A2-structure (W-type) and the bcc-D0₃-structure (BiF₃-type). According to Liu's phase diagram version (see also Fig. 21), the B2-structure should be present in the samples with 17, 18, 18.5 and 20 at% Sn at 700°C, as well as in the sample with 18.5 at% Sn at 725°C, but there was only either the β -phase (is a synonym for the bcc-A2-structure) or the γ -phase (is a synonym for the bcc-D0₃-structure), but never the bcc-B2-structure detectable. So we couldn't confirm Liu's suggestion of an existing bcc-B2-phase (CsCl-type).

Fig. 53: Comparison of diffractograms at 18 & 18.5 at% Sn, 700°C

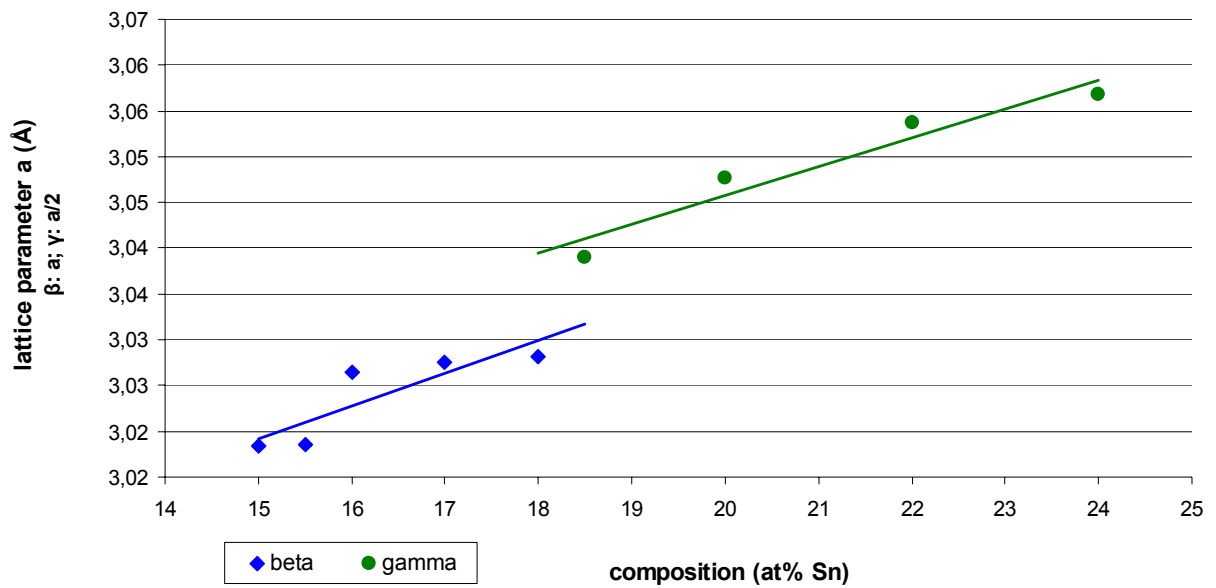


If we respect the resolution of this measurement to be 0.5 at% Sn, we can conclude that the crystal structure changed suddenly from beta to gamma.

Theoretically it would be possible to refine the powder pattern at 18.5 at% Sn with the gamma and the beta structure together, because gamma includes the peaks of the beta diffraction pattern. To evidence the hypothesis that beta and gamma do not exist together in a two-phase-field, the lattice parameters of the β - and the γ -phase were plotted in a diagram as a function of the composition. The lattice parameter of gamma was halved to allow a direct comparison. The plot shows an increase of the lattice parameter with increasing Sn content, because the larger Sn atoms need for both phases more space in the cubic cell than the Cu atoms, and therefore the unit cell has to be widened. We estimate this behaviour with increasing Sn content as linear, this is shown by a linear best-fit line. The two best-fit lines for beta and gamma show a significant step in the lattice parameter between 18 and 18.5 at% Sn (see Fig. 54). Thus we can exclude a complete interference of the β - and γ -XRD-pattern in one sample. This observation differs to the results of Knödler [22], who reported a linear increase of the lattice parameter at compositions between 14 and estimated 20 at% Sn, without the existence of any step in the graph (see Fig. 19). He also found that the significant γ -lines in the diffractogram appeared slightly between 15 and 17 at% Sn and became clear at >17 % Sn.

This also was not the case in our investigations. We could show that the gamma diffraction lines appeared suddenly at 18.5 at% Sn (see Fig. 53). The different results compared to Knödler's work in the early 1960's may be due to the nowadays available modern diffraction technique and the availability of computers to manage sophisticated mathematical procedures, which support an accurate and fast analysis.

Fig. 54: Lattice parameter vs. composition at 700°C



The fact, that there is neither a two-phase sample which contains beta and gamma, nor a continuous change of the crystal structure, leads us to the conclusion that the phase transition between the beta and gamma phase is a special case of a fast, non-diffusion-controlled second order transition. Thus we have omitted the β - γ -two-phase-field in our phase diagram version (see Fig. 56).

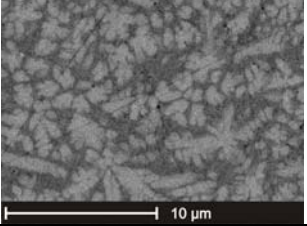
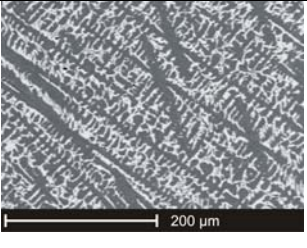
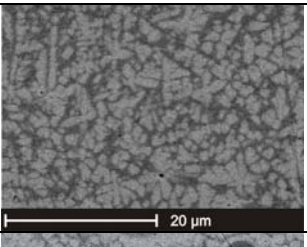
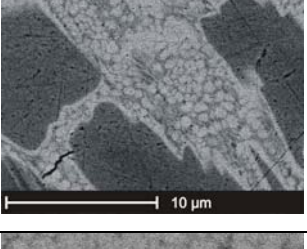
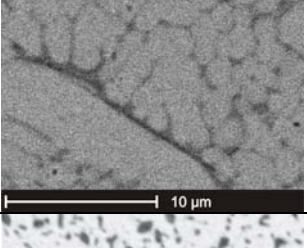
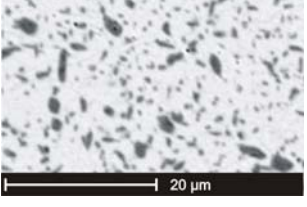
5.1.4 ESEM / EPMA

With the ESEM and the EPMA method the composition of the phases of quenched samples at the annealing temperature of 400 and 700°C was examined (see Table 19 and Table 20). The samples were embedded, polished and measured with EDX (ESEM) and WDX (EPMA) mode. For the calibration of the Cu-measurement the K-line was used, for Sn we took the L-line. The acceleration voltage of the beam was 15-20 kV, depending on the size of the examined grains (smaller grains → lower voltage → less beam diameter and depth of indentation).

The homogeneity ranges of the phases in the samples quenched from 400°C were nearly the same as described in the phase diagram of Saunders and Miodownik [15]. The (Cu)-phase, which formed characteristic dendritic crystals of copper, had a solubility range of Sn in (Cu) of 7.7 at%. The δ -phase existed at 400°C in a small concentration range at estimated 20.8 – 21.1 at% Sn. Similar was the ϵ -phase, which was a line-shaped phase too, with a small concentration range between 25.3 and 25.8 at% Sn. Finally also the easily detectable η phase was found, it appeared very bright in the ESEM due to the high Sn content and had its phase boundary at the Cu-rich side at 44.5 at% Sn.

The interpretation of the samples quenched from 700°C was a little bit more complicated. Theoretically, only the β - and γ -phase should have been occurred at this temperature, but they could not be quenched to room temperature and had therefore formed the previously mentioned phases which were stable at lower temperatures. The δ - and ϵ -phase could be found in the ESEM, the homogeneity range was the same as with the samples quenched from 400°C. Remarkable is also the presence of the ζ -phase in samples with 21-27.5 at% Sn. The homogeneity range of the ζ -phase was between 22.2 and 22.7 at% Sn, which accords roughly to the literature data in a temperature range of 582-640°C [15]. According to the X-ray diffraction results of the quenched sample $\text{Cu}_{76}\text{Sn}_{24}$ (contained pure ζ -phase after quenching from 700°C) we could conclude that the solubility of the ζ -phase at the Sn-rich side was extended to 24 at% Sn. However, we did not consider this result, because this is not an equilibrium sample. For further conclusions this sample has to be annealed at temperatures below the existence of the γ -phase.

Table 19: ESEM / EPMA results of Cu-Sn phase compositions

Sample composition	Ann.-temp.	Phase 1 (dark)			Phase 2 (bright)			SEM image
			at% Cu	at% Sn		at% Cu	at% Sn	
Cu ₈₉ Sn ₁₁	700°C	(Cu)	not resolvable		δ _{Cu}	81.3	18.7	
	400°C	(Cu)	92.6	7.4	δ _{Cu}	79.9	20.1	
Cu _{84.5} Sn _{15.5}	700°C	(Cu)	not resolvable		δ _{Cu}	79.6	20.4	
	400°C	(Cu)	92.2	7.8	δ _{Cu}	80.1	19.9	
Cu _{81.5} Sn _{18.5}	700°C	(Cu)	not resolvable		δ _{Cu}	78.7	21.3	
	400°C	(Cu)	91.8	8.2	δ _{Cu}	79.1	20.9	

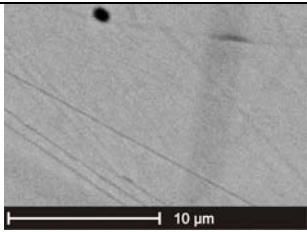
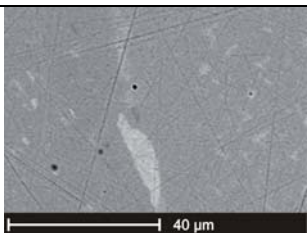
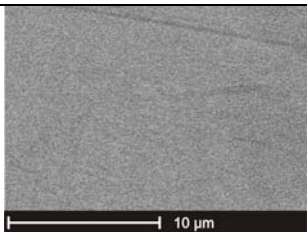
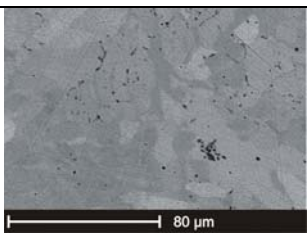
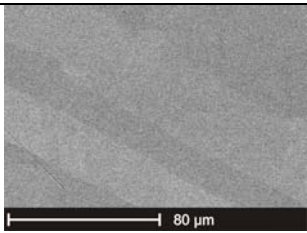
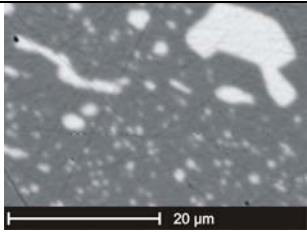
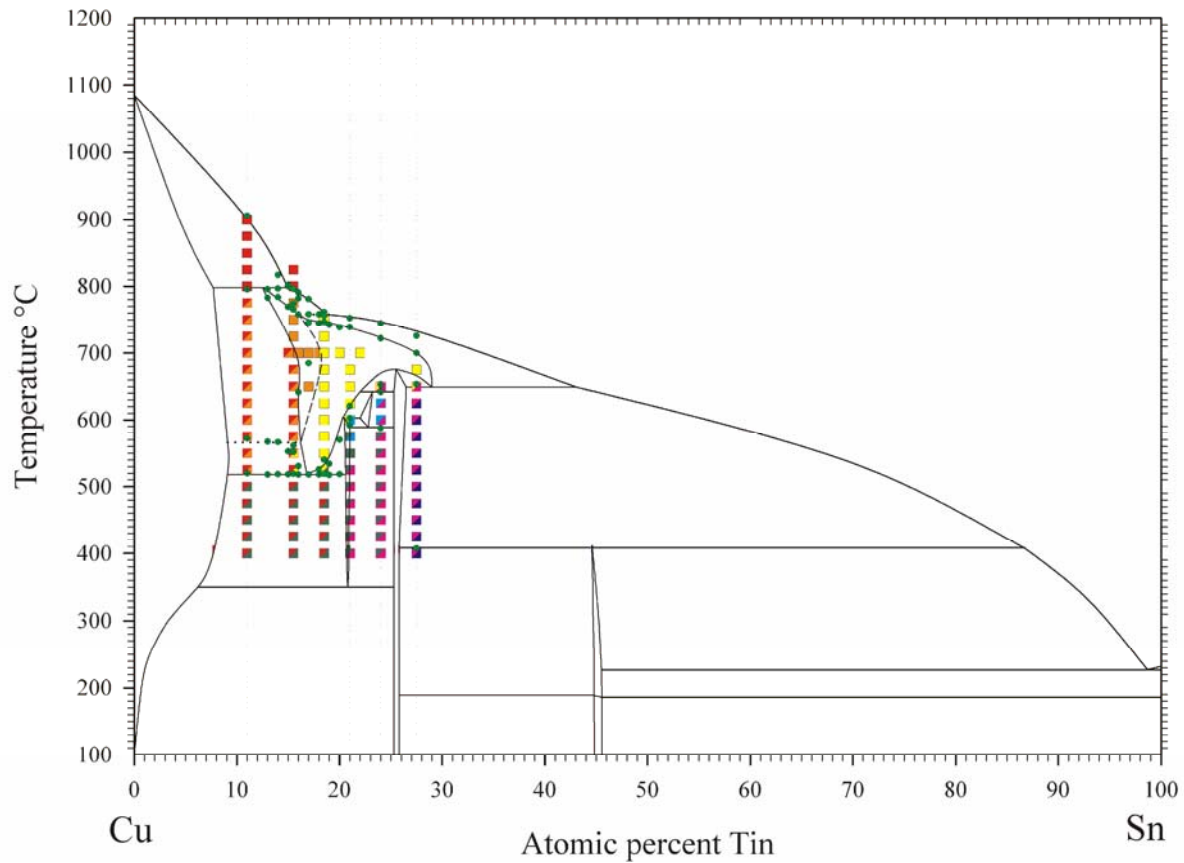
$\text{Cu}_{79}\text{Sn}_{21}$	700°C	δ_{Sn}	78.3	21.7	ζ_{Cu}	77.8	22.2	
	400°C	δ_{Sn}	79.0	21.0	ϵ_{Cu}	75.1	24.9	
$\text{Cu}_{76}\text{Sn}_{24}$	700°C	ζ_{Cu}	77.3	22.7	No second phase observable			
	400°C	δ_{Sn}	79.0	21.0	ϵ_{Cu}	75.0	25.0	
$\text{Cu}_{72.5}\text{Sn}_{27.5}$	700°C	ζ_{Sn}	77.4	22.7	ϵ_{Cu}	74.7	25.3	
	400°C	ϵ_{Sn}	74.3	25.7	η_{Cu}	56.0	44.0	

Table 20: Summary of ESEM / EPMA results

Phase	400°C → quenched			700°C → quenched	
	at% Cu	at% Sn		at% Cu	at% Sn
(Cu)	92.3 (92.0)	7.7 (8.0)			
δ_{Cu}	79.2 (79.8)	20.8 (20.2)		79.3 (n)	20.7 (n)
δ_{Sn}	79.0 (79.2)	21.0 (20.8)		78.3 (n)	21.7 (n)
ζ_{Cu}				77.8 (n)	22.2 (n)
ζ_{Sn}				77.3 (n)	22.7 (n)
ϵ_{Cu}	74.7 (75.5)	25.3 (24.5)		74.5 (n)	25.5 (n)
ϵ_{Sn}	74.2 (74.7)	25.8 (25.3)			
η_{Cu}	55.5 (56.5)	44.5 (43.5)			
<p>X_{Cu}...concentration limit of phase X at Cu-rich side X_{Sn}...concentration limit of phase X at Sn-rich side Values in brackets: Literature [15] (n)...phase not stable at 700°C [15]</p>					

5.1.5 Phase diagram Cu-Sn

Fig. 55: Developed Cu-Sn phase diagram, including data points



HT-PXRD	ESEM/EPMA	thermal analysis
■ alpha	■ alpha	• DTA
■ alpha beta	■ delta	
■ alpha gamma	■ epsilon	
■ alpha delta	■ eta	
■ beta		
■ gamma		
■ gamma delta		
■ gamma epsilon		
■ gamma zeta		
■ delta		
■ delta epsilon		
■ delta zeta		
■ epsilon zeta		
■ epsilon eta		

Fig. 56: Developed Cu-Sn phase diagram with temperatures and compositions

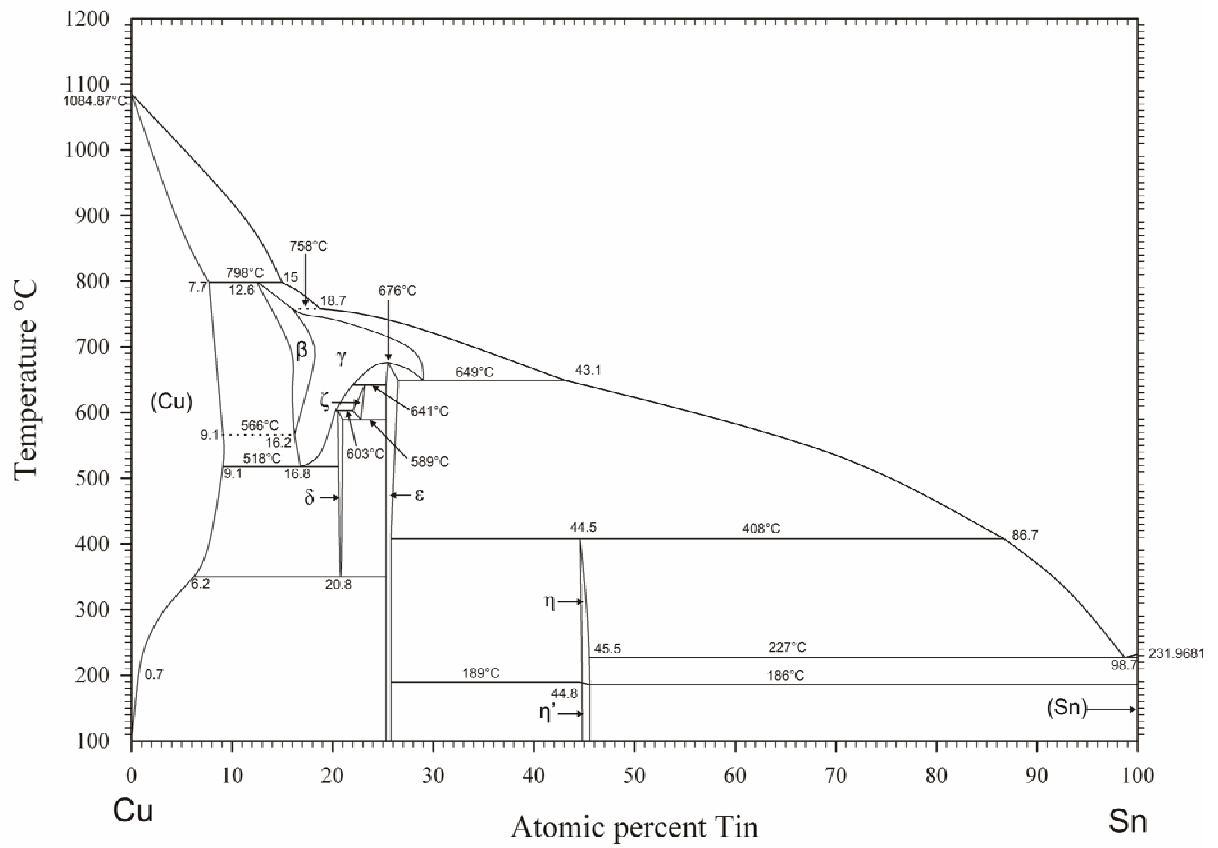


Table 21: Comparison temperature-invariant reactions in the Cu-Sn-system this work and literature [15]

Reaction	Composition of equilibrium phases (at% Sn)			Temp. (°C)	Reaction type
$(\text{Cu}) + \text{L} \rightarrow \beta$	7.7 [#]	12.6 (13.1)	15.0 (15.5)	798 (798)	Peritectic
$\beta + \text{L} \rightarrow \gamma$	16.0 (15.8)	16.5 [#]	18.7 (19.1)	758 (755)	Degenerated
$\varepsilon \rightarrow \gamma$	25.5 [#]	25.5 [#]	25.5 [#]	676 [#]	Congruent
$\gamma + \varepsilon \rightarrow \zeta$	22.0 (21.8)	23.2 (22.5)	25.3 (24.5)	642 (640)	Peritectoid
$\gamma \rightarrow \varepsilon + \text{L}$	26.5 (25.9)	29.0 (27.9)	43.1 [#]	649 (640)	Metatectic
$\gamma + \zeta \rightarrow \delta$	20.3 (19.8)	20.5 (20.3)	22.0 (20.9)	603 (590)	Peritectoid
$\beta \rightarrow (\text{Cu}) + \gamma$	9.1 [#]	14.9 [#]	16.2 (15.4)	566 (586)	Degenerated
$\zeta \rightarrow \delta + \varepsilon$	21.0 (20.8)	22.8 (21.7)	25.3 (24.5)	589 (582)	Eutectoid
$\gamma \rightarrow (\text{Cu}) + \delta$	9.1 [#]	16.8 (16.5)	20.6 (20.4)	518 (520)	Eutectoid
$\varepsilon + \text{L} \rightarrow \eta$	25.8 (24.9)	44.5 (43.5)	86.7 [#]	408 (415)	Peritectic
$\delta \rightarrow (\text{Cu}) + \varepsilon$	6.2 (6.2)	20.8 (20.5)	25.3 (24.5)	350 [#]	Eutectoid
$\text{L} \rightarrow \eta + (\text{Sn})$	45.5 [#]	98.7 [#]	>99.9 [#]	227 [#]	Eutectic

[#] value adopted from literature [15]

(value)...literature value [15]

5.2 Results in the system Cu-Sb

5.2.1 Thermal analysis: DTA

For the thermal analysis two different DTA devices, the Netzsch DTA 404S and the Setaram Setsys Evolution, were employed. The measurements with the first one were done in closed crucibles (quartz glass, reference was a nickel bead), whereas the Setaram worked with open crucibles in an inert gas atmosphere (Alox-crucibles, reference: Slices of titanium sheet). The samples were annealed for 4 weeks at 340°C, quenched in water and measured after this treatment. The temperature program included two heating and cooling loops, starting from 340°C and ending 50-100°C above the estimated liquidus curve. The temperature increase was 5 K/min at both devices. With the Setaram arrangement we also tried to measure each sample a second time with 10 K/min, immediately after the first two heating-cooling loops the same program was run with the slope of 10 K/min. Our idea was to find some effects with small amplitudes, if we heated the sample a little bit faster. The analysis of the obtained diagrams was done with the Netzsch Proteus[®] software in the case of the Netzsch measurements, for the Setaram data we used the Calisto[®] software. The main advantage of the last-mentioned software was the possibility of a peak deconvolution, which enabled us to calculate the onsets of interfering peaks. All the results are summarized in Table 22.

The maximum of the melting peaks of the samples between 10 and 40 at% Sb resulted in a liquidus curve, which was consistent with the literature [43]. The solidus curve of the β -phase, which could be described by DTA measurements of three samples between 21 and 28 at% Sb, was as well in agreement with the literature [43]. For the eutectic reaction located at 645°C ($L \rightarrow (Cu) + \beta$) the eutectic point could be estimated at 17.7 at% Sb, similar to the literature value at 19 at% Sb [43]. At concentrations of 10 and 17.5 at% Sb some discrepancies occurred at temperatures below 645°C. The main effect in our measurements was observable in both samples at a temperature of 467°C. We relate this effect to the reaction $(Cu) + \beta \rightarrow \gamma$, which is described by the literature [43] to be located at 488°C.

We also found effects at 480-485°C in the sample with 10 at% Sb, but only in the Setaram DTA, whereas we found it in the sample with 17.5 at% Sb only with the Netzsch DTA 404S. We don't want to deny the existence of this effect at 480-485°C, but it was not reproducible and was therefore not considered as a reliable reaction temperature. This decision can thus be justified with the missing reproducibility, the small size of this effect compared to the signal at 467°C, and finally the obtained results of the X-ray diffraction, which is weighted most and will be discussed in the chapter 5.2.2. Furthermore, we didn't find the eutectoid reaction at 400°C ($\gamma \rightarrow (\text{Cu}) + \delta$), but in the samples with 10 and 17.5 at% Sb we found a signal at 440-441 °C. This effect occurred in the sample with 10 at% Sb only at the second, third and fourth heating loop, but not at the first one. Therefore we think that, if this sample was in equilibrium after quenching, this indication is negligible. In the sample with 17.5 at% Sb we found this temperature at the first heating too. If we additionally consider the X-ray diffraction results and the rules for the construction of a binary phase diagram, our assumption is that this sample was not really in a thermodynamic equilibrium before the first measurement. Thus we ignored the signals at 440-441 °C and reference to the literature [43], which locates the reaction at 400°C.

If we further discuss the samples with 17.5 and 21 at% Sb, we see that there was a reaction at estimated 455°C. We suggest that this temperature is attended by the peritectoid reaction " $\beta + \gamma \rightarrow \delta$ ", which is described by the literature [43] to occur at 462°C.

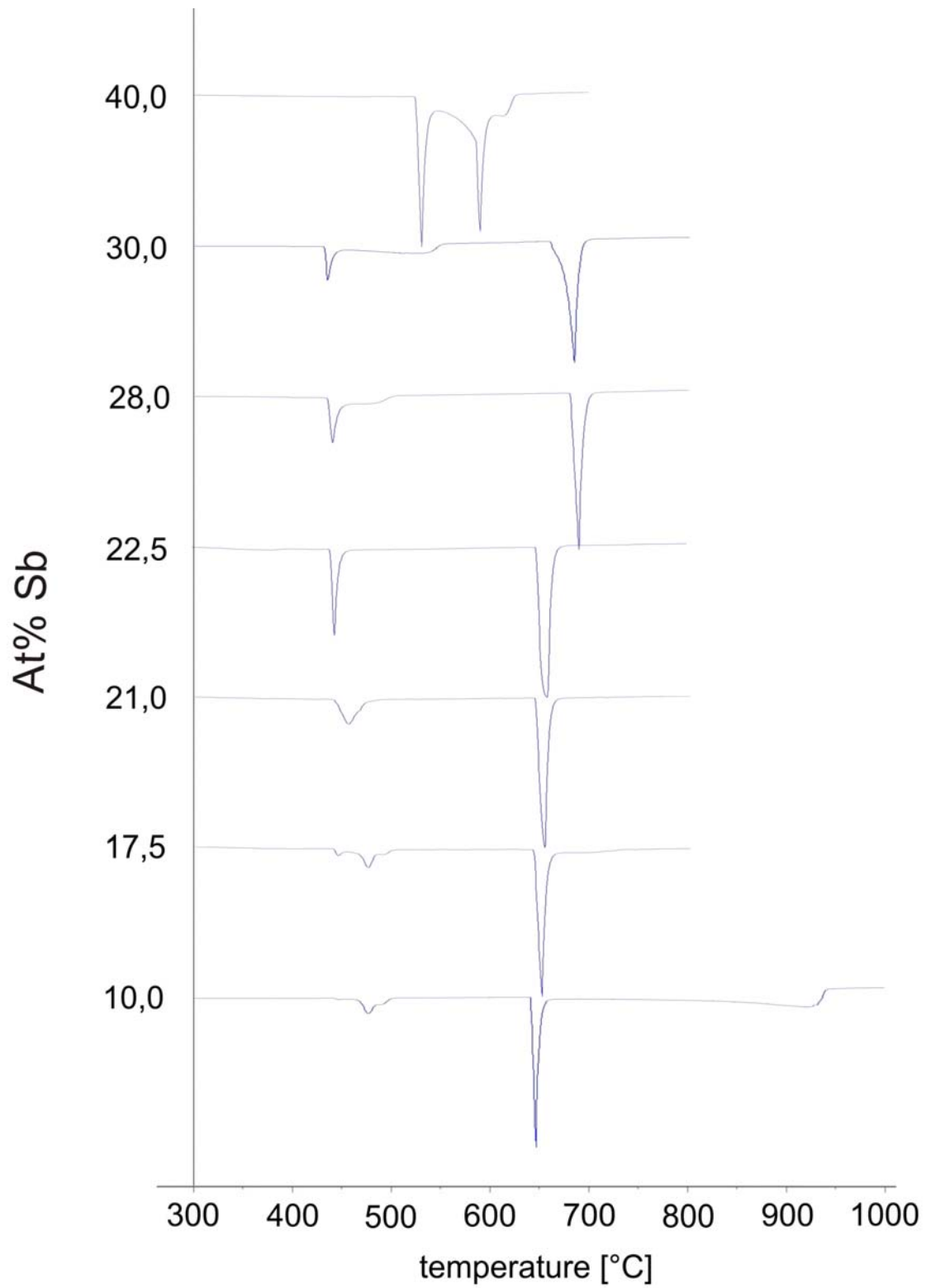
The peritectoid reaction " $\beta + \delta \rightarrow \varepsilon$ " could be corroborated by measuring the samples with 21 and 22.5 at% Sb, only the temperature (440°C) differed five centigrades from the literature value (445°C, [43]). These sample compositions also would have been suitable to prove the existence of the transition temperatures, which affect the ζ -phase (390°C: $\varepsilon + \delta \rightarrow \zeta$; 360°C: $\varepsilon \rightarrow \zeta + \eta$; 260°C: $\zeta \rightarrow \delta + \eta$) and are known since the 1950's [47]. With the exception of the 360°C reaction, which was hardly to resolve in the second heating loop of the sample with 22.5 at% Sb (measured with the Setaram Setsys Evolution), we couldn't detect any of these reaction temperatures. Initially we thought that we already had detected the 360°C reaction with the Netzsch DTA 404S in the samples with 22.5 and 28 at% Sb, but finally we realized that the weak signal came from the reference material, which was nickel with its Curie temperature at 357°C (transformation from ferromagnetic to paramagnetic state).

To investigate the exact formation and decomposition temperatures of the ζ -phase, some measurements with the heat flow DSC (Setaram) are planned. This arrangement is much more sensitive than the common DTA, we hope that also these solid state reactions at low temperatures could be detected. Hence antimony is rather volatile at high temperatures and the measurement is done in open crucibles, the maximum temperature needs to be limited to 500°C. With the samples of 28 and 30 at% Sb we could prove the temperature of the eutectoid reaction " $\beta \rightarrow \varepsilon + \eta$ " at 427°C (literature: 440°C). The liquidus and solidus curves allow an approximation of the congruent melting point of the β -phase at 29 at% Sb and 693°C (literature: 29 at% Sb and 683°C). Finally, we could also prove the eutectic reaction at 526°C ($L \rightarrow \eta + (\text{Sb})$) and the peritectic reaction at 586°C ($\beta + L \rightarrow \eta$).

Table 22: Comparison of reactions and temperatures between literature and this work (Cu-Sb)

Invariant reactions	Temp. (°C), [43]	Temp. (°C), this work	Comments
$L \rightarrow \beta$	683	693	estimated from liquidus curves
$L \rightarrow (\text{Cu}) + \beta$	645	645	
$L + \beta \rightarrow \eta$	586	586	
$L \rightarrow \eta + (\text{Sb})$	526	526	
$(\text{Cu}) + \beta \rightarrow \gamma$	488	467	result differs from literature
$\beta + \gamma \rightarrow \delta$	462	455	result differs from literature
$\beta + \delta \rightarrow \varepsilon$	445	440	result differs from literature
$\beta \rightarrow \varepsilon + \eta$	440	427	result differs from literature
$\gamma \rightarrow (\text{Cu}) + \delta$	400	400	not detected, adopted by literature
$\delta + \varepsilon \rightarrow \zeta$	390	390	not detected, adopted by literature
$\varepsilon \rightarrow \zeta + \eta$	360	360	barely signal
$\zeta \rightarrow \delta + \eta$	260	260	not detected, adopted by literature

Fig. 57: DTA curves 10-40 at % Sb



5.2.2 PXRD at room temperature

As already described in the chapter 4.2 the samples with compositions between 10 and 40 at% Sb were annealed for four weeks at certain temperatures between 340 and 600°C and then quenched in water (see also Table 16). They were powdered and then measured with the Bruker-D8 powder diffractometer. The obtained powder patterns were analyzed with the Topas3[®] software. The results of the PXRD analysis are summarized in Table 24, Table 25 and Fig. 59.

Important for the interpretation of the results is the fact, that the β -phase is a non-quenchable high temperature phase. We only found small amounts of this phase in equilibrium with (Cu) in the quenched sample with 10 at% Sb (quenched from 600°C). The explanation of this exception is that the ductile copper matrix can stabilize smaller amounts of the β -phase. In the diffractogram 10 at% Sb / 600°C we also found an anomaly concerning the peaks associated with the β -phase. Some were very well defined, other ones broadened, but nevertheless the peaks could be clearly assigned to the β -phase. We assume that the quality of crystallisation is not the same in all crystallographic directions. Contrary to the observations in the former sample there were three phases (Cu, β , δ) detectable in the sample with 17.5 at% Sb (also quenched from 600°C). Here the effect of the (Cu)-matrix, which would be necessary to stabilize the larger amount of β -phase, was too little, and therefore the high-temperature phase mainly transformed into the low-temperature- δ -phase (see Fig. 59 and Fig. 60).

Important for the construction of the phase diagram was the sample with 10 at% Sb, quenched from 470°C. We found the three phases (Cu), β and the quenchable high temperature phase γ , which characterize non-equilibrium. The presence of the β -phase, which can be formed only at temperatures above the peritectoid reaction “(Cu) + $\beta \rightarrow \gamma$ ”, indicates a respective reaction temperature below 470°C. This temperature was formerly reported in literature [43] to be at 488°C, but also according to our DTA measurements this reaction is at 467°C. To confirm this result a further PXRD measurement is planned at sample at 10 at% which is quenched from a temperature below 467°C (430-450°C).

In the samples with 17.5 at% Sb, quenched from 470 and 430°C, we obtained γ and δ in equilibrium. We estimate that there was β with a few percent of (Cu) present at the annealing temperature of 470°C, but transformed completely into the stable phases γ and δ during the quenching process. Only the sample quenched from 430°C established an equilibrium state.

The presence of γ in this sample rules out the theory, that the eutectoid reaction “ $\gamma \rightarrow (\text{Cu}) + \delta$ ” took place at 441°C, as it could be concluded from some of our DTA results (small effect at 10 at% Sb: 2nd-4th heating loop; small effect at 17.5 at% Sb: 1st-4th heating loop, see also Fig. 57).

Finally, to finish the discussion of the samples with 10 and 17.5 at% Sb, the presence of the (Cu)- and δ -phase was corroborated at the annealing temperature of 340°C, which is consistent with the literature [43].

In the sample with 21 at% Sb, which was annealed at 470°C, we found the phases δ and ϵ accompanied by a small peak in the diffractogram that could arise from β . We assume that the β -phase was initially formed at the annealing temperature and transformed to the ϵ -phase during quenching. At this composition and at 22.5 at% Sb, both annealed at 430°C, the phases δ and ϵ were formed, which agrees to the literature data [43]. The sample at 22.5 at% also showed non-equilibrium after quenching from 600, 470 and 450°C. We think that the three phases δ , ϵ and η were formed during quenching from the β -single-phase.

When we turn to the lower annealing temperature of 340°C we find a single phase field of ζ in the 21.0 at% Sb sample, which supports the assumption that the ζ -phase is located more at the Cu-rich side than described by the literature [43]. If we additionally consider the ESEM results of the solubility of the δ -phase at the Cu-rich side, we expect the δ - ζ -two-phase-field in a very small concentration range. A second-order transition ($\delta \rightarrow \zeta$) can be ruled out, because there is no sufficient crystallographic relationship between these phases. The δ -phase, which shows the space group $P6_3/mmc$, is no sub- or supergroup of the ζ -phase with the space group $P-3$. In the samples with 22.5 at% Sb, and 28 at% Sb we found the phases ζ and η in equilibrium.

Three samples within which β -phase was present, have been located at 28 at% Sb, quenched from 600°C, and 30 at% Sb, quenched from 600 and 470°C. Here we found the low-temperature phases ε and η with traces of β , we assume that the β -phase formed the other phases during the quenching. Furthermore, in the samples with the compositions 28 and 30 at% Sb, quenched from 430°C, we found the phases ε and η in equilibrium. If we rely on the DTA-results, which indicated an invariant reaction at estimated 427°C ($\beta \rightarrow \varepsilon + \eta$), we should have found β with ε or η in equilibrium in these samples at the annealing temperature of 430°C. The absence of β in the quenched samples is a further evidence for the bulk transformation during quenching.

Finally we annealed samples which should be located in the η -(Sb)-two-phase-field (40 at% Sb) at 340, 470 and 600°C and quenched them. The samples at 340 and 470°C showed an equilibrium of η and (Sb), which agrees with literature data [43]. The sample with 40 at% Sb was already partially molten at 600°C, because it was located between the solidus and the liquidus line. During the quenching two well known, stable phases, namely the ε and η -phase were formed. Additionally traces of β could be stabilized. However, we found a further peak pattern in the diffractogram, which potentially indicates a new phase. This phase could be indexed with the Topas3[®]-software and was assigned as the new cubic phase ι , which has the space group Im-3m and the lattice parameter $a = 9.56918(9)$; see also Table 23. The structure of this phase corresponds to the Ge_7Ir_3 prototype, which was reported by Schubert and Pfisterer in 1950 [62]. Fig. 58 illustrates the X-ray diffractogram of this sample, the calculated curve shows the sum of the contributions of the ε -, η - and β -phase. The difference between the measured and the calculated curve is plotted as the grey curve, which could mainly be explained by the estimated Cu_3Sb_7 -phase (ι -phase). Further experiments are planned to allocate this phase in the phase diagram and for single crystal structure refinement. It could also be a metastable phase, even though the hitherto known metastable phases in Cu-Sb are located in the Cu-rich part.

Fig. 58: Diffractogram of the sample 40 at% Sb, annealed at 600°C and quenched

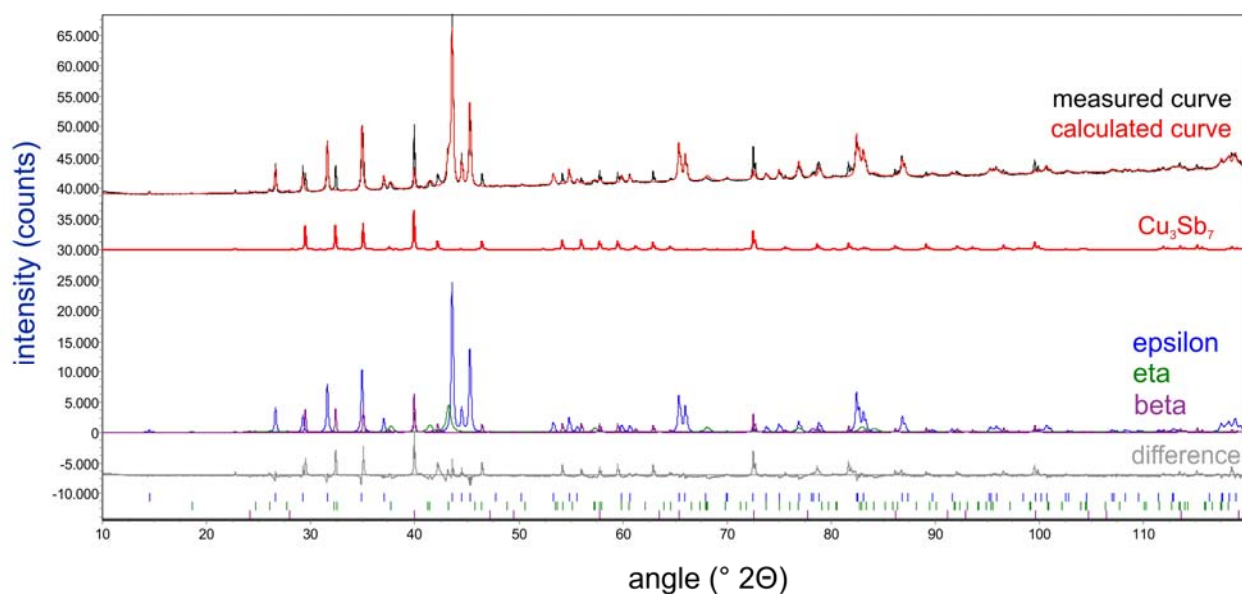


Table 23: Crystallographic data of Cu_3Sb_7 , refined from [62]

Space group: Im-3m		Lattice parameter a = 9.56918(9)			
Atom	multiplicity	x	y	z	occupation
Sb1	12	0.25000	0.00000	0.50000	1
Cu1	12	0.33181	0.00000	0.00000	1
Sb2	16	0.16562	0.16562	0.16562	1

Table 24: Crystal structures and lattice parameters of quenched Cu-Sn-samples

No.	Nominal Comp.	Heat Treatment	Phase Analysis		
			Phase	Structure Type	Lattice Param. (Å)
CA_F_01	Cu ₉₀ Sb ₁₀	340°C, 28d	α = (Cu)	Fm-3m	$a = 3.64479(2)$
			δ = Cu ₇₈ Sb ₂₀	P6 ₃ /mmc	$a = 19.0823(2)$ $c = 4.32615(9)$
		470°C, 28d	α = (Cu)	Fm-3m	$a = 3.62263(2)$
			β = Cu ₃ Sb γ = Cu ₄ Sb	Fm-3m P6 ₃ /mmc	$a = 5.8105(1)$ $a = 3.3521(3)$ $c = 2.8928(5)$
CA_F_02	Cu _{82.5} Sb _{17.5}	340°C, 28d	α = (Cu)	Fm-3m	$a = 3.6482(9)$
			δ = Cu ₇₈ Sb ₂₀	P6 ₃ /mmc	$a = 19.0836(1)$ $c = 4.32763(4)$
		430°C, 28d	γ = Cu ₄ Sb	P6 ₃ /mmc	$a = 2.6950(1)$ $c = 4.3283(4)$
			δ = Cu ₇₈ Sb ₂₀	P6 ₃ /mmc	$a = 19.0033(4)$ $c = 4.3276(2)$
CA_F_03	Cu ₇₉ Sb ₂₁	340°C, 28d	ζ = Cu ₁₀ Sb ₃	P-3	$a = 9.90817(7)$ $c = 4.32364(5)$
			δ = Cu ₇₈ Sb ₂₀	P6 ₃ /mmc	$a = 19.1082(2)$ $c = 4.32665(9)$
		430°C, 28d	ϵ = Cu ₃ Sb	PmmnZ	$a = 5.4920(2)$ $b = 4.34468(8)$ $c = 4.7510(2)$
			β = Cu ₃ Sb δ = Cu ₇₈ Sb ₂₀ ϵ = Cu ₃ Sb	Fm-3m P6 ₃ /mmc PmmnZ	$a = 6.0108(8)$ $a = 19.1990(2)$ $c = 4.33742(8)$ $a = 5.443(1)$ $b = 4.3296(3)$ $c = 4.711(1)$

CA_F_04	Cu _{77.5} Sb _{22.5}	340°C, 28d	$\zeta = \text{Cu}_{10}\text{Sb}_3$ $\eta = \text{Cu}_2\text{Sb}$	P-3 P4/nmm	a = 9.92390(6) c = 4.32223(5) a = 4.0018(2) c = 6.1031(5)
		430°C, 28d	$\delta = \text{Cu}_{78}\text{Sb}_{20}$ $\varepsilon = \text{Cu}_3\text{Sb}$	P6 ₃ /mmc PmmnZ	a = 19.156(1) c = 4.3273(4) a = 5.49427(9) b = 4.34601(5) c = 4.75169(9)
		450°C, 28d	$\delta = \text{Cu}_{78}\text{Sb}_{20}$ $\varepsilon = \text{Cu}_3\text{Sb}$ $\eta = \text{Cu}_2\text{Sb}$	P6 ₃ /mmc PmmnZ P4/nmm	a = 19.022(5) c = 4.4541(9) a = 5.3831(5) b = 4.2871(5) c = 5.0467(6) a = 4.2732(3) c = 5.7367(7)
		470°C, 28d	$\delta = \text{Cu}_{78}\text{Sb}_{20}$ $\varepsilon = \text{Cu}_3\text{Sb}$ $\eta = \text{Cu}_2\text{Sb}$	P6 ₃ /mmc PmmnZ P4/nmm	a = 18.973(4) c = 4.4484(8) a = 5.3763(7) b = 4.2818(5) c = 5.0382(5) a = 4.2675(2) c = 5.7335(7)
		600°C, 28d	$\delta = \text{Cu}_{78}\text{Sb}_{20}$ $\varepsilon = \text{Cu}_3\text{Sb}$ $\eta = \text{Cu}_2\text{Sb}$	P6 ₃ /mmc PmmnZ P4/nmm	a = 18.992(4) c = 4.4519(8) a = 5.3810(9) b = 4.2812(6) c = 5.0447(6) a = 4.2667(2) c = 5.7424(7)
CA_F_05	Cu ₇₂ Sb ₂₈	340°C, 28d	$\zeta = \text{Cu}_{10}\text{Sb}_3$ $\eta = \text{Cu}_2\text{Sb}$	P-3 P4/nmm	a = 9.9206(1) c = 4.3219(1) a = 4.00138(3) c = 6.1032(1)
		430°C, 28d	$\varepsilon = \text{Cu}_3\text{Sb}$ $\eta = \text{Cu}_2\text{Sb}$	PmmnZ P4/nmm	a = 5.5197(2) b = 4.36081(9) c = 4.7898(2) a = 4.00352(4) c = 6.1059(1)
		600°C, 28d	$\beta = \text{Cu}_3\text{Sb}$ $\varepsilon = \text{Cu}_3\text{Sb}$ $\eta = \text{Cu}_2\text{Sb}$	Fm-3m PmmnZ P4/nmm	a = 5.9979(9) a = 5.3919(8) b = 4.2688(7) c = 5.0588(7) a = 4.00016(7) c = 6.0977(2)
CA_F_07	Cu ₇₀ Sb ₃₀	430°C, 28d	$\varepsilon = \text{Cu}_3\text{Sb}$ $\eta = \text{Cu}_2\text{Sb}$	PmmnZ P4/nmm	a = 5.5157(2) b = 4.35768(8) c = 4.7830(1) a = 4.00130(3) c = 6.10265(8)
		470°C, 28d	$\beta = \text{Cu}_3\text{Sb}$ $\varepsilon = \text{Cu}_3\text{Sb}$ $\eta = \text{Cu}_2\text{Sb}$	Fm-3m PmmnZ P4/nmm	a = 6.0384(9) a = 5.5113(5) b = 4.3558(2) c = 4.7796(4) a = 4.00302(2) c = 6.10545(7)
		600°C, 28d	$\beta = \text{Cu}_3\text{Sb}$ $\varepsilon = \text{Cu}_3\text{Sb}$ $\eta = \text{Cu}_2\text{Sb}$	Fm-3m PmmnZ P4/nmm	a = 6.035(3) a = 5.5039(3) b = 4.3540(1) c = 4.7787(2) a = 4.00170(3) c = 6.10306(8)
CA_F_06	Cu ₆₀ Sb ₄₀	340°C, 28d	$\eta = \text{Cu}_2\text{Sb}$ $\theta = (\text{Sb})$	P4/nmm R-3m	a = 4.00172(3) c = 6.10443(9) a = 4.3066(1) c = 11.2689(6)
		470°C, 28d	$\eta = \text{Cu}_2\text{Sb}$ $\theta = (\text{Sb})$	P4/nmm R-3m	a = 4.00204(2) c = 6.10431(7) a = 4.30686(9) c = 11.2708(5)
		600°C, 28d	$\beta = \text{Cu}_3\text{Sb}$ $\varepsilon = \text{Cu}_3\text{Sb}$ $\eta = \text{Cu}_2\text{Sb}$ $\iota = \text{Cu}_3\text{Sb}_7$	Fm-3m PmmnZ P4/nmm Im-3m	a = 6.3796(2) a = 5.507(6) b = 4.3536(6) c = 4.771(5) a = 4.00162(4) c = 6.1036(1) a = 9.5689(1)

Table 25: Found Cu-Sb phases in the PXRD analysis

sample	Annealing temperature (°C)					
	arc	340	430	450	470	600
Cu ₉₀ Sb ₁₀	(Cu), δ	(Cu), δ			(Cu), β , γ	(Cu), β
Cu _{82.5} Sb _{17.5}	δ , ϵ	(Cu), δ	γ , δ		γ , δ	(Cu), β , δ
Cu ₇₉ Sb ₂₁	δ , ϵ	ζ	δ , ϵ		β , δ , ϵ	
Cu _{77.5} Sb _{22.5}	δ , ϵ	ζ , η	δ , ϵ	δ , ϵ , η	δ , ϵ , η	δ , ϵ , η
Cu ₇₂ Sb ₂₈	ϵ , η	ζ , η	ϵ , η			β , ϵ , η
Cu ₇₀ Sb ₃₀			ϵ , η		β , ϵ , η	β , ϵ , η
Cu ₆₀ Sb ₄₀	η , (Sb)	η , (Sb)			η , (Sb)	β , ϵ , η , ι

5.2.3 ESEM / EPMA

To measure the solubility of copper and antimony in the equilibrium phases, we employed the ESEM (Zeiss Supra 55 VP) and the EPMA (CAMECA SX 100) method. Due to its easier availability for most measurements the ESEM was used. Only for the first few measurement series we used the EPMA (samples annealed at 340°C). In the WDX mode (EPMA), as well as in the EDX mode (ESEM) we chose the K-line to measure Cu and the L-line for Sb.

The solubility of antimony in the (Cu)-phase was similar to the literature value [43], attributed to our results we estimated a higher solubility at the eutectic temperature (645°C: 6.7 at% Sb) and a significant lower solubility at the lower annealing temperatures (470°C: 3.9 at% Sb; 340°C: 2.7 at% Sb). All results are listed in Table 26 and presented as a chart in Fig. 59.

The β -phase, which only could be distinguished from the other phases in the samples with 10 and 17.5 at% Sb, had a solubility at 600°C in the range of 19.8 at% Sb at the Cu-rich side. The solubility at lower temperatures, as well as the solubility behaviour at the Sb-rich side couldn't be obtained from quenched samples; see also chapter 5.2.2.

Contrary to this experience with the β -phase, the γ -phase could easily be obtained by quenching. We got a very similar homogeneity range as described by the literature [43], and we suggest for the limit of the γ -phase at the Cu-rich side 15 at% Sb, 0.5 at% lower than given in [43].

The largest divergence from the literature resulted for the δ -phase. At lower temperatures we found a composition of 20.6 at% Sb for δ at the Cu-rich side. The solubility limit is shifted towards higher Cu-contents at higher temperatures, which is illustrated by an enlarged phase field at the high temperature region. We estimate a maximum of the Cu-solubility at 17.8 at% Sb (at the peritectoid temperature of 455°C). At the Sb-rich side of the δ -phase we can find an increasing solubility of Sb, coming along with lower temperatures, giving the whole phase field a club shape. We tried to prove the δ - ζ -two phase field with the sample at 21.0 at% Sb, quenched from 340°C. Because there was only pure ζ -phase detectable in the PXRD, according to the observed dark phase with traces of bright η in the ESEM (probably remaining from a non-equilibrium state), we couldn't measure the composition of δ at the Sb-rich side. Therefore we conclude that the δ - ζ -two phase field exists in a much smaller composition range at compositions below 21 at% Sb.

The ζ -phase at 340°C showed a composition in the range between 22.0 and 22.8 at% Sb. According to the DTA-results for the sample at 22.5 at% Sb (signal at 360°C), we approximate the maximum extension of the ζ -phase at 22.3 at% Sb and at 360°C for the Sb-rich side.

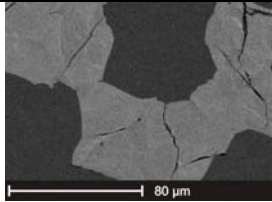
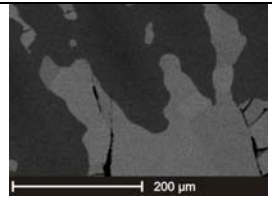
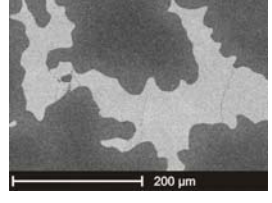
The interpretation of the ESEM data regarding the ε -phase is much more challenging. We only considered data, which were obtained from equilibrium samples, according to the DTA and PXRD measurements. Because ε is formed in a peritectoid reaction at 440°C from δ and β , we can thus only use the data obtained from the two samples quenched from 430°C, with the compositions 21.0 and 22.5 at% Sb. Unfortunately, the found compositions for the ε -phase differed between 21.1 and 23.4 at% Sb. We know that the sample with 22.5 at% Sb had a DTA-signal at 440°C and from the PXRD data that δ and ε were in equilibrium at 430°C, hence the peritectoid point for the formation of ε is estimated at 22.3 at% Sb and 440°C. The phase borders, which were obtained from 430°C-annealed and afterwards quenched samples (sample composition 28 and 30 at% Sb), resulted from the decomposition of the β -phase to ε and η at 427°C. We found one composition at 22.6 at% Sb, which could be related to the solvus line at the top side of the ε -phase. The most confidential value seemed to be the composition in the 30 at% Sb sample, which was 24.9 at% Sb. This value determines the ε – concentration in the eutectoid reaction $\beta \rightarrow \varepsilon + \eta$.

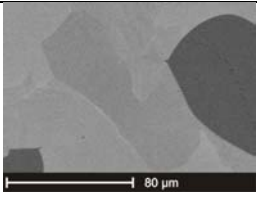
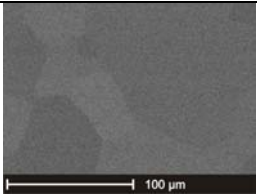
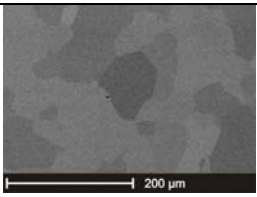
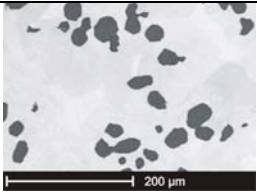
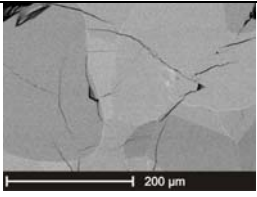
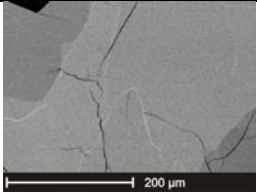
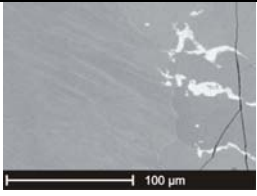
The shape and extension of the η -phase field at temperatures below 470°C confirmed the literature data [43]. We found the η -phase field between 33.9 and 34.4 at% Sb, for both boundaries this was about 1% higher than reported in literature. In the samples with 30 and 40 at% Sb, both quenched from 470°C, we found that the composition of the η -phase was 1-2 at% lower than at temperatures below 470°C (Cu-rich side: 31.4 at% Sb; Sb-rich side: 31.7 at% Sb). There are two possibilities to interpret these data. On the one hand it could be, and this is rather unlikely, that the η -phase shows a hard bend to the Cu-rich side after the eutectic reaction at 427°C and ends up in a line compound. On the other hand, and this is the better explanation, there could be a systematic error in the measurements about 1 %, for samples annealed at lower temperatures towards the Sb-rich side, and for samples which were annealed at higher temperatures towards the Cu-rich side. To clarify this situation, there have to be done some further measurements. Meanwhile we trust the data obtained from the samples annealed at lower temperatures, and suggest that the η -phase-field is shaped as estimated in literature.

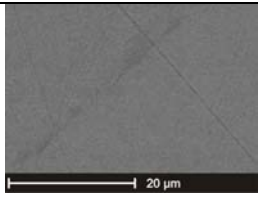
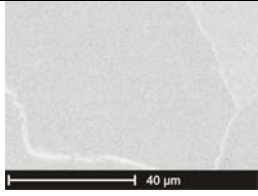
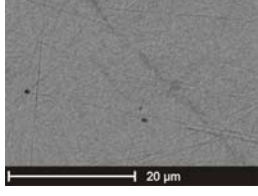

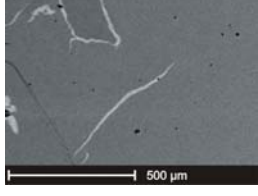

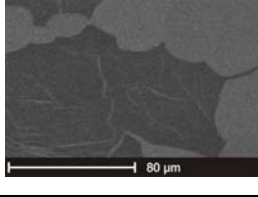
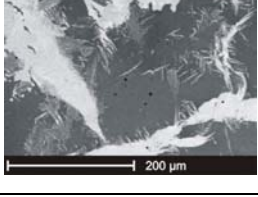
Finally we found the (Sb)-phase in the samples at 40 at% Sb. The results differed between 99.9 at% (470°C) and 98.2 at% (340°C). We know from the literature [43] that there is nearly no solubility of Cu in (Sb), we confirm this report with the higher Sb content at 470°C.

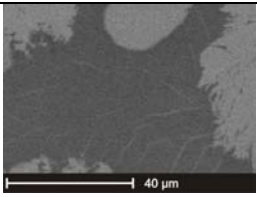
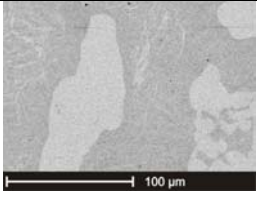
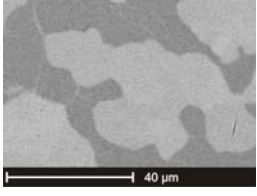
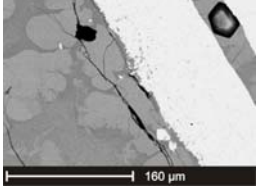
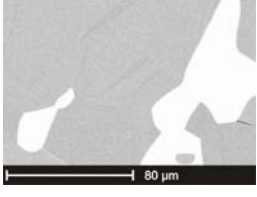
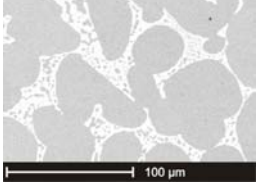
The new phase Cu_3Sb_7 , which was obtained from the sample with 40 at% (quenched from 600°C) could not be found in the ESEM. In spite of this indication we will do further samples and measurements to prove the existence of Cu_3Sb_7 .

Table 26: ESEM/EPMA results of Cu-Sb phase compositions

Sample	Ann.-temp.	phase 1 (dark)			phase 2 (bright)			SEM image
			at% Cu	at% Sb		at% Cu	at% Sb	
$\text{Cu}_{90}\text{Sb}_{10}$	600°C	(Cu)	94.1	5.9	β_{Cu}	80.2	19.8	
	470°C	(Cu)	96.0	4.0	γ_{Cu}	85.3	14.7	
	340°C	(Cu)	97.3	2.7	δ_{Cu}	79.3	20.7	

Cu _{82.5} Sb _{17.5}	600°C	(Cu)	94.1	5.9	β_{Cu}	80.3	19.7	
					$*\delta_{\text{Cu}}$	78.9	21.1	
	470°C	γ_{Sb}	84.7	15.3	δ_{Cu}	83.3	16.7	
	430°C	γ_{Sb}	84.4	15.6	δ_{Cu}	83.0	17.0	
Cu ₇₉ Sb ₂₁	340°C	(Cu)	97.4	2.6	δ_{Cu}	79.1	20.9	
	470°C	δ_{Sb}	82.4	17.6	ϵ_{Cu}	79.6	20.4	
					ϵ_{Cu}	78.9	21.1	
	430°C	δ_{Sb}	81.7	18.3	$*\eta_{\text{Cu}}$ (white lines)	70.6	29.4	
	340°C	ζ_{Sb}	78.3	21.7	η_{Cu}	66.1	33.9	

Cu _{77.5} Sb _{22.5}	600°C	#mixed phase	77.1	22.9				
	470°C	ε _{Cu}	76.1	23.9	#η _{Cu} + ε _{Cu}	69.8	30.2	
	450°C	#mixed phase	76.6	23.4				
	430°C	δ _{Sb}	79.6	20.4	ε _{Cu}	76.7	23.4	
	340°C	ζ _{Sb}	77.9	22.1	η _{Cu}	65.8	34.2	
Cu ₇₂ Sb ₂₈	600°C	ε _{Sb}	73.4	26.6	η _{Cu}	67.4	32.6	
	430°C	ε _{Sb}	74.3	25.7	η _{Cu}	66.6	33.4	
	340°C	ζ _{Sb}	78.0	22.0	η _{Cu}	65.5	34.5	

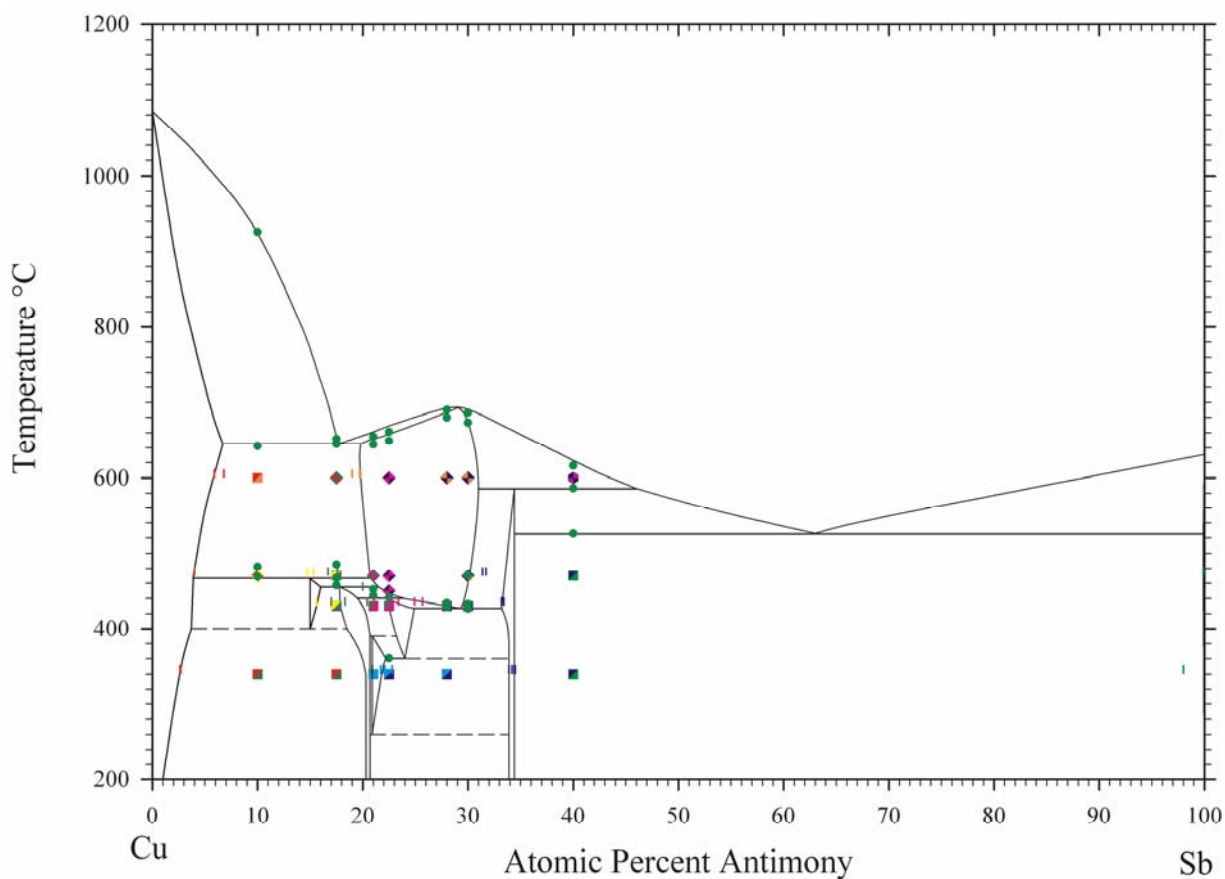
Cu ₇₀ Sb ₃₀	600°C	ε _{Sb}	74.0	26.0	η _{Cu}	64.5	35.5	
	470°C	ε _{Sb}	77.0	23.0	η _{Cu}	68.6	31.4	
	430°C	ε _{Sb}	75.1	24.9	η _{Cu}	66.8	33.2	
Cu ₆₀ Sb ₄₀	600°C	*ε _{Sb} or β _{Sb}	76.3	23.7	η _{Sb}	69.3	30.7	
					(Sb) (white phase)	0.6	99.5	
	470°C	η _{Sb}	68.3	31.7	(Sb)	0.1	99.9	
	340°C	η _{Sb}	65.6	34.4	(Sb)	2.0	98.0	

* non-equilibrium (shows more than 2 phases)

not fully resolvable (too small precipitated grains)

5.2.4 Phase diagram Cu-Sb

Fig. 59: Developed Cu-Sb phase diagram, including data points



PXRD ESEM / EPMA thermal analysis

- alpha delta
- gamma delta
- delta epsilon
- zeta
- zeta eta
- beta epsilon eta
- epsilon eta
- eta theta
- alpha beta
- alpha beta gamma
- alpha beta delta
- beta delta epsilon
- delta epsilon eta
- beta epsilon eta iota

- (Cu)
- beta
- gamma
- delta
- epsilon
- zeta
- eta
- (Sb)

- DTA

Table 27: Comparison temperature-invariant reactions in the Cu-Sb-system this work and literature [43]

Reaction	Composition (at% Sb)			Temp. (°C)	Reaction type
$L \rightarrow \beta$		29.0 (29.0)		693 (683)	Congruent melting
$L \rightarrow (Cu) + \beta$	6.7 (5.8)	17.7 (19)	19.8 (19.5)	645 (645)	Eutectic
$L + \beta \rightarrow \eta$	31.0 [#]	34.5 (33.5)	46.0 [#]	586 (586)	Peritectic
$L \rightarrow \eta + (Sb)$	34.5 (33.5)	63.0 [#]	99.9 (99.9)	526 (526)	Eutectic
$(Cu) + \beta \rightarrow \gamma$	3.9 (5.65)	15.0 (15.5)	20.7 (21.5)	467 (488)	Peritectoid
$\beta + \gamma \rightarrow \delta$	16.0 (16.5)	17.8 (19.0)	21.5 (24.0)	455 (462)	Peritectoid
$\beta + \delta \rightarrow \varepsilon$	19.5 (19.5)	22.9 (23.0)	13.3 (25.5)	440 (445 [*])	Peritectoid
$\beta \rightarrow \varepsilon + \eta$	24.9 (25.5)	29.3 (26.5)	33.2 (32.0)	427 (440 [*])	Eutectoid
$\gamma \rightarrow (Cu) + \delta$	3.7 (4.6)	15.0 (15.5)	18.5 (18.5)	400 ^{#*}	Eutectoid
$\delta + \varepsilon \rightarrow \zeta$	20.7 (20.0)	20.9 (21.5)	22.7 (23.5)	390 ^{#*}	Peritectoid
$\varepsilon \rightarrow \zeta + \eta$	22.2 (22.5)	24.0 [#]	33.9 (32.5)	360 (360)	Eutectoid
$\zeta \rightarrow \delta + \eta$	20.7 (20)	20.9 (21.5)	33.9 (32.5)	260 [*]	Eutectoid

* uncertain temperatures

[#] value adopted from literature [43]

(value)... literature value [43]

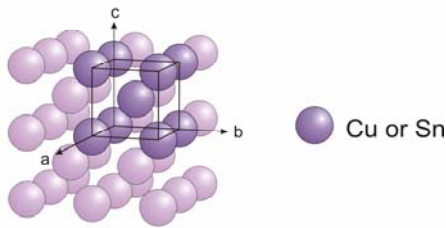
5.3 Comparison of Cu-Sn and Cu-Sb

In this section the relationship between the systems Cu-Sn and Cu-Sb will be discussed. Tin and antimony are neighbours in the periodic table of the elements, therefore they have very similar properties. Crucial for the understanding of their behaviour in alloys is the knowledge about the size and the electronegativity of the atoms. The atomic radius of copper is 127.8 pm, this is a little bit smaller than the radii of tin (140.5 pm) and antimony (141 pm). The values for the electronegativity are 1.90 (Cu), 1.96 (Sn) and 2.05 (Sb); see also Tables 4-6. Antimony is a little bit more electronegative, it already shows semi-metallic character. This is interesting for the prediction of macroscopic properties. Although the difference of the electronegativity gap between Cu-Sn, and Cu-Sb respectively, seems to be negligible, the Cu-Sb alloys are much more brittle than the Cu-Sn alloys. The typical metallic bonding, as shown between atoms with similar electronegativity, provides a ductile behaviour of the alloy (Cu-Sn). Due to the delocalisation of the binding energy in the electron gas the metallic bonding can reversible switch in the original position after deformation. If the difference in the electronegativity increases (Cu-Sb), the alloy becomes more like a ceramic, because the bindings show more and more covalent character. At deformation these localized bindings with defined energy content suddenly break.

When we consider the high temperature phases of both systems, we find out that the crystal structures are dominated by the BiF_3 -type. This kind of metastable structure appears in the β -phase of Cu-Sb and in the γ -phase of Cu-Sn. The BiF_3 -type can't be stabilized quantitatively by quenching, it forms several other stable or metastable phases during decomposition. In both systems the decomposition of the BiF_3 -type mainly happens in eutectoid reactions (Cu-Sn: $\gamma \rightarrow (\text{Cu}) + \delta$; Cu-Sb: $\beta \rightarrow \varepsilon + \eta$).

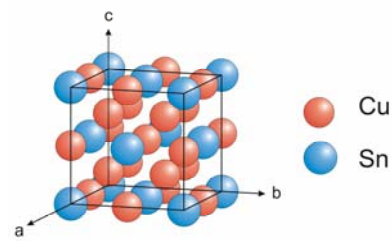
The high-temperature phases in the Cu-Sn system are based on a cubic lattice. The simplest structure is the W-type β -phase, which is a bcc cell. Here the atoms Cu and Sn are randomly arranged at low Sn contents (see Fig. 61). With increasing Sn content the Cu atoms have to occupy certain sites between the Sn atoms, because Sn is a large atom and forms densely packed planes (see Fig. 62). Diffusion processes are hindered due to the dense layer of Sn in the (111) plane. This forces the formation of the γ -phase, which is an ordered BiF_3 -type with the double lattice parameter of the β -phase.

Fig. 61: Randomly arranged atoms in the W-type (Cu-Sn)



Atoms in unit cell are shadowed

Fig. 62: Well ordered atoms in the BiF₃-type (Cu-Sn)



The phase transitions in Cu-Sb are similar, but a little bit more complicate. Initially a BiF₃-type phase (β) is formed from the melt. The lattice parameter of this phase is smaller than that one of the Cu-Sn- BiF₃-type (Cu-Sn: 6.1176Å; Cu-Sb: 6.0000Å). This could be explained by the higher attracting forces between the Cu and the Sb atoms (higher difference in the electronegativity), therefore the bonding distance between the atoms decrease. The β -phase only exists above 427°C, below this temperature it decomposes to the stable ϵ -phase. Those two structures are closely related, as shown in Fig. 63 and Fig. 64. ϵ can be obtained from beta by shifting a certain layer of atoms along the c-axis.

Fig. 63: Cu-Sb β -phase, crystal and (010) plane

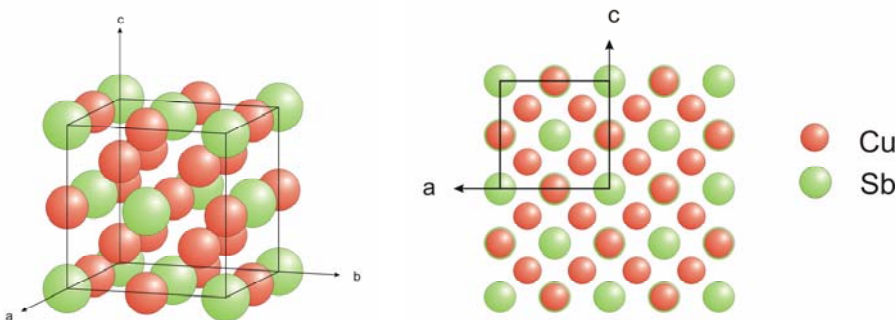
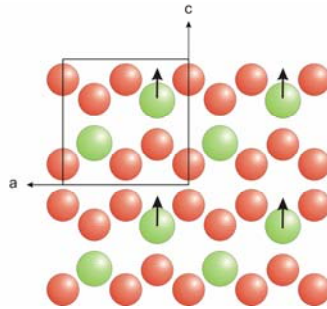


Fig. 64: Cu-Sb ϵ -phase, (010) plane; arrows show transformation of $\epsilon \rightarrow \beta$



The stable Cu-Sb phases, except (Cu), are based on crystal structures with lower symmetry than the cubic lattice (e.g. hexagonal symmetry). This could be explained again with the semi-metal character of Sb. The more covalent nature of bindings deforms the crystals to structures with lower symmetry. According to this assumption the electronegativities of Cu and Sn are similar, respectively the bindings lead to less deformation, therefore we can observe here mainly high-symmetric cubic structures. It is noteworthy, that the cubic and the hexagonal structures, namely the face centered cubic and the hexagonal close packed structure, are related and can be converted into each other. If we look at the fcc structure along the $\langle 111 \rangle$ axis, it becomes clear that it differs from the hcp cell only in the sequence of the stacked levels of close packed atoms. The hcp cell consists of two alternating layers, whereas the fcc cell can be described by three different layers which will be repeated along the $\langle 111 \rangle$ axis (see Fig. 65).

However, if we apply this rule to the hcp Cu-Sb γ -phase, which is the simplest structure in this system (Mg-type, two atoms per unit cell), we have to realise that it cannot be transformed to a cubic lattice, because of a a/c -relation which deviates from a close packaging (see Fig. 66 – 68).

Fig. 65: Comparison hcp vs. fcc unit cell

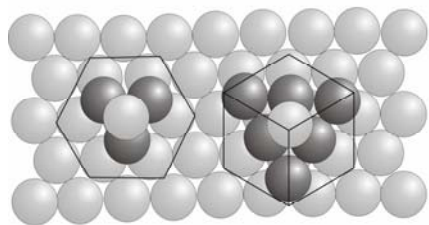


Fig. 66: Cu-Sb β -phase (BiF_3 -type), view along $\langle 111 \rangle$ axis

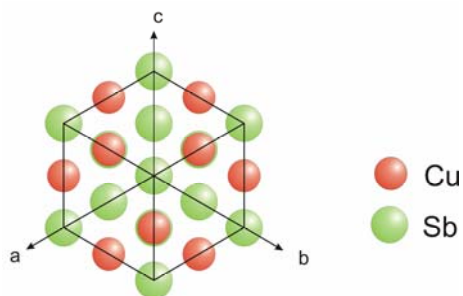


Fig. 67: Crystal and unit cell of the γ -phase (Mg-type)

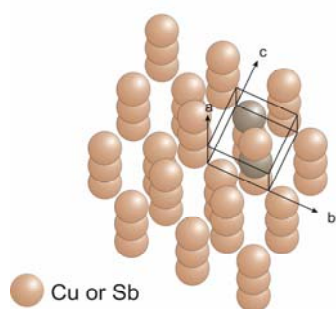
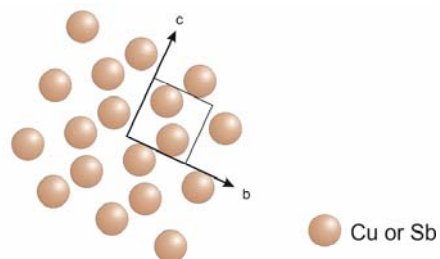


Fig. 68: Cu-Sb γ -phase (Mg-type), (100) plane



Atoms in unit cell are shadowed

6 Summary

6.1 Summary (English)

The two binary systems Cu-Sn and Cu-Sb were investigated with various experimental methods (DTA, PXRD, HTPXRD, ESEM, EPMA). Additionally for the Cu-Sn system the available literature data since 1894 was summarized in a detailed literature review.

For the Cu-Sn system the controversial discussion about the transition order between the high temperature phases β (W-type) and γ (BiF₃-type) was set out. The data, especially those gained by the high temperature X-ray diffraction method, support the theory of a second-order transition between those phases, the existence of a β - γ -two-phase field seems to be unlikely (see Fig. 55 and 56). Accordingly, the interpretation of the thermal analysis (DTA) allows the assumption of the presence of two degenerated invariant reactions at 566 and 758°C (see Table 21). Some further invariant reactions were shifted to marginal different temperatures than described by the literature [15], as well as the solubility ranges of the occurring phases were adapted (from ESEM / EPMA data).

To investigate the Cu-Sb system the same methods, excepting the HTPXRD, were employed. It was tried to confirm the present phase diagram [43] and clarify the less investigated parts of the phase diagram (see Fig. 59 and Fig. 60). The thermal analysis agreed well to the literature, nevertheless some adaptations for the invariant reaction temperatures were necessary (see Table 27). Especially those reactions which were located at the Cu-rich side of the metastable high temperature phase β (BiF₃-type) left leeway for interpretations and require further investigation. The solubility of the δ -phase (Cu₇₈Sb₂₁-type) seemed to increase at temperatures above 340°C. The δ - ζ -two-phase field was found to be much narrower and was located at a lower Sb-content. The eutectoid point at 427°C (decomposition of the β -phase) was adapted to a value of about 3 at% Sb higher than estimated before, additionally the η -phase was found at a 1-2 at% higher composition of Sb. By quenching of a sample with 40 at% Sb from 600°C (liquidus-solidus-field) the new phase ι (Ge₇Ir₃-type) with an estimated composition of Cu₃Sb₇ was found in the PXRD, which has to be verified by further experiments.

6.2 Zusammenfassung (Deutsch)

Die binären Systeme von Cu-Sn und Cu-Sb wurden in der vorliegenden Arbeit mittels mehrerer experimenteller Methoden untersucht (DTA, PXRD, HTPXRD, ESEM, EPMA). Zusätzlich wurde für das Cu-Sn-System die vorhandene Literatur seit 1894 aufgearbeitet und in einer detaillierten Zusammenfassung dargestellt.

Die kontroverse Diskussion über die Art des Übergangs zwischen den Hochtemperaturphasen von Cu-Sn, namentlich die β -Phase (W-Typ) und die γ -Phase (BiF_3 -Typ), wurde wieder aufgegriffen. Die Messdaten der HTPXRD unterstützten die Theorie einer diffusionslosen und daher spontanen β - γ -Umwandlung, die Existenz eines β - γ -Zweiphasenmischgebiets wurde als unwahrscheinlich angesehen (siehe Abb. 55 und 56). Weiters erlaubte die Interpretation der Daten aus der thermischen Analyse (DTA) die Annahme zweier degenerierter invarianter Reaktionen bei 566 und 758°C, die aus dem β - γ -Übergang resultierten und in den Zweiphasengebieten (Cu)- β bzw. β -liquidus als schwache Signale aufscheint (siehe Tabelle 21). Einige weitere invariante Reaktionen wurden bei geringfügig abweichenden Temperaturen, im Vergleich zur Literatur [15], beschrieben.

Das Cu-Sb-System wurde mit denselben Methoden, mit Ausnahme der HTPXRD, untersucht. Es wurde versucht das vorliegende Phasendiagramm [43] zu bestätigen und die als ungesichert betrachteten Annahmen zu überprüfen (siehe Abb. 59 und 60). Die thermische Analyse stimmte gut mit der Literatur überein, nichtsdestotrotz mussten für einige Temperaturen, bei denen invariante Reaktionen beschrieben wurden, Anpassungen getroffen werden. Besonders die Reaktionen, welche die Hochtemperaturphase β (BiF_3 -Typ) entlang der kupferreichen Seite betrafen, ließen Interpretationsspielraum zu und bedürfen weiterer Beforschung. Die Löslichkeit von Kupfer in der δ -Phase ($\text{Cu}_{78}\text{Sb}_{21}$ -Typ) war bei Temperaturen über 340°C erhöht. Das δ - ζ -Zweiphasenmischgebiet wurde in einem schmäleren Konzentrationsbereich und bei niedrigerem Sb-Gehalt gefunden. Der eutektische Punkt bei 427°C (Zersetzung der β -Phase) wurde an einen um 3 at% Antimon erhöhten Wert angepasst. Zusätzlich wurde die η -Phase bei einer um 1-2 at% Sb erhöhten Zusammensetzung gefunden. Die Probe mit der Zusammensetzung $\text{Cu}_{60}\text{Sb}_{40}$, welche bei 600°C gegläht (Flüssig-Fest-Mischgebiet) und anschließend abgeschreckt wurde, zeigte im Röntgendiffraktogramm die bis dato unbekannte Phase ι (Ge_7Ir_3 -Typ) mit einer angenommenen Zusammensetzung Cu_3Sb_7 . Dieser Befund muss allerdings noch durch weitere Untersuchungen überprüft werden.

7 References

1. Wuich, W., *Löten. Lötverfahren, Lote, Flußmittel, Anwendungstechniken*. 1972, Würzburg: Vogel. 168 S.
2. Karakaya, I. and W.T. Thompson, eds. *Pb-Sn (Lead-Tin)*. 2 ed. Binary Alloy Phase Diagrams, ed. T.B. Massalski. Vol. 3. 1988, The Materials Information Society: Ohio. 3014-3017.
3. Mikula, A. *Skriptum zur VO "Anorganische Technologie"*. 2010; Available from: <http://homepage.univie.ac.at/adolf.mikula/Anorg-Tech.ppt>.
4. COST_Action_MP0602. <http://cost602.ipm.cz/mp0602-mou.pdf>. 2010.
5. Heise-online. 2010; Available from: <http://www.heise.de/newsticker/meldung/Zoelle-auf-Multi-Chip-Bausteine-abgeschafft-145024.html>.
6. Emsley, J., *The Elements*. 1989, Oxford: Clarendon Press.
7. Schlaepfer-Altmetall, C. http://www.schlaepfer-altmetall.ch/medien/wertstoffe/img/kupfer_millberry.jpg.
8. Trueb, L.F., *Die chemischen Elemente*. 1996, Leipzig: S. Hirzel Verlag.
9. Kantola, M. and E. Tokola, eds. *X-ray studies on the thermal expansion of copper-nickel alloys*. 2 ed. Pearson's Handbook of Crystallographic Data for Intermetallic Phases, ed. P. Villars and L.D. Calvert. Vol. 3. 1967, The Materials Information Society: Materials Park, Ohio. 2785.
10. Cotton, F.A. and G. Wilkinson, *Anorganische Chemie*. 4 ed. 1980, Weinheim: Verlag Chemie.
11. Infocom Network Limited, I. <http://product-image.tradeindia.com/00155169/b/0/Tin-Ingot.jpg>.
12. Musée d'histoire naturelle Fribourg, C. <http://www.fr.ch/mhn/images/mineraux/antimoni.jpg>.
13. Le Chatelier, H., *Sur la loi générale de solubilité des corps normaux*. Comptes Rendus, 1894: p. 638-644.
14. Heycock, C.T. and F.H. Neville, *Complete freezing-point curves of binary alloys*. Philosophical Transactions of the Royal Society of London Series a-Containing Papers of a Mathematical or Physical Character, 1897. A189: p. 47-51, 62-66.
15. Saunders, N. and A.P. Miodownik, *The Cu-Sn (Copper-Tin) System*. Bulletin of Alloy Phase Diagrams, 1990. 11: p. 278-287.

16. Heycock, C.T. and F.H. Neville, *On the constitution of the copper-tin series of alloys*. Philosophical Transactions of the Royal Society of London Series a-Containing Papers of a Mathematical or Physical Character, 1904. 202: p. 1-70.
17. Shepherd, E.S. and E. Blough, *The constitution of the copper-tin alloys*. Journal of Physical Chemistry, 1906. 10(8): p. 630-653.
18. Verö, J., *The composition of tin bronzes*. Zeitschrift Fur Anorganische Und Allgemeine Chemie, 1934. 218(4): p. 402-424.
19. Hamsumi, M. and S. Nishigori, Tech. Repts. Tōhoku Univ., 1931. 10: p. 131-187.
20. Raynor, G.V., *The equilibrium diagram of the system copper-tin*. Annotated Equilibrium Diagram Series, 1944. 2.
21. Knödler, H., *Die Überstruktur der gamma-Hochtemperaturphase im System Kupfer-Zinn*. Acta Crystallographica, 1956. 9: p. 1036.
22. Knödler, H., *Über Kristallstruktur und strukturellen Zusammenhang der Phasen gamma und epsilon im System Kupfer-Zinn*. Metall, 1966. 20(8): p. 823-829.
23. Baur, W.H. and A.A. Khan, eds. *Rutile-Type Compounds. IV. SiO₂, GeO₂ and a Comparison with other Rutile-Type Structures*. 2 ed. Pearson's Handbook of Crystallographic Data for Intermetallic Phases, ed. P. Villars and L.D. Calvert. Vol. 3. 1971, The Materials Information Society: Materials Park, Ohio. 4765.
24. Ganguluee, A., G.C. Das, and M.B. Bever, eds. *An X-Ray Diffraction and Calorimetric Investigation of the Compound Cu₆Sn₅*. 2 ed. Pearson's Handbook of Crystallographic Data for Intermetallic Phases, ed. P. Villars and L.D. Calvert. Vol. 3. 1973, The Materials Information Society: Materials Park, Ohio. 3007.
25. Brandon, J.K., W.B. Pearson, and D.J.N. Tozer, *A Single-Crystal X-ray Diffraction Study of the zeta Bronze Structure, Cu₂₀Sn₆*. Acta Crystallographica, 1975. B31: p. 774-779.
26. Booth, M.H., et al., *Gamma-Brasses with F Cells*. Acta Crystallographica Section B-Structural Science, 1977. 33(Jan15): p. 30-36.
27. Watanabe, Y., Y. Fujinaga, and H. Iwasaki, *Lattice Modulation in the Long-Period Superstructure of Cu₃Sn*. Acta Crystallographica Section B-Structural Science, 1983. 39(Jun): p. 306-311.
28. Hansen, M.A., K., *Cu-Sn Copper-Tin*. 2 ed. Constitution of Binary Alloys. ed. K.A. M. Hansen. 1985, New York: Genum Publishing Corporation. 1304.

29. Saunders, N. and A.P. Miodownik, eds. *Cu-Sn (Copper-Tin)*. 2 ed. Binary Alloy Phase Diagrams, ed. T.B. Massalski. Vol. 2. 1990, The Materials Information Society: Ohio. 1481-1483.
30. Shim, J.H., et al., *Thermodynamic assessment of the Cu-Sn system*. Zeitschrift für Metallkunde, 1996. 87(3): p. 205-212.
31. Liu, X.J., et al., *Experimental investigation and thermodynamic calculation of the phase equilibria in the Cu-Sn and Cu-Sn-Mn systems*. Metallurgical and Materials Transactions a-Physical Metallurgy and Materials Science, 2004. 35A(6): p. 1641-1654.
32. Gierlotka, W., S.W. Chen, and S.K. Lin, *Thermodynamic description of the Cu-Sn system*. Journal of Materials Research, 2007. 22(11): p. 3158-3165.
33. Li, M., et al., *Thermodynamic optimization of the Cu-Sn and Cu-Nb-Sn systems*. Journal of Alloys and Compounds, 2009. 477(1-2): p. 104-117.
34. Knödler, H., ed. *Über Kristallstruktur und strukturellen Zusammenhang der Phasen gamme und epsilon im System Kupfer-Zinn*. 2 ed. Pearson's Handbook of Crystallographic Data for Intermetallic Phases, ed. P. Villars and L.D. Calvert. Vol. 3. 1966, The Materials Information Society: Materials Park, Ohio. 3008.
35. Hoyt, S.L., *On the copper-rich kalchoids (copper-tin-zinc alloys)*. Journal of the Institute of Metals, 1913. 10: p. 235-274.
36. Hoyt, S.L., *Constitution of tin bronzes*. Transactions of the American Institute of Mining and Metallurgical Engineers, 1919. 60: p. 198-203.
37. Vollenbruck, O.B.O., *Das Erstarrungs- und Umwandlungsschaubild der Kupfer-Zinnlegierungen*. Zeitschrift für Metallkunde, 1923. 15(5): p. 119-125; 191-195.
38. Hamasumi, M. and N. Takamoto, Nippon Kinzoku Gakkai-Si, 1937. 1: p. 251.
39. Watanabe, Y., Y. Fujinaga, and H. Iwasaki, eds. *Lattice Modulation in Long-Period Superstructure of Cu₃Sn*. 2 ed. Pearson's Handbook of Crystallographic Data for Intermetallic Phases, ed. P. Villars and L.D. Calvert. Vol. 3. 1983, The Materials Information Society: Materials Park, Ohio. 3006-3007.
40. Brandon, J.K., W.B. Pearson, and D.J.N. Tozer, eds. *A Single-crystal X-ray Diffraction Study of the zeta-Bronze Structure, Cu₂₀Sn₆*. 2 ed. Pearson's Handbook of Crystallographic Data for Intermetallic Phases, ed. P. Villars and L.D. Calvert. Vol. 3. 1975, The Materials Information Society: Materials Park, Ohio. 3007.
41. Larsson, A.K., L. Stenberg, and S. Lidin, *The Superstructure of Domain-Twinned Eta'-Cu₆Sn₅*. Acta Crystallographica Section B-Structural Science, 1994. 50: p. 636-643.

42. Lee, J.A. and G.V. Raynor, eds. *The lattice Spacings of binary Tin-Rich Alloys*. 2 ed. Pearson's Handbook of Crystallographic Data for Intermetallic Phases, ed. P. Villars and L.D. Calvert. Vol. 3. 1954, The Materials Information Society: Materials Park, Ohio. 5284.
43. Massalski, T.B., ed. *Cu-Sb (Copper-Antimony)*. 2 ed. Binary Alloy Phase Diagrams, ed. T.B. Massalski. Vol. 2. 1990, The Materials Information Society: Ohio. 1471-1473.
44. Schubert, K. and M. Ilschner, **Untersuchungen Im System Kupfer-Antimon*. Zeitschrift für Metallkunde, 1954. 45(6): p. 366-370.
45. Heumann, T. and F. Heinemann, *Mehrphasendiffusion Im System Kupfer-Antimon*. Zeitschrift Fur Elektrochemie, 1956. 60(9-10): p. 1160-1169.
46. Hansen, M.A., K., ed. *Constitution of Binary Alloys*. 2 ed. 1958: New York.
47. Günzel, E. and K. Schubert, *Strukturuntersuchungen Im System Kupfer-Antimon*. Zeitschrift für Metallkunde, 1958. 49(3): p. 124-133.
48. Murakami, T. and N. Shibata, Science Report of the Tohoku University, 1936. Series 1, Volume 25: p. 527.
49. Suh, I.K., H. Ohta, and Y. Waseda, eds. *High temperature thermal expansion of six metallic elements measured by dilatation method and X-ray diffraction*. 2 ed. Pearson's Handbook of Crystallographic Data for Intermetallic Phases, ed. P. Villars and L.D. Calvert. Vol. 3. 1988, The Materials Information Society: Materials Park, Ohio. 2785.
50. Hofmann, W., ed. *Zur Überstruktur von Cu₃Sb*. 2 ed. Pearson's Handbook of Crystallographic Data for Intermetallic Phases, ed. P. Villars and L.D. Calvert. Vol. 3. 1941, The Materials Information Society: Materials Park, Ohio. 2980.
51. Schubert, K., et al., eds. *Einige strukturelle Ergebnisse an metallischen Phasen II*. 2 ed. Pearson's Handbook of Crystallographic Data for Intermetallic Phases, ed. P. Villars and L.D. Calvert. Vol. 3. 1957, The Materials Information Society: Materials Park, Ohio. 2980.
52. Yamaguchi, S. and M. Hirabayashi, *Long Period Superstructures with Hexagonal Symmetry in Cu-Sb Alloys near 20 at Percent Sb*. Journal of the Physical Society of Japan, 1972. 33(3): p. 708-&.
53. Karlsson, N., *An X-Ray study of the phases in the Cu-Ti-System*. Acta Crystallographica 1972. B (28): p. 371-378.
54. Günzel, E. and K. Schubert, eds. *Strukturuntersuchungen im System Kupfer-Antimon*. 2 ed. Pearson's Handbook of Crystallographic Data for Intermetallic Phases, ed. P. Villars and

- L.D. Calvert. Vol. 3. 1958, The Materials Information Society: Materials Park, Ohio. 2980-2981.
55. Pearson, W.B., ed. *Electrical resistivity, Hall coefficient, and thermoelectric power of AuSb₂ and Cu₂Sb*. 2 ed. Pearson's Handbook of Crystallographic Data for Intermetallic Phases, ed. P. Villars and L.D. Calvert. Vol. 3. 1964, The Materials Information Society: Materials Park, Ohio. 2980.
56. Barrett, C.S., P. Cucka, and K. Haefner, eds. *The crystal structure of antimony at 4.2, 78 and 298K*. 2 ed. Pearson's Handbook of Crystallographic Data for Intermetallic Phases, ed. P. Villars and L.D. Calvert. Vol. 4. 1963, The Materials Information Society: Materials Park, Ohio. 5182.
57. Richter, K. *VO Charakterisierung Anorganischer Materialien - Methoden und Modellierung, B_Methods_for_combination*. 2009; Available from: https://moodle.univie.ac.at/file.php/5010/B_Methods_for_Combination.pdf.
58. Nanostrukturforschung, F.f. 2010; Available from: nanozentrum.univie.ac.at.
59. West, A.R., *Basic Solid State Chemistry*. 1999: Wiley.
60. Riedel, E. and C. Janiak, *Anorganische Chemie*. 7 ed. 2007: Walter de Gruyter.
61. Villars, P. and L.D. Calvert, eds. *Pearson's Handbook of Crystallographic Data for Intermetallic Phases*. 2 ed. 1991, The Materials Information Society: Materials Park, Ohio.
62. Schubert, K. and H. Pfisterer, **Zur Kristallchemie Der B-Metall-Reichsten Phasen in Legierungen Von Übergangsmetallen Der Eisentriaden Und Platintriaden Mit Elementen Der Vierten Nebengruppe*. Zeitschrift für Metallkunde, 1950. 41(11): p. 433-441.

8 Appendices

8.1 List of figures

Fig. 1: Pb-Sn phase diagram for common soft solders [2]	- 7 -
Fig. 2: Possible liberation of lead into the environment [3]	- 9 -
Fig. 3: Multi chip package (recorded with an electron microscope) [5].....	- 10 -
Fig. 4: Copper wires [7]	- 11 -
Fig. 5: Tin ingots [11]	- 13 -
Fig. 6: Antimony crystals [12]	- 15 -
Fig. 7: Beta and gamma structure of Cu-Sn [31].....	- 18 -
Fig. 8: Current phase diagram version of the Cu-Sn-system [15]	- 20 -
Fig. 9: Stansfield's liquidus and invariant temperatures, cited in [17]	- 20 -
Fig. 10: Section of Heycock and Neville's phase diagram [16].....	- 21 -
Fig. 11: Phase diagram of Shepherd and Blough [17].....	- 23 -
Fig. 12: Small temperature effect at 590°C in pure Cu-Sn-alloys [35]	- 24 -
Fig. 13: Section of Hoyt's phase diagram [35].....	- 24 -
Fig. 14: Section of Bauer and Vollenbruck's phase diagram [37]	- 25 -
Fig. 15: Section of Hamasumi and Nishigori's phase diagram [18].....	- 26 -
Fig. 16: Section of Verö's phase diagram [18].....	- 26 -
Fig. 17: 15.1 at% Sn, quenched from 595°C, etched with FeCl ₃ . Beta (dark) and gamma (bright)	- 26 -
Fig. 18: Section of Raynor's phase diagram [20].....	- 27 -
Fig. 19: Lattice parameter a vs. composition, 710°C and 605°C [22].....	- 27 -
Fig. 20: Concentration profile of Sn in the Cu/Sn diffusion-couple at 700°C, 1h [31].....	- 28 -
Fig. 21: Section of phase diagram, A ₂ → B ₂ and B ₂ → D ₀ , 2nd order transitions [31].....	- 28 -
Fig. 22: Current phase diagram version of the Cu-Sb system [43]	- 31 -
Fig. 23: Transformation DO ₁₉ → ζ [47].....	- 33 -
Fig. 24: Transformation DO ₁₉ → BiF ₃ [47]	- 33 -
Fig. 25: δ-phase [52]	- 33 -
Fig. 26: ζ-phase [52].....	- 33 -
Fig. 27: Chill-moulds of the arc furnace	- 35 -
Fig. 28: CS_F_01, after arc furnace, diameter ~7mm	- 35 -
Fig. 29: Diamond saw	- 36 -
Fig. 30: Quartz glass tubes CS_F_01-06.....	- 36 -
Fig. 31: Samples in Mo-foil	- 36 -
Fig. 32: Embedded and polished samples	- 38 -
Fig. 33: Automatic grinder and polisher	- 38 -
Fig. 34: Sb purifying	- 39 -
Fig. 35: Open DTA furnace with crucibles	- 41 -
Fig. 36: DTA quartz glass crucible	- 41 -
Fig. 37: Temperature program Netzsch DTA 404S	- 42 -
Fig. 38: DTA Setaram Setsys Evolution [57].....	- 43 -
Fig. 39: open DTA furnace with open alumina crucibles (left side: sample; right side: reference Ti).....	- 43 -
Fig. 40: Bright field [57]	- 44 -
Fig. 41: Dark field [57]	- 44 -
Fig. 42: Polarization [57]	- 44 -
Fig. 43: DIC [57].....	- 44 -
Fig. 44: Zeiss Supra 55 VP ESEM [58]	- 46 -
Fig. 45: CAMECA SX 100 [57].....	- 46 -
Fig. 46: Bruker D8 diffractometer [57].....	- 47 -
Fig. 47: Origin of Cu-X-ray-radiation [59]	- 47 -
Fig. 48: Scattering of X-rays on crystal plains [60]	- 48 -
Fig. 49: Important equations to describe a X-ray-scatter-signal [57]	- 49 -
Fig. 50: High-temperature vacuum chamber.....	- 50 -
Fig. 51: High-temperature specimen holder	- 50 -
Fig. 52: DTA curves 13-20 at % Sn	- 54 -
Fig. 53: Comparison of diffractograms at 18 & 18.5 at% Sn, 700°C.....	- 58 -

Fig. 54: Lattice parameter vs. composition at 700°C	- 59 -
Fig. 55: Developed Cu-Sn phase diagram, including data points	- 64 -
Fig. 56: Developed Cu-Sn phase diagram with temperatures and compositions	- 65 -
Fig. 57: DTA curves 10-40 at % Sb	- 70 -
Fig. 58: Diffractogram of the sample 40 at% Sb, annealed at 600°C and quenched	- 74 -
Fig. 59: Developed Cu-Sb phase diagram, including data points	- 84 -
Fig. 60: Developed Cu-Sb phase diagram with temperatures and compositions	- 85 -
Fig. 61: Randomly arranged atoms in the W-type (Cu-Sn)	- 88 -
Fig. 62: Well ordered atoms in the BiF ₃ -type (Cu-Sn)	- 88 -
Fig. 63: Cu-Sb β -phase, crystal and (010) plane	- 88 -
Fig. 64: Cu-Sb ε -phase, (010) plane; arrows show transformation of $\varepsilon \rightarrow \beta$	- 89 -
Fig. 65: Comparison hcp vs. fcc unit cell	- 90 -
Fig. 66: Cu-Sb β -phase (BiF ₃ -type) , view along $\langle 111 \rangle$ axis	- 90 -
Fig. 67: Crystal and unit cell of the γ -phase (Mg-type)	- 90 -
Fig. 68: Cu-Sb γ -phase (Mg-type), (100) plane	- 90 -

8.2 List of tables

Table 1: Benefits of soldering [1]	- 5 -
Table 2: Disadvantages of soldering [1]	- 6 -
Table 3: Cu-Sn hard solders [1]	- 8 -
Table 4: Element data of Cu [6]	- 11 -
Table 5: Element data of Sn [6]	- 13 -
Table 6: Element data of Sb [6]	- 15 -
Table 7: Temperature-invariant reactions in the Cu-Sn-system [15]	- 19 -
Table 8: Misinterpretations of high temperature phases	- 22 -
Table 9: Crystallographic data of Cu-Sn phases	- 29 -
Table 10: Temperature-invariant reactions in the Cu-Sb-system [43]	- 32 -
Table 11: Crystallographic data of Cu-Sb phases	- 32 -
Table 12: Cu-Sn: Main sample compositions	- 34 -
Table 13: Cu-Sn: HTPXRD sample compositions	- 34 -
Table 14: Cu-Sn: Annealing temperatures and applied methods	- 37 -
Table 15: Cu-Sb sample compositions	- 39 -
Table 16: Cu-Sb: Annealing temperatures and applied methods	- 40 -
Table 17: Comparison of reactions and temperatures between literature and this work (Cu-Sn)	- 53 -
Table 18: Crystal structures and lattice parameters of quenched Cu-Sn-samples	- 55 -
Table 19: ESEM / EPMA results of Cu-Sn phase compositions	- 61 -
Table 20: Summary of ESEM / EPMA results	- 63 -
Table 21: Comparison temperature-invariant reactions in the Cu-Sn-system this work and literature [15]	- 66 -
Table 22: Comparison of reactions and temperatures between literature and this work (Cu-Sb)	- 69 -
Table 23: Crystallographic data of Cu ₃ Sb ₇ , refined from [62]	- 74 -
Table 24: Crystal structures and lattice parameters of quenched Cu-Sn-samples	- 75 -
Table 25: Found Cu-Sb phases in the PXRD analysis	- 77 -
Table 26: ESEM/EPMA results of Cu-Sb phase compositions	- 80 -
Table 27: Comparison temperature-invariant reactions in the Cu-Sb-system this work and literature [43]	- 86 -

8.3 Curriculum Vitae et Studiorum

Name: Siegfried Fürtauer
D.O.B.: Feb. 3rd, 1984, Wels
Citizenship: Austria
Home adress: Sobieskigasse 32/20, 1090 Wien

Education and career:

planned from October 2010	PhD studies at the Department of Inorganic Chemistry / Materials Chemistry, Vienna
2009-2010	Diploma thesis at the Department of Inorganic Chemistry / Materials Chemistry, Vienna: Investigation of relevant phase diagrams for high temperature solder materials: The binary systems Cu-Sn and Cu-Sb
2004-2010	Master studies at the University of Vienna Courses: Teachers Profession in Physical Education (PE) Teachers Profession in Chemistry
2003-2004	basic military service (military top sports centre Linz)
1998-2003	HTBLA in Wels, Upper Austria: College for Chemical Engineering
1994-1998	junior high school in Lambach, Upper Austria